Probing Transition Metal Dichalcogenide Monolayers and Heterostructures by Polarization-Resolved Spectroscopy

SUK HYUN KIM

Submitted in partial fulfillment of the

requirements for the degree

of Doctor of Philosophy

in the Graduate School of Arts and Sciences

COLUMBIA UNIVERSITY

2018

Abstract

Probing Transition Metal Dichalcogenide Monolayers and Heterostructures by Polarization-Resolved Spectroscopy

SUK HYUN KIM

The goal of this dissertation is to introduce my study on exotic materials in two dimensional world, not only to the well-trained researchers in this field but also to the beginners of condensed matter experiment. I hope this material to be a good guide for those of who paves the way of spintronics and valleytronics.

The first chapter will give you the introduction to two dimensional materials - Graphene and Monolayer Transition Metal DiChalcogenide (TMDC). The second chapter introduces some toolkits on optical techniques on condensed matter experiment, from very basics for everyone to the advanced for main projects of this work. They include Reflection Contrast, Raman Spectroscopy, Photoluminescence, and Pump Probe Spectroscopy. Chapter three will be review on several literature which are prerequisites for understanding and getting inspiration for this work. They are on the spin-valley indexes of carriers in TMDC, interlayer charge transfer in TMDC heterostructre, valley Hall effect, etc.

Chapter four will focus on the first half of main project, Charge and Spin-Valley Transfer in Transition Metal Dichalcogenide Heterostructure. Starting from the fabrication of heterostructure samples for our playground, we investigate the Interlayer Charge Transfer in our Heterostructure sample by ultrafast pump probe spectroscopy. We bring the polarization resolved version of the technique to study the Spin-Valley indexes conservation in the interlayer transferred charge, and analyze its physical

meaning. We study which one is the dominantly preserved quantity among spin and valley by using the broadband pump probe spectroscopy which covers A and B excitonic energy in TMDC material. As all the measurement here are taken under room temperature condition, this work paves the way for possible real device application.

Chapter five will cover the second half of main project, Electrical control of spin and valley Hall effect in monolayer WSe_2 transistors near room temperature. Spin and Valley Hall effect device in previous studies will be briefly revisited, and our new device is presented, using hole as carrier rather than electron for the robustness of valley index conservation, followed by optical experiment setting and results. Quantitative analyze on valley polarized carrier concentration and its depolarization time constant will follow. Chapter six will be a summary and direction to the future work.

Contents

List of Figures

Acknowledgments

It was such a long journey all the way from back to Pohang - a harbor city of South Korea, my hometown that I spend my 10 years in childhood - through Seoul- where all my family moved in and my undergraduate study took place - through New York - my Ph.D student life was began in Columbia University -to California - finally arrived in Stanford with my group. I cannot forget every single moment I struggle, fall down, stand up and run again in my Ph.D student life.

I specially thanks to my advisor, Professor Tony Heinz, who gave me wonderful opportunity to have a journey to the world of light and matter. In the movie Theory of Everything, depicting the life of Steven Hawking, there is a scene that Hawking and his fianc meet each other for the first time in a dancing party in their university. At the question what do you study? from the fianc, Hawking answers; I study the marriage of space and time. Every single time I was asked the same question, I answer; I study the marriage of light and matter., because of you, Tony.

Another special thanks is to Professor Philip KIM, former Columbia Professor and currently teaching in Harvard. As the best known Korean physicist you sent me the invitation to the world of 2D material from graphene through TMDC to other wonderland of materials. I always admire you and dreaming someday I become like you.

Our group postdoc Dezheng Sun was always my great, kind teacher, who taught me almost all the experimental techniques I know. I always thank to my group members like Elyse, Burak, Xiaoxiao, Yilei who stays and fight together in the darkness of the optics lab in the way to the truth. Finally, I always think of my beloved family - my mother Myung-Heui LIM, my father Jun-Hwan KIM, my sister Mi-Sol KIM.

Although they are far, far away in Korea, they always have been my great support and the reason I endure the pain of study.

Dedicated to Mi-Sol KIM, Jun-Hwan KIM, and Myung-Heui LIM

Chapter 1

Introduction to 2D material

We begin with the introduction to the physics of 2-dimensional material, especially the one with the honeycomb lattice Graphene and Transition Metal DiChalcogenides (TMDC). We point out their band structure briefly, and will point out the most prominent property of TMDC the spin valley locking effect.

1.1 Graphene

Graphene is atomically thin material made of carbon atoms, named after carbon material graphite and the suffix -ene, and it opened the world of practical realization of 2-dimensional material. Graphene was predicted as a building block of 3D graphite and its properties were calculated from a few decades ago. [1]

However, it was isolated and characterized for the first time by Andre Geim and Konstantin Novoselov at the University of Manchester only in 2004 [3]. Fig 1.1 show the honeycomb crystal structure of monolayer graphene, made of closely packed sp2 hybridization bonds.

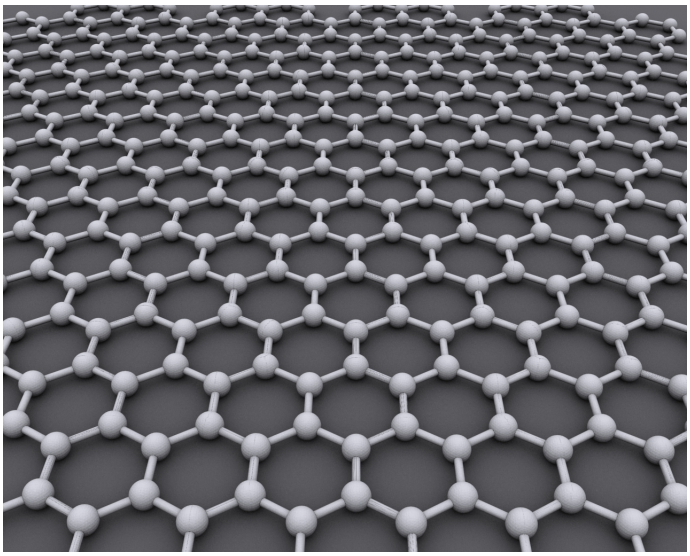

Figure 1.1: *Schematic Structure of monolayer graphene (illustration brought from [2])*

Tight binding method band calculation method with simple NN (Nearest Neighborhood) hopping, we see the Dirac cone shape band structure near K-point, without opening a gap, making the graphene semimetal phase.

While the electrons in plane makes the graphene structure robust, the p orbital electron in z direction adds free electron, making graphene very good conductor. With the optical transparency on top of it, graphene is nice candidate for transparent electrode particularly useful for display application. It is also widely used for atomically thin electrode for electrical study of other atomically thin material such as TMDC, 2D superconductor, 2D topological insulator, etc. The ultrathin conductor property of graphene serves ideal laboratory for 2D free electron gas, made various experiment possible quantum Hall effect even in room temperature [5] which were only possible in cryogenic low temperature.

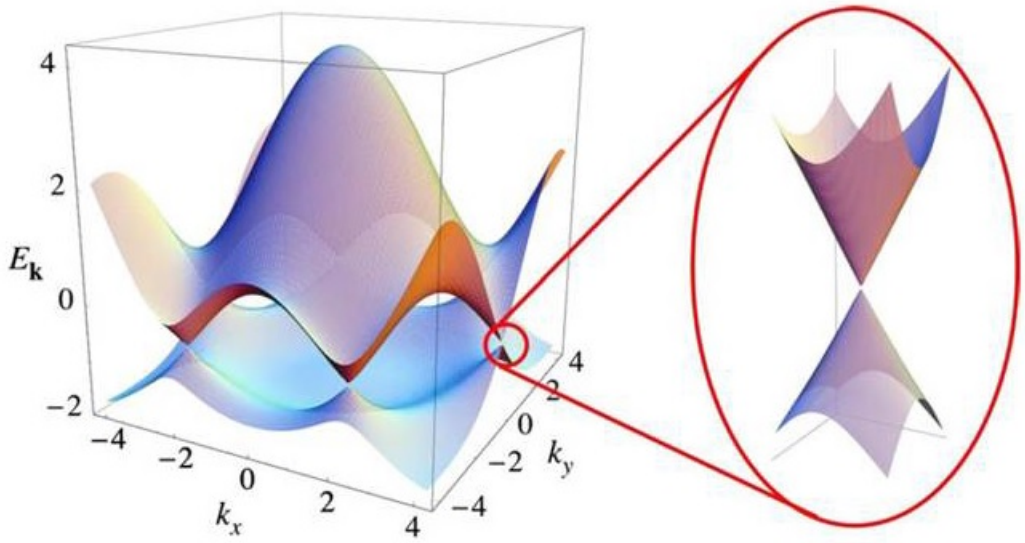

Figure 1.2: *Band structure of graphene - Dirac cone shape near K-point (illustration brought from [4])*

However when it comes to the semiconductor application of graphene, it is still far more way to go, with the obstacle of band gap generation which is essential for turning on/off the switch of semiconductor circuit device. The isolation of atomic monolayer material is done with famous Scotch tape exfoliation or CVD (Chemical Vapor Deposition) method, but to identify if we really have monolayer material is different matter. The optical detection of Monolayer graphene is usually done with finding the peak positions in Raman spectroscopy signal, which will be introduced in detail in Chapter 2.

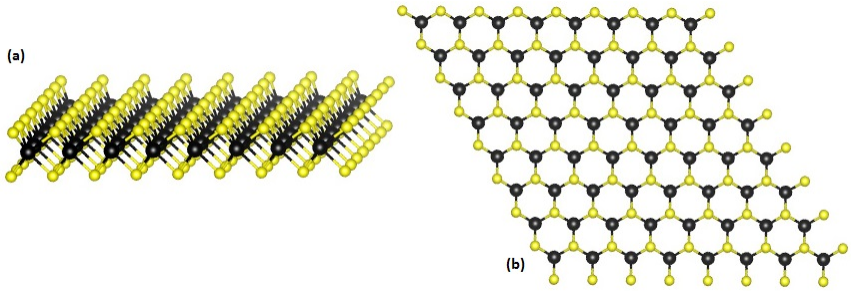

Figure 1.3: *Crystal Structure of TMDC - seen from (a) side and (b) above (illustration brought from [6])*

1.2 Transition Metal DiChalcogenides (TMDC)

Now here comes Monolayer Transition Metal DiChalcogenides (TMDC), our main playground of researches in this thesis. Fig 1.3 show the quasi-monolayer crystal structure of TMDC.

Seen from above, the TMDC crystal just looks same as the graphene honeycomb lattice at first glance. However there is difference first, there are two species of atoms forming the honeycomb, making the chemical formular of the material MX_2, where M is transition metal atom (Mo, W) and and X is chalcogen atom (S, Se, Te). Second, the two species of atoms are not in same height. Rather, one can say that two layers of X atoms are sandwiching one layer of M atom as Fig. 1.4 shows.

The inequality of two atoms and this quasi-monolayer 2D crystal structure makes an astonishing aspect - the sizable bandgap about the order of 1eV, which makes TMDC perfect playground for optical spectroscopy experiment, apart from semimetal behavior of graphene without bandgap. Now the two K and +K points in TMDC can be optically excited exclusively one by one in principle. See Fig. 1.5 for detail.

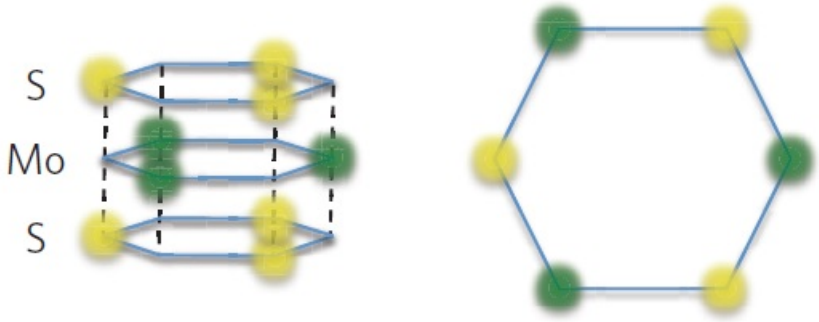

Figure 1.4: *Crystal Structure of TMDC - seen from (a) side and (b) above (illustration brought from [7])*

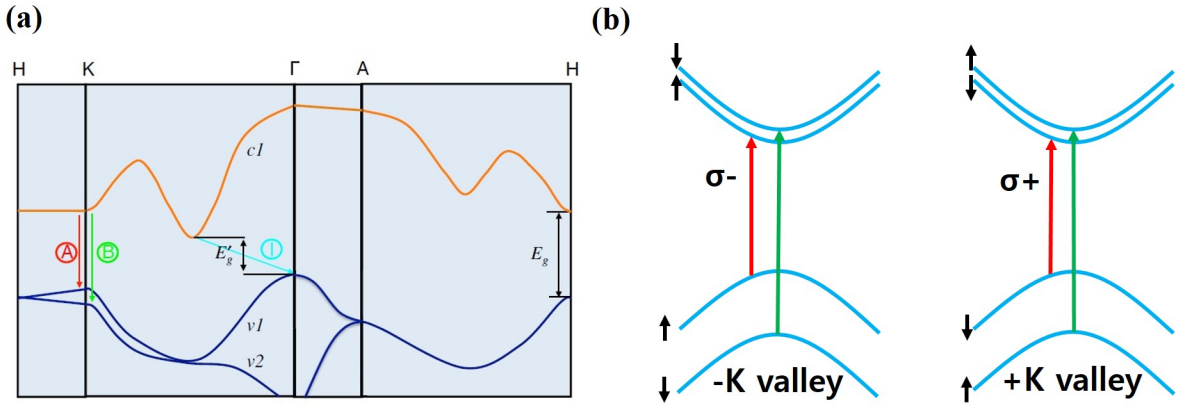

Figure 1.5: *(a) Band structure of TMDC [8] (b) Optical Selection Rule*

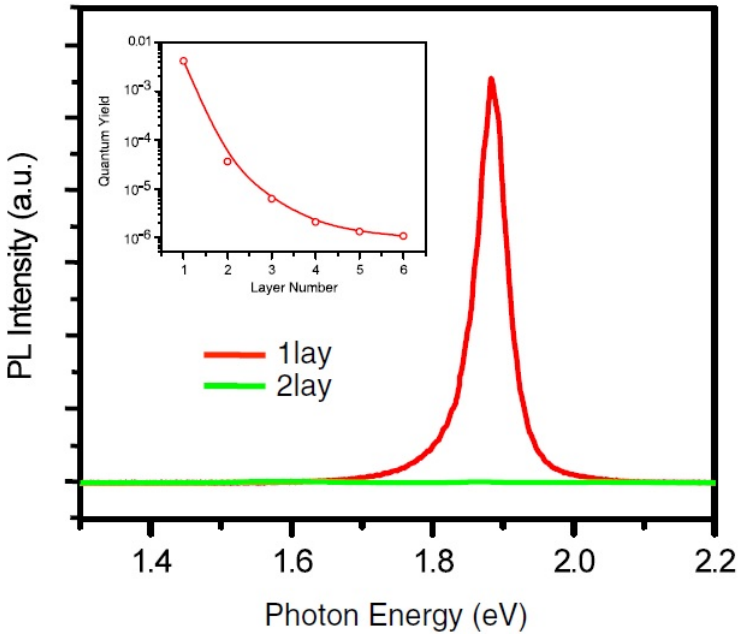

Figure 1.6: *Photoluminescense signal of Monolayer MoS_2 [8]*

You can see that the circular polarized light for each polarization can be used to excite electrons in one valley exclusively. The properties of bands in conduction band and valance band are different as well. The spin splitting (energy level difference for spin up and spin down electrons) of conduction band are just few or few tens of meV, makes the conduction band nearly spin degenerate in room temperature (for T = 300K, k_BT = 25.7meV) However the spin splitting of valance band are about few hundreds of meV, makes the spin separated holes cannot talk with each other. This makes hole particularly important for valley separation, which will be extensively used in our work in Chapter 5. The identification of monolayer TMDC is usually done with Photoluminescence (PL) Spectroscopy, whose method will be introduced in detail in Chapter 2.

Fig. 1.6 show the PL signal of monolayer and bilayer TMDC. As you can see

the signal from the monolayer is at least hundreds of times more than the bilayers, serves as a smoking gun evidence for the existence of monolayer sample in practical experiment.

Chapter 2

Experimental Setup

In this chapter, I will introduce some well-established and powerful technique for accessing key features of solid state material, like band structure, carrier dynamics, and spin-valley states. They are essential for characterization of sample and study of chapter 4, 5.

2.1 Reflection Contrast

Reflection Contrast (RC) spectroscopy is one of the most basic technique to investigate the band gap structure of material. We can see the dielectric function directly with the RC result, defined by

$$\frac{R_S - R_0}{R_S} \tag{2.1}$$

where R_S and R_0 are the reflection rate on the area with sample and without simple (bare substrate), respectively. As in Fig 2.1, in this work, RC measurement was

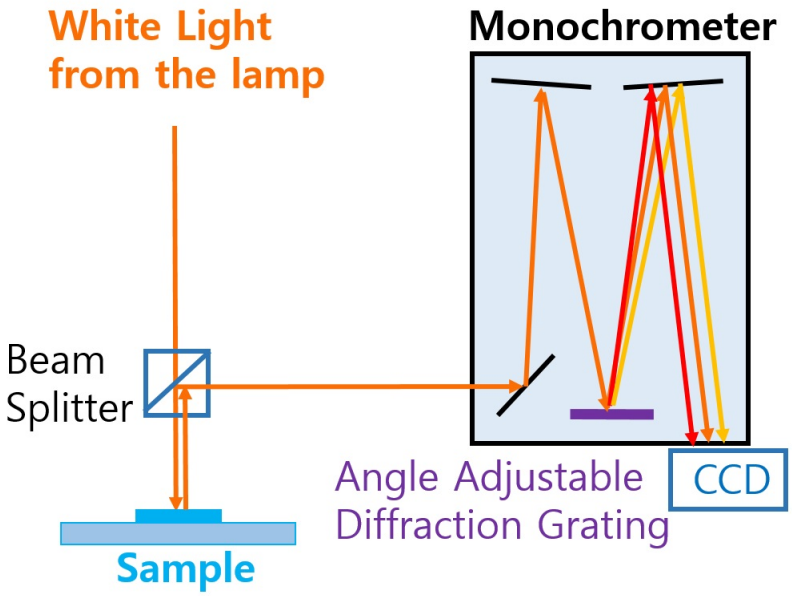

Figure 2.1: *Reflection Contrast Setup*

performed by broadband white light from tungsten halogen lamp, which is spatially cropped by a pinhole and focused on the sample into a circular region with the diameter about 2um by a 40x microscope objective lens. The reflected light from the sample is gathered and analyzed by a monochromator and electronically cooled CCD to $-80°C$. Since the equation calculates ratio of the reflection rates, RC is independent of the white light fluence, as long as the linearity of the sample response and the detector sensitivity are guaranteed.

Fig 2.2 is an example of RC spectroscopy on CVD grown monolayer MoS_2 and WSe_2, measured by myself. Since the measurements were performed on Si/SiO2 substrate, the interference effect makes the reflection on the sample weaker than the bare substrate site. Hence the reflection contrast value takes negative value, so I placed additional minus sign to revert the graph for convenience. The position of the

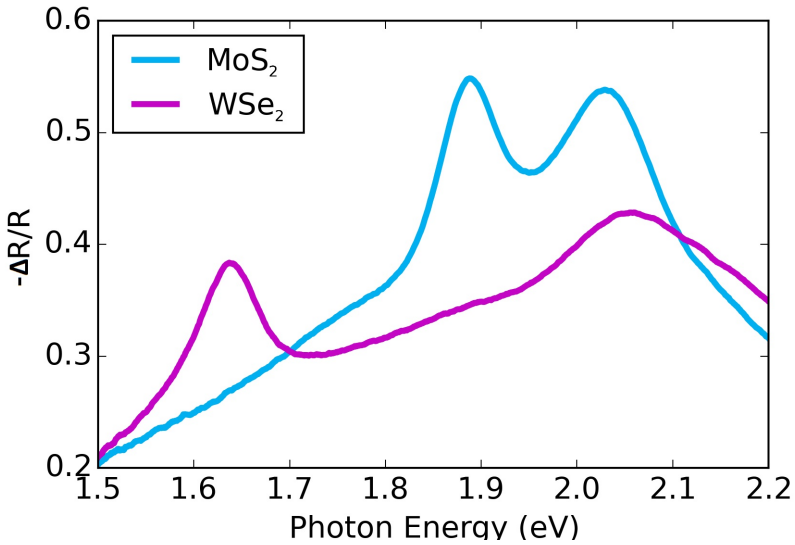

Figure 2.2: *Reflection Contrast Curve of Monolayer MoS_2 and WSe_2, at Room Temperature*

left (lower energy) and right (higher energy) peaks are the A and B excitons of each materials.

2.2 Raman Spectroscopy

Raman Spectroscopy is a technique to measure various phonons in a crystal, including vibrational, rotational, and other low-frequency modes. Laser beam is shined on a crystal, and reflected beam is gathered and spectrally analyzed. Among the reflected beam, there is not only the light with the original wavelength (or the original photon energy) but also a component of light with shifted photon energy about few or few tens of meV. After the original wavelength beam is optically filtered by edge filter, this little photon energy shift is detected with the monochromator and cooled CCD, which

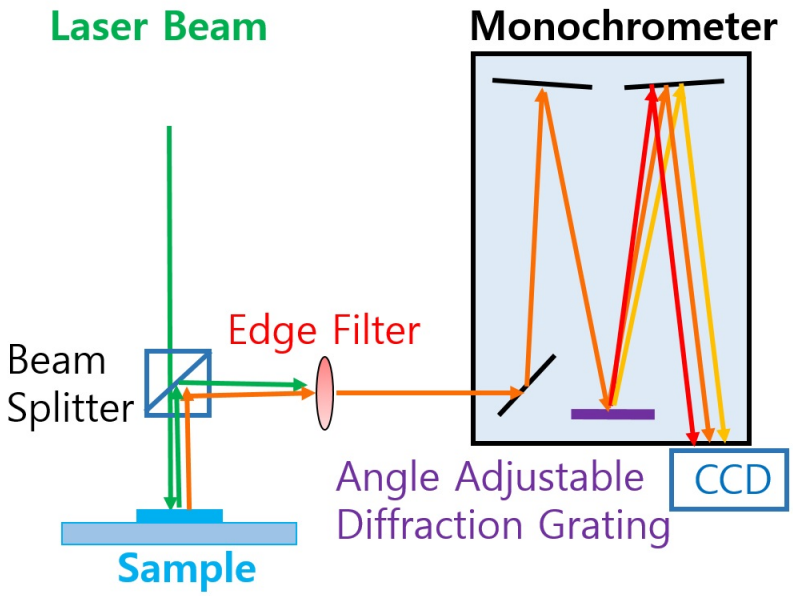

Figure 2.3: *Common Setup for Raman Spectroscopy and Photoluminescence*

corresponds transferred energy to phonon of the crystal. Fig 2.3 shows the optical setup we used in this work. Raman spectroscopy measurements were performed by continuous wave diode green laser beam with wavelength 532nm, using same objective lens, monochromator, and CCD as in the reflection contrast. Fig 2.4 was brought from [9], showing how is the raman spectroscopy signal is gathered and analyzed.

2.3 Photoluminescence

Photoluminescence (PL) Spectroscopy is a technique to measure energy gap structure especially in semiconductor material. This technique is particularly important in monolayer transition metal dichalcogenide, a main theme material of this thesis, because of the unusual strong PL intensity compared to the other material.

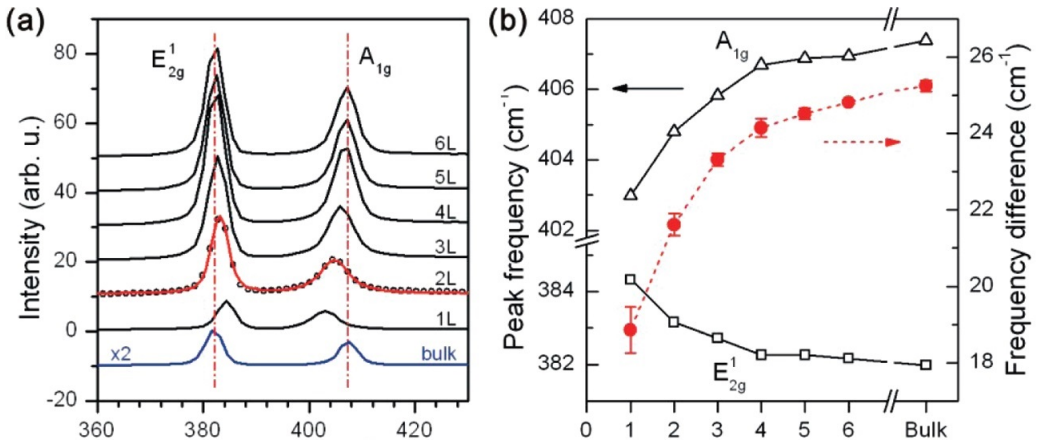

Figure 2.4: *Raman Spectroscopy of atomically thin MoS_2, from [9]. (a) Raman spectra of thin (nL) and bulk MoS_2 samples. (b) Frequencies of two different Raman modes, and their difference, depending on layer numbers.*

Practically, PL Spectroscopy uses almost exactly same experiment setup as in Fig 1.3. However I divide these two separated subchapters since they are originated from different physical phenomena. In the laser pumped excited sample, higher band electron and lower band hole pair bound, or exciton is formed, and recombination process releases photoluminescence photon with energy same as the band gap energy subtracted by the electron-hole pair bound energy, or exciton energy.

In PL experiment, laser beam is shined on a crystal, and we gather, optically filter, and spectrally analyze the reflected beam to find a component of absorbed and reemitted light. Unlike about few or few tens of meV shift of Raman spectroscopy signal, the emission photon energy is can be deviated from the original excitation beam energy by several hundreds of meV. In this work we used same setup in PL as in Raman. Fig 1.5 shows PL signal of Monolayer WSe_2 in room temperature. We see 1.6 eV peak which corresponds to A exciton energy of Monolayer WSe_2.

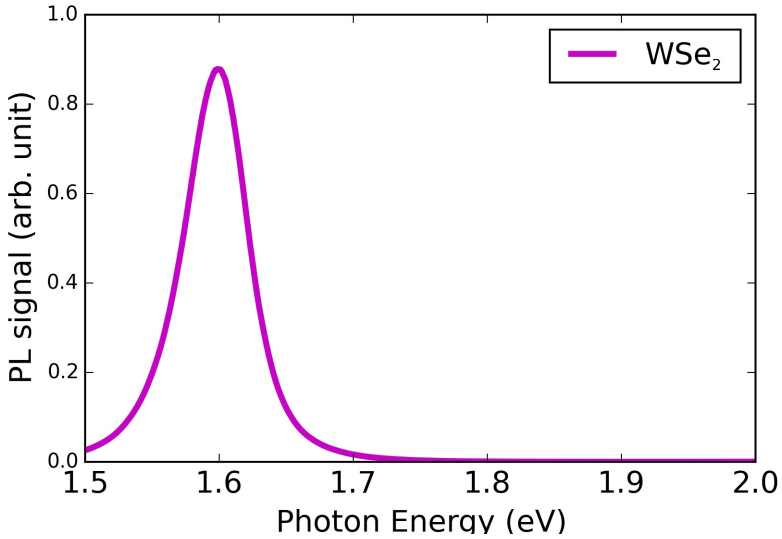

Figure 2.5: *Photoluminescence of Monolayer WSe_2*

2.4 Pump Probe Spectroscopy

Now we dive to the world of femtosecond ultrafast pulse laser. In order to look into the ultrafast carrier dynamics in solid, one should have a probe with the timescale sharper (shorter) than the carrier time scale. The pump-probe spectroscopy works as following. We bring well synchronized two pulse laser beam which are typically made from a single beam and beam splitter, and we call this as pump and probe beams. With white light generation and OPA (Optical Parametric Amplifier) method, this two beams can be at different wavelength. Moreover, they can be either monochromatic or broadband white light beam.

Figure 2.6 (a) is the basic picture of Pump Probe Spectroscopy. Our goal is to first excite the carrier of sample with pump beam, and detect the excitation with the probe beam, by measuring change in reflection induce from the pump beam. (One

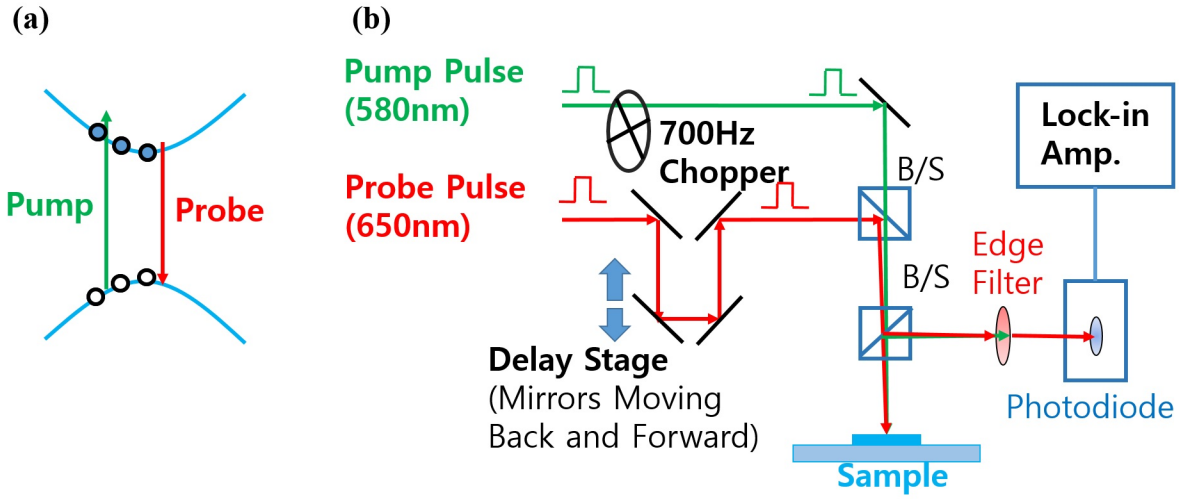

Figure 2.6: *Pump Probe Spectroscopy (a) Schematic Mechanism and (b) Optical Setup*

can do transmission experiment as well) Say that the pump and probe beams have photon energy enough to slightly overcome the band gap. Just after the carrier is excited by the pump beam of the sample material, the probe beam reflectance can be changed, since the pump-excited electron in the conduction band blocks (Pauli blocking) the additional probe induced excitation, hinders the probe beam photon absorption.

See Figure 2.6 (b) for practical Pump Probe Spectroscopy setup. We install 700Hz mechanical chopper in pump to detect pump influence of the probe reflectance. The arriving time interval between pump and probe are controlled by a pair of perpendicular mirror on linear motor stage, called delay stage. Using the fact that the speed of light is finite, by manipulating the beam path length we can make the arriving time of the beam pulse early or later. Considering the speed of light is finite and the beam path change is doubled with the delay stage geometry, 0.15mm change of

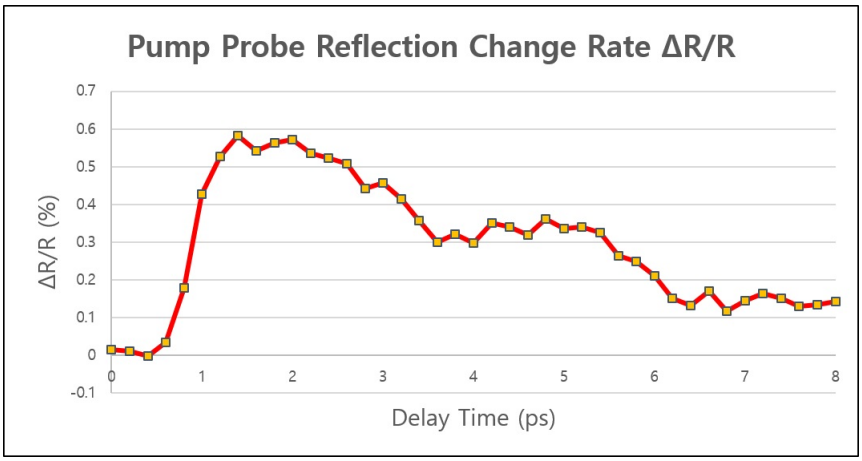

Figure 2.7: *Pump Probe Spectroscopy data - Pump induced Probe change rate in Monolayer* WS_2

delay stage makes 1ps beam pulse time difference. Fig 2.7 shows the result of pump induced probe change, usually denoted by percent.

Seeing Fig 2.8 (a), now one can turn this setup into band gap scanner for wide range of wavelength, using continuum white light probe pulses. Fig 2.8 (b) is the setup for broadband pump probe spectroscopy, applying monochromator at the end of the optical path. Fig 2.9 shows the result show on 2-dimensional plot, with the axes of delay time and wavelength. Along the wavelength axis the signal peak is around 645nm, showing the band gap of the WS_2 sample.

2.5 Polarization Resolved Spectroscopy

2.5.1 Kerr Rotation

In many studies related to spin and valley degree of freedom of carriers in solid, polarization sensitive measurements offered power tools. Among various derivatives,

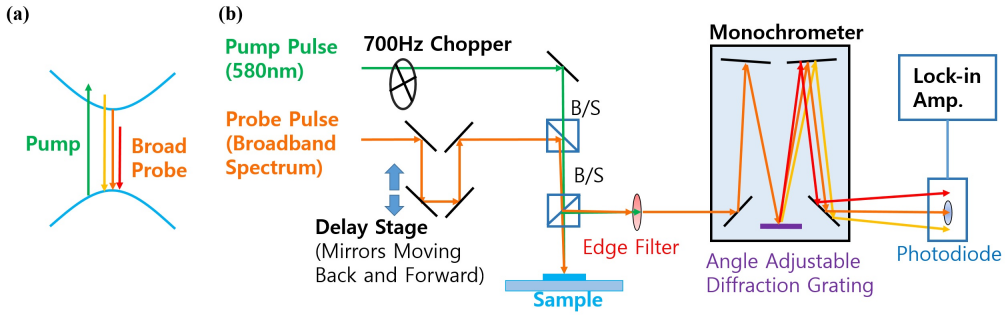

Figure 2.8: *Broadband Pump Probe Spectroscopy (a) Schematic Mechanism and (b) Optical Setup*

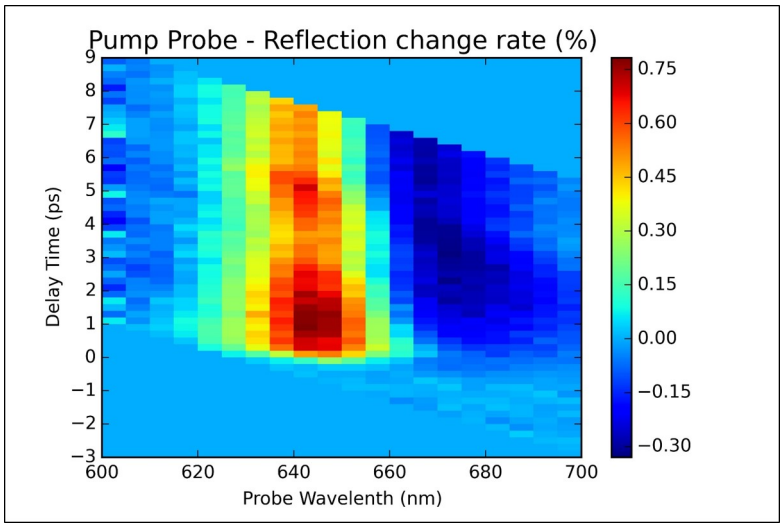

Figure 2.9: *Broadband Pump Probe Spectroscopy data - Pump induced Probe change rate in Monolayer WS_2*

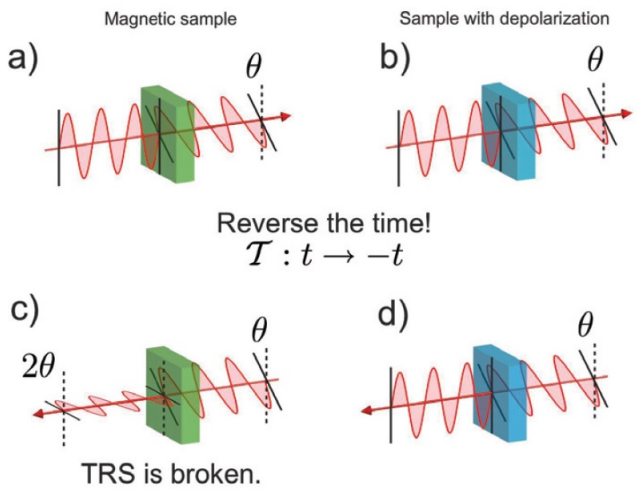

Figure 2.10: *Kerr Rotation from Time Reversal Symmetry Breaking, brought from [10]*

I will explain Kerr Rotation as a representative of this family of techniques. In experimental point of view, in Kerr Rotation we shine linear polarized light into the material surface and gathers reflected light. The measurement focuses on the rotated angle of the reflected light.

As you can see from Fig 2.10, the rotation of reflected beam can be induced only by the time reversal symmetry breaking (TRSB) of the sample material. The TRSB can be from spontaneous symmetry breaking process, circular polarized ultrafast pulse, magnetic field or electrical current.

Fig 2.11 shows up the Kerr Rotation detector setup called optical bridge. It consists of Wollaston prism a polarization sensitive beam splitter, and a pair of photodiodes. The setup is aligned so that after the typical reflection (usually takes place on the bare substrate area, or on the unperturbed sample), the linear beam split into two and enters the two photodiodes equally, 50 to 50. However if there is

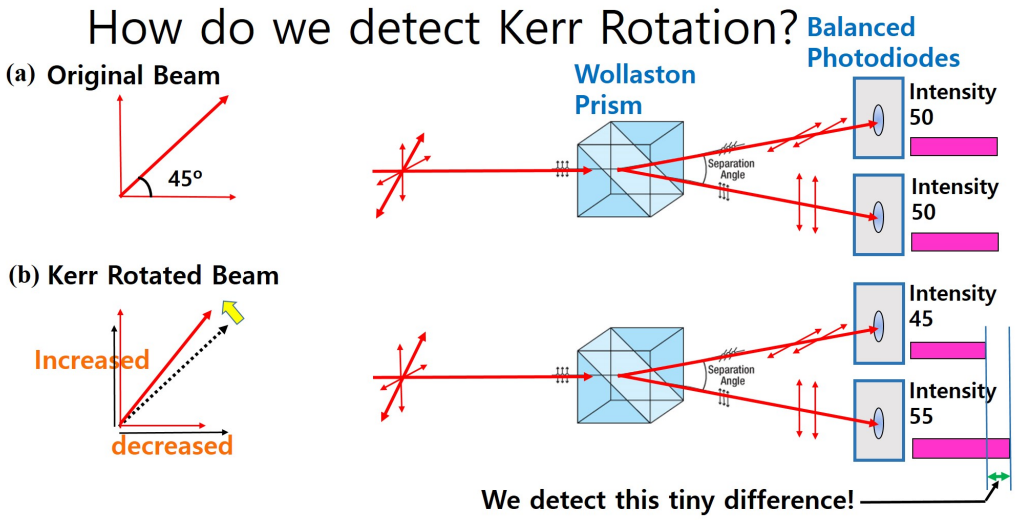

Figure 2.11: *Kerr Rotation Detector - Optical Bridge, analysing (a) Normal and (b) Rotated Reflection*

any rotation during the reflection on the (perturbed) sample area, the equilibrium is slightly broken, say like 51 to 49, and we detect tiny difference by differential electrical amplifier circuit. When the sensor linearity is guaranteed and the angle is small (¡¡ 1 rad), the electrical signal difference is proportional to the rotation angle.

2.5.2 Polarization Resolved Pump Probe Spectroscopy

For example, let us have a look into more specific case pump probe spectroscopy with the circular polarized pump and linear polarized probe in TMDC.

Among K and K valleys of TMDC, left circular polarized pump excites only K valley, making holes in valance band and electrons in conduction band. Linearly polarized probe, made of two circularly polarized lights, is deformed as described before. If the deformation is phase mismatching, we see Kerr Rotation.

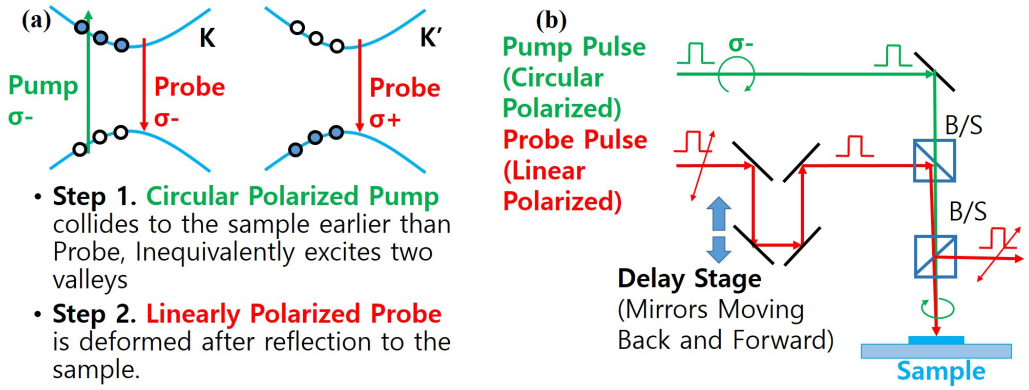

Figure 2.12: *Polarization Resolved Pump Probe Spectroscopy (a) Schematic Mechanism and (b) Optical Setup*

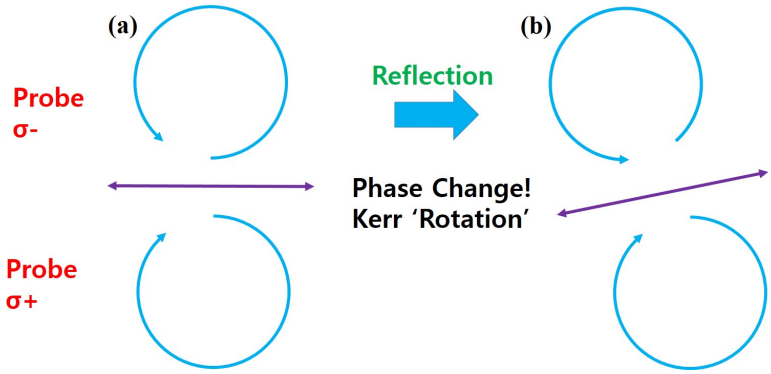

Figure 2.13: *Wave Optics point of view of Kerr Rotation, for (a) Normal and (b) Rotated Reflection*

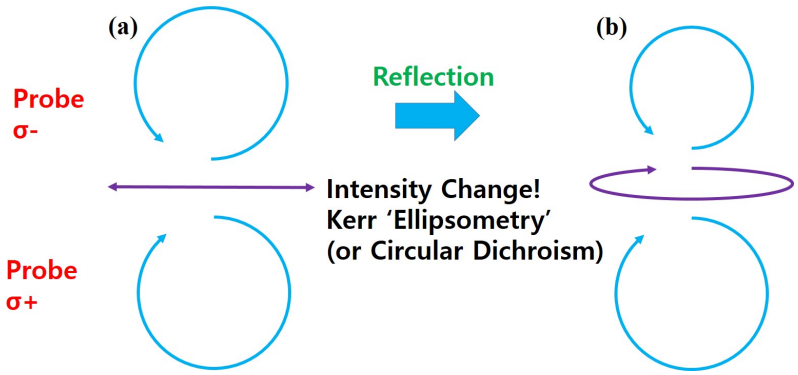

Figure 2.14: *Wave Optics point of view of Circular Dichroism, for (a) Normal and (b) Rotated Reflection*

Seeing Fig 2.13 (a) for the wave optics point of view, linear polarized light can be understood as a superposition of two circularly polarized lights, left and right, or CCW and CW. Kerr Rotation is induced by the phase misalignment of two circularly polarized components, as in Fig 2.13 (b)

2.5.3 Circular Dichroism

Then what if the phase remains its alignment but the reflection ratio is different for the two circularly polarized components? As in See Fig 2.14, the reflected beam forms elliptical polarization shape. We call this measurement as Kerr Ellipticity or Circular Dichroism.

In order to measure the small ellipticity of the light, we keep using the Kerr rotation setup with minor adjusting- inserting quarter wave plate. The elliptical beam becomes Kerr rotated beam (Fig 2.15) and we measure the tiny difference of the photodiode signal as we have done before (Fig 2.16).

All these experiment can be done wavelength (photon energy) resolved way by

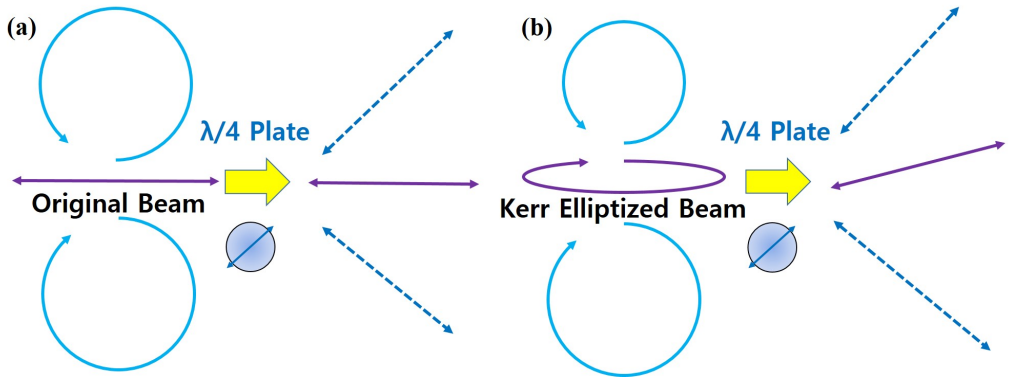

Figure 2.15: *Wave Optics point of view of Circular Dichroism with quarterwave plate, for (a) Normal and (b) Rotated Reflection*

installing monochromator before the Kerr rotation optical bridge, as in Fig 2.8.

When the reflection ratio difference is pretty much large, one can shine two circularly polarized components of light one by one and compare the result instead of using optical bridge.

2.5.4 An example of Polarization Resolved Pump Probe Spectroscopy

The study [11] shows practical application of this technique. Fig 2.17 shows the Kerr rotation signal measured on monolayer WSe_2 sample, cryogenically cooled to 4K with degenerate (same) pump and probe photon energy 1.735eV. (or wavelength 693.9nm) In this kind of degenerate pump and probe wavelength, beams are shine with some angle, deviated a little bit from the normal direction. Pump and Probe beams are separated by pinhole by virtue of different angle of incidence of two beams. We can see that the Kerr Rotation signal looks like exponential decay with time constant 6ps. The most significant of Kerr Rotation is that it flips the sign when the pump

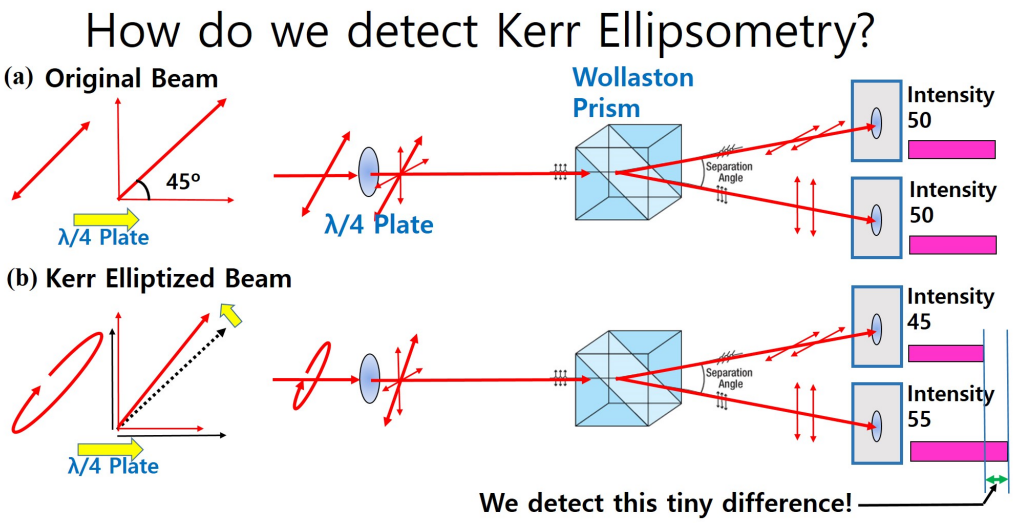

Figure 2.16: *Kerr Ellipticity (or Circular Dichroism) Detector - Optical Bridge with a Quarterwave Plate, analysing (a) Normal and (b) Rotated Reflection*

flips its polarization.

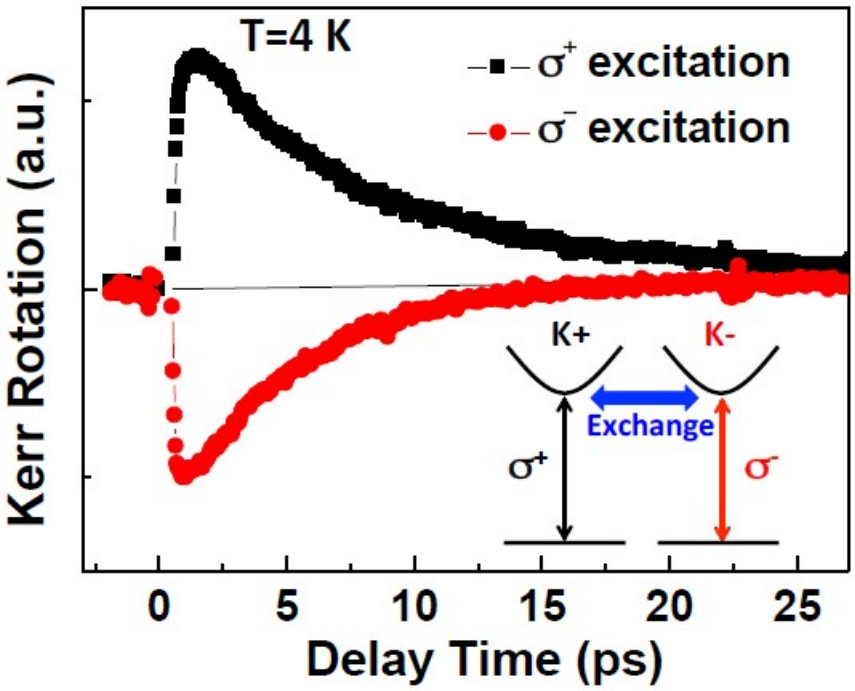

Figure 2.17: *Pump Probe Kerr Rotation of Monolayer* WSe_2 at temperature 4K, from [11]

Chapter 3

Review of Literature

In this chapter, we will review several prerequisite studies which lead us to our main work. We begin with the direct evidence of light matter interaction of TMDC related to the valley degree of freedom. Then we move to sandwiched monolayer TMDC the vertical heterostructure. We review the papers of interlayer charge transfer, and we move to the study to investigate if spin- valley index of the charge are interlayer transferred as well. We also visit the study on electrical control of spin-valley degree of freedom of carrier in TMDC materials.

3.1 Control of valley polarization in monolayer MoS_2 by optical helicity [7]

Monolayer transition metal dichalcogenides (TMDC) offer new avenues to control valley and spin polarization based on their valley circular dichroism and spin-valley locking. In this paper the authors are showing that among the -K and +K valleys,

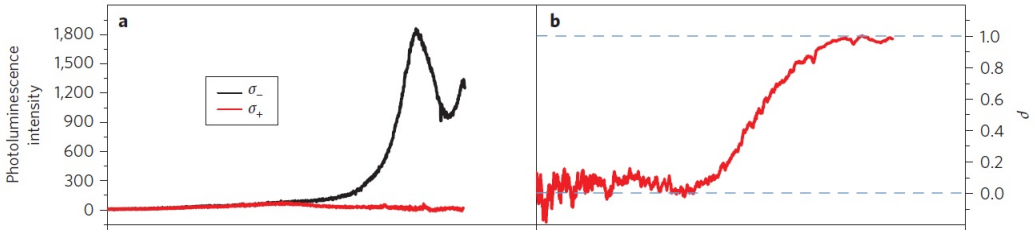

Figure 3.1: *(a) Photoluminescence signal of MoS_2 and (b) its helicity (from [7])*

one and only one valley can be excited by circular polarized light. Fig 3.1 (a) shows the Photoluminescence signal of MoS_2 monolayer in temperature 30K, excited by sigma - circular polarized light. This is one of the most basic experiment to observe the existence of valley in monolayer TMDC, and its role in light matter interaction. As you see in the graph, photoluminescence emission of same polarization as pump is dominant, showing that the excitation is done in one valley. Fig 3.1 (b) shows the graph of polarization factor ρ, defined by

$$\rho = \frac{I(\sigma+) - I(\sigma-)}{I(\sigma+) + I(\sigma-)} \tag{3.1}$$

where $I(\sigma+)$ and $I(\sigma-)$ stands for the intensity of light with polarization $\sigma+$ and $\sigma-$, respectively. ρ takes the value 1 for the perfect circular polarized light and 0 for non-circular polarized light. The ρ factor is near unity around the peak signal wavelength, but decreases to 0 with the wavelength further from it, showing that valley depolarization happens depending on the wavelength.

3.2 Optically initialized robust valley-polarized holes [12]

One can naturally think of information storage as a practical use of valley in TMDC monolayer, which is the main idea of valleytronics. However it requires enough time to write, store, read the information, while the time to keep information is only about picosecond scale. We can make use of hole instead of electron, for the holes have much wider spin splitting as you can see in Fig 1.5. This wide spin splitting makes the valley polarized holes extremely hard to hop to another valley, preserving the valley polarization much longer.

In this paper the authors used CVD monolayer WSe_2 at the temperature 10 K, which are naturally p-doped to investigate hole valleytronics.

Fig 3.2 (a) shows the optical bridge setup for the Pump Probe Kerr rotation as described in section 1.5.2 Polarization Resolved Pump Probe Spectroscopy. Fig 3.2 (b) shows the Kerr rotation signal, flipping the sign with the flipping pump helicity, showing the signal is from spin-valley effect which is an odd function of pump helicity.

Fig 3.3 (a) shows the Kerr rotation signal, decaying with the pump probe delay time, depending on the probe energy. (The pump energy was set always 12meV higher than the probe energy.) Fig 3.3 (b) shows the Kerr rotation signal snapshot in given time 2.5ps (about the maximum) and 100ps, depending on the probe energy. Compared with PL signal, we can see that the Kerr rotation signal takes maximum value around X+ (charged exciton - trion) peak, rather that X0 (neutral exciton) peak. The Kerr rotation signal is the result of the transfer of valley pseudospin from photocarriers to the resident carriers, in particular, the transfer of valley pseudospin

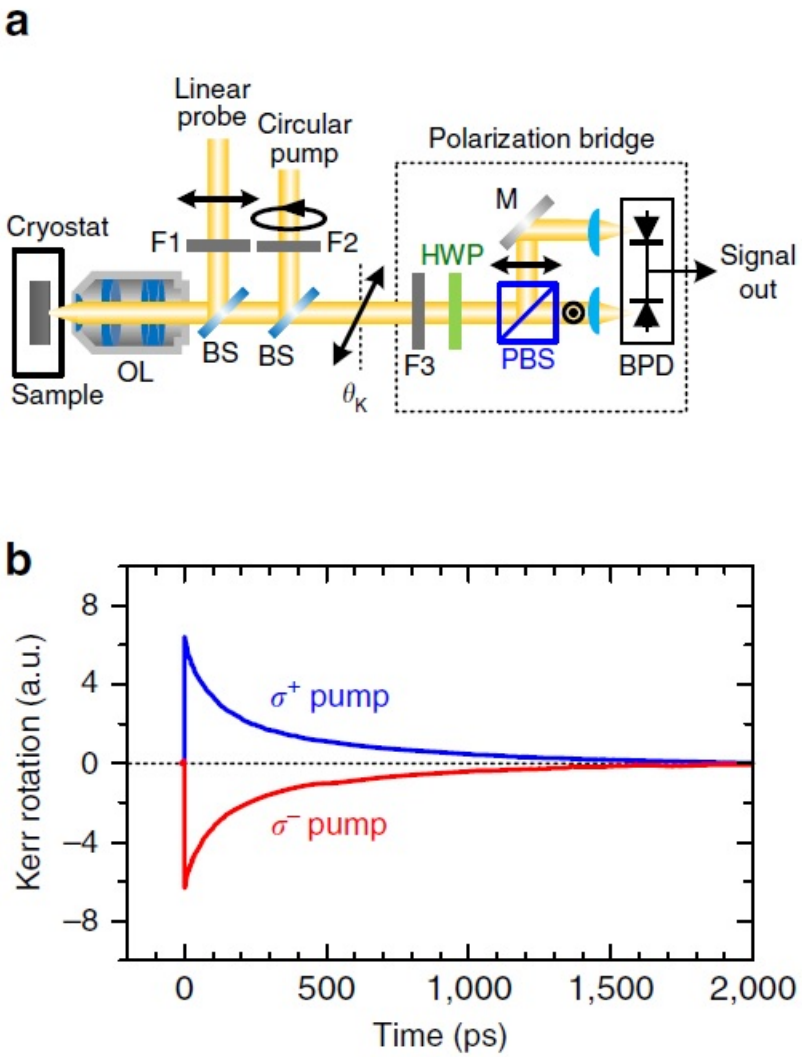

Figure 3.2: *(a) Pump Probe Kerr rotation setup (b) Kerr rotation signal (from [12])*

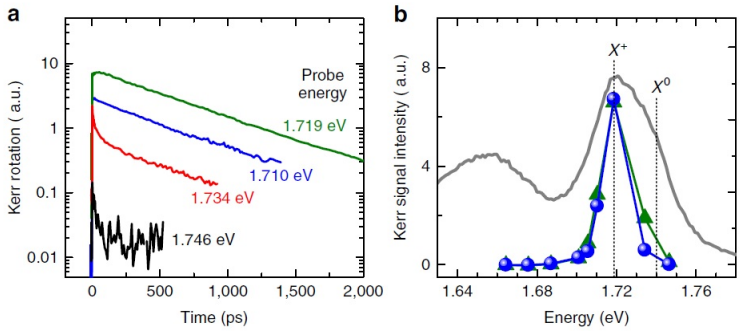

Figure 3.3: *(a) Kerr rotation signal, decaying with delay time (b) max. Kerr rotation signal for each probe energy (from [12])*

can be mediated by positive trion X+, leaving behind valley-polarized holes after trion recombination. This result will appear again in Chapter 4, when we try to explain the red shifted position of Circular Dichroism curve in TMDC heterostucture.

3.3 Ultrafast Charge Transfer in TMDC Heterostructures [13]

From the study of monolayer TMDC, now we turn to vertically stacked two different monolayer TMDC the TMDC (vertical) heterostructure. With the contact of two material, the Alignment of valance band and conduction band of two materials can be classified to 3 types.

Fig 3.4 (a) shows the band alignment of various TMDC materials, from [14], for selecting pairs of material for the type of alignment we want. Fig 3.4 (c) shows the 3 different band alignment type of heterostructure. The material studied in [13] is the stack of MoS_2 and WS_2, the type 2 heterostucture, the one we are particularly

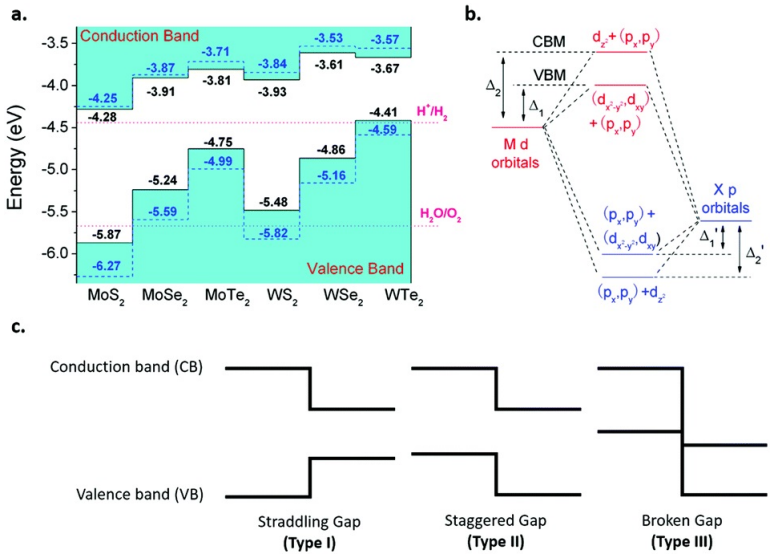

Figure 3.4: *(a) band alignment of various TMDC materials (b) Orbital Hybradization in TMDC Heterostructure (c) Three types of Band Alignment (from [14])*

interested in.

Fig 3.5 (a) shows the band alignment of two materials, MoS_2 and WS_2, which is type 2 band alignment as we have seen above. Fig 3.5 (c) is the photoluminescence signal of two materials in none overlapping areas. We can see that the WS_2 band gap energy is higher than that of MoS_2 from the PL peak positions. The authors shined a pulse laser beam to the sample with photon energy, which is higher than the MoS_2 band gap and lower than the WS_2 band gap, so that the electron are excited only in MoS_2 but not in WS_2. With the electron and hole pairs creation in MoS_2 conduction and valance band respectively, one can expect the hole transfer from MoS_2 to WS_2, or electron transfer from WS_2 to MoS_2, because the electron might want to fill the vacant lower energy state of MoS_2. They probed this charge transfer with pump probe spectroscopy.

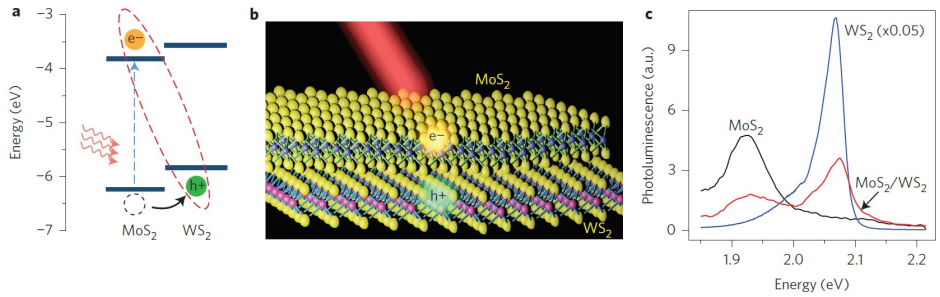

Figure 3.5: *(a) band alignment of MoS_2 and WS_2 Heterostructure (b) Interlayer Charge Transfer (c) PL signal of MoS_2, WS_2, and stacked area (from [13])*

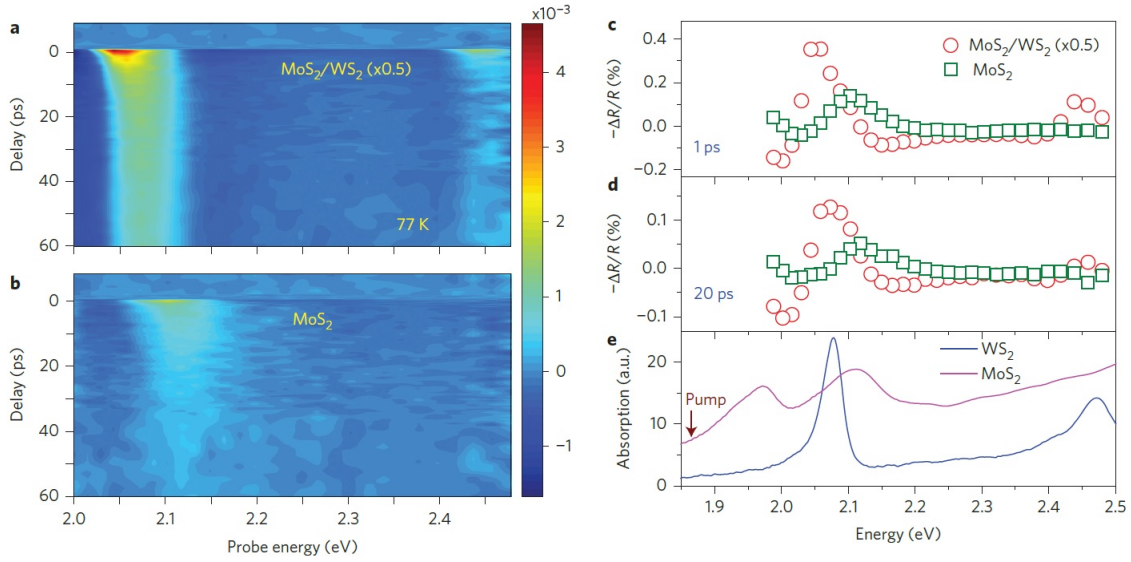

Figure 3.6: *Broadband pump probe spectroscopy result for (a) MoS_2 - WS_2 Heterostructure (b) MoS_2 only. Time sliced signal for t = (c) 1ps and (d) 20ps. (e) Reflection Contrast data (from [13])*

Fig 3.6 (a), (b) shows the broadband pump probe spectroscopy result, which is a powerful technique to scan the transferred charge over the band, as mentioned in Chapter 2. Fig 3.6 (a) is the 2D plot of pump induce probe reflection change and delay time. When the interlayer charge transfer happens, the absorption of the material is affected by pauli blocking mediated photobleaching effect, and the reflection change R/R is directly proportional to the change in absorption coefficient on atomically thin material on a transparent sapphire substrate. We look at the reflection change because it is easy to measure. The pump induced probe reflection change of the heterostructure sample shows significant peak at WS_2 gap energy, while the signal is not seen in bare WS_2 sample. On the bare MoS_2 sample there is a little peak but with much weaker strength and different position the MoS_2 B excitonic gap energy, showing that the signal from the heterostructure sample is not solely from WS_2 or MoS_2. This transient reflection experiment shows the evidence of interlayer charge transfer in type-2 heterostructure.

3.4 Interlayer spin-valley transfer in two-dimensional heterostructures [15]

We just have seen that in the monolayer TMDC material, excited carriers can store information as the form of spin and valley-pseudospin (spin- valley locking makes us difficult to say if the information is stored in spin or valley), and in the vertically stacked heterostructure made of 2 different monolayer TMDC with type-2 band alignment there can be interlayer charge transfer from one layer to the other. Then what if we combine these two phenomena? We might want to guess that in the TMDC het-

erostructure, if the excited charges in one material layer are spin-valley polarized well enough, and if the charges are to interlayer transfer to the other layer, the electrons might preserve its spin-valley information even after the charge transfer.

Recently there was one report that a charge transfer in $MoSe_2$-WSe_2 heterostructure is carrying not only charge itself but also spin valley information over the layers, observed by polarization sensitive CW laser pump probe spectroscopy at the temperature 30 K.

Fig 3.7 (a) show the transient reflection of $MoSe_2$-WSe_2 heterostructure sample and bare WSe_2 as a control experiment. Since band gap size of $MoSe_2$ is slightly smaller than that of WSe_2, by using the pump beam with photon energy in between the band gap of $MoSe_2$ and WSe_2, one can excite the carriers of $MoSe_2$ only, leaving WSe_2 untouched. The band gap alignment of $MoSe_2$ and WSe_2 is type 2 and looks like MoS_2 and WS_2 as we have seen before, so one can prove that there is a interlayer charge transfer from $MoSe_2$ to WSe_2 by the same method as in section 3.2. using pump beam with photon energy in between the band gap of $MoSe_2$ and WSe_2, and probe beam with photon energy same as the band gap size of WSe_2.

Fig 3.7 (b) show the transient transmission of $MoSe_2$-WSe_2 heterostructure sample. They excited a given spin-valley state in one layer by one (say sigma -) circularly polarized CW radiation resonant with the relevant exciton energy, and compared co- (sigma -) and cross- (sigma +) polarized transmission for resonant pumping of excitonic transitions in the other layer, examining the spin-valley characteristics of the interlayer transferred charge. The two graph Co- (burgundy) and cross- (green) circularly polarized probe are quite different in peak strength peak shape, showing that there is spin valley effect persists in transferred charge. Fig 3.7

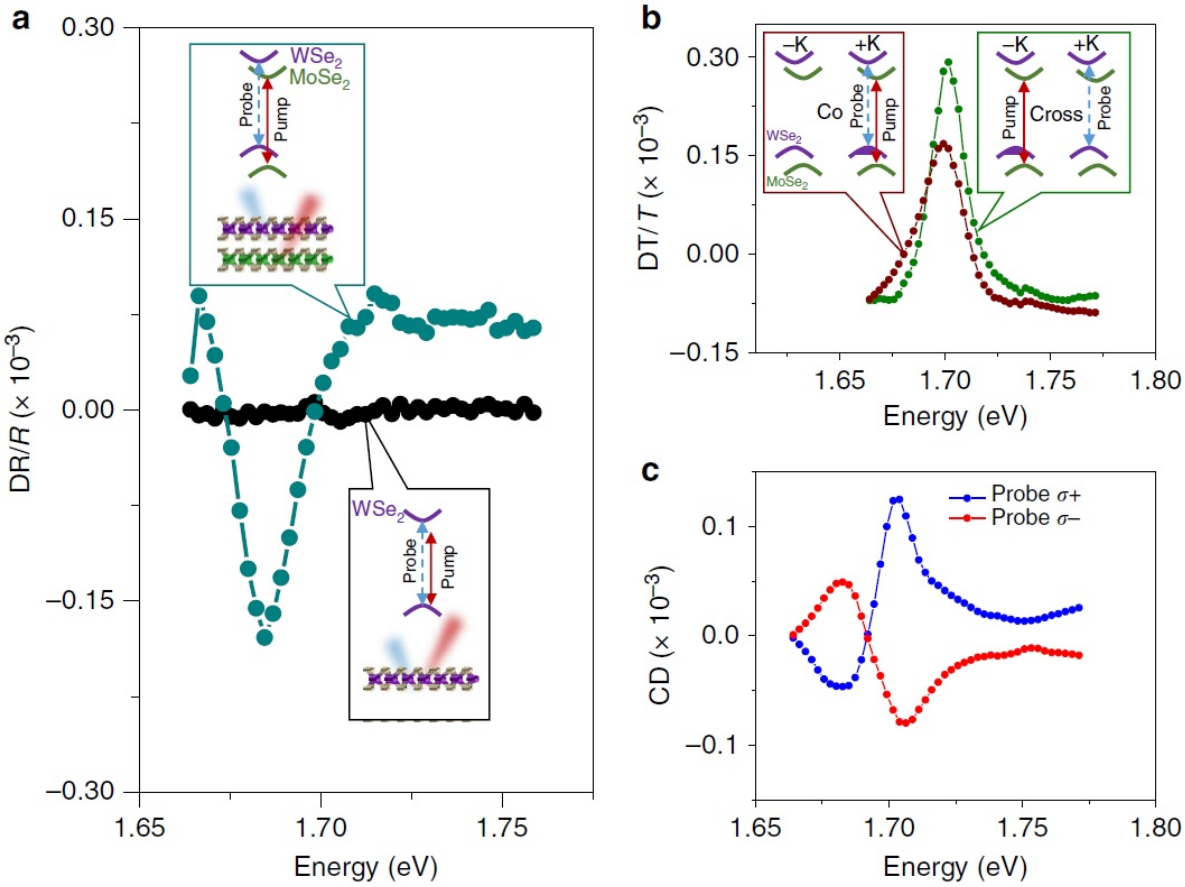

Figure 3.7: *(a) Transient reflection of $MoSe_2$-WSe_2 heterostructure and bare WSe_2, pumped at $MoSe_2$ band gap energy (b) transient transmission of $MoSe_2$-WSe_2 for co- and cross- polarized pump probe. (c) Circular Dichroism (from [15])*

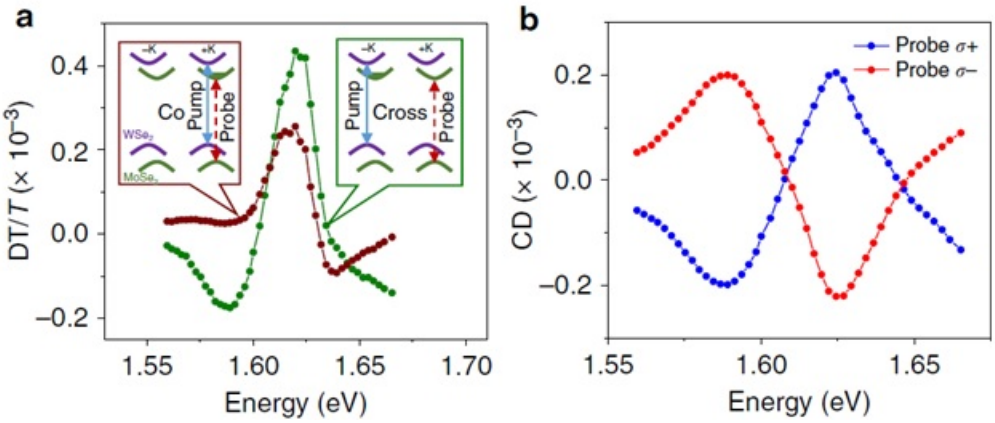

Figure 3.8: *(a) transient transmission of $MoSe_2$-WSe_2 for co- and cross- polarized pump probe, pumped at WSe_2 band gap energy (b) Circular Dichroism (from [15])*

(c) shows the circular dichroism of the sample. Usually the circular dichroism experiment is done by calculating the difference of the transmission (or reflection) signals between (sigma -) probe and (sigma +) probe, but it can be done by measuring difference of the signals between (sigma -) pump and (sigma +) pump, and the authors chose the latter method. In Fig 3.7 (c), the circular dichroism graph flips the sign with changing of probe helicity, showing that the effect is spin-valley effect. Hole. This experiment used the interlayer Hole transfer from the valence band of $MoSe_2$ to the valence band of WSe_2. However what will happen if we try the interlayer Electron transfer from the valence band of $MoSe_2$ to the valence band of WSe_2? If we shine the light with the photon energy same as the WSe_2 band gap, which is larger than the $MoSe_2$ band gap, than the electrons can be excited both in WSe_2 and $MoSe_2$, and the excited electrons in WSe_2 conduction band can transfer to the $MoSe_2$ conduction band.

Fig 3.8 (a) shows the transmission spectra of circular polarized (sigma -) po-

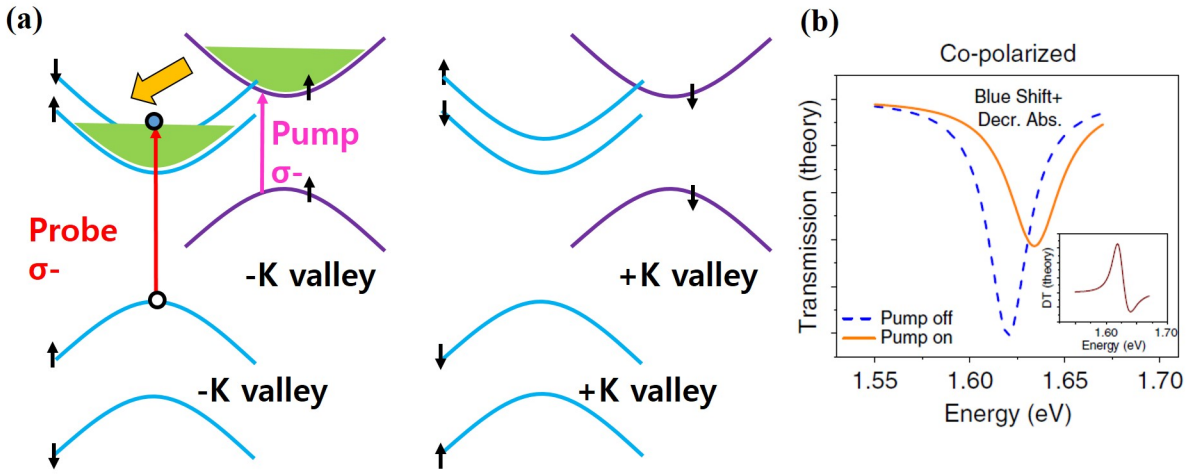

Figure 3.9: *(a) Band Diagram for Co- polarized pump probe, pumped at WSe_2 band gap energy (b) Estimated Transmisson (from [15])*

larized probe beam for the co- (sigma -) and cross- (sigma +) resonant pumping of excitonic transitions in the WSe_2 layer. Fig 3.8 (a) shows the circular dichroism the signal difference between co- (sigma -) and cross- (sigma +) resonant pumping, flipping the sign with the helicity of probe beam, as expected. The graph in Fig 3.8 (a) does not seems from one single lorentzian peak but made of a couple of peaks with different center position. This can be explained by the effect of neutral exciton and charged exciton (trion) as in Section 3.2. Lets have a look at it in more detail.

Fig 3.9 (a) shows the mechanism of pump induced probe transmission change for the Co- circular polarization. Assuming the ideal case with (perfectly matched crystal angle), Pumping is in - polarization, the excited electrons in WSe_2 (K,) conduction band are entirely transfer to (K,) band of $MoSe_2$ conduction band, and probe is in - polarization, which is Co-polarized case. The transferred electron in $MoSe_2$ conduction band blocks the formation of neutral exciton with Pauli blocking, so the

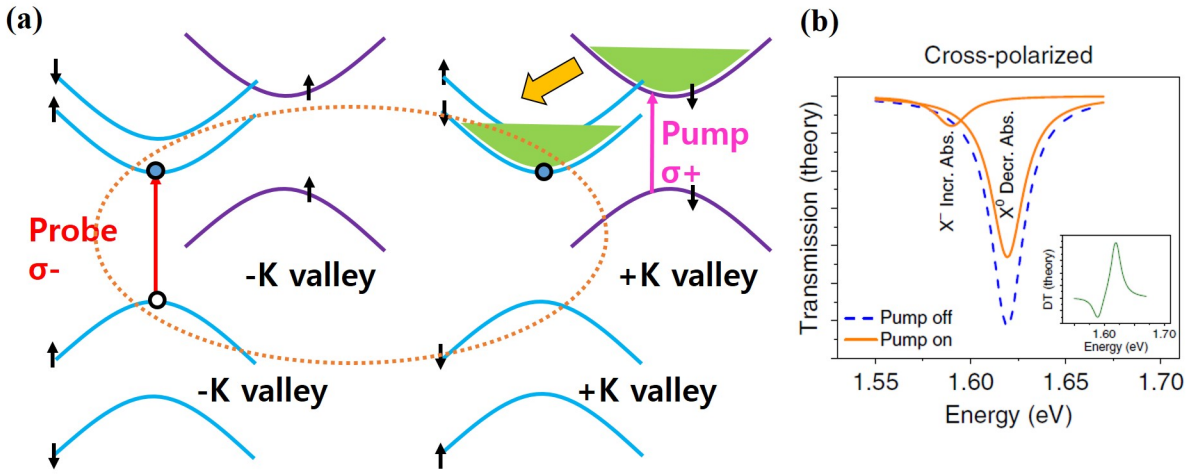

Figure 3.10: *(a) Band Diagram for Cross- polarized pump probe, pumped at WSe_2 band gap energy (b) Estimated Transmisson ([15])*

exciton formation becomes harder, and exciton energy gets higher because of the rising of electron level with the accumulated electron. As a result, neutral exciton peak gets smaller, and blue shifted, as shown in Fig 3.9 (b).

Fig 3.10 (a) shows the mechanism of pump induced probe transmission change for the Cross- circular polarization. Assuming the ideal case, Pumping is in + polarization, the excited electrons in WSe_2 (+K,) conduction band are entirely transfer to (+K,) band of $MoSe_2$ conduction band, and probe is in - polarization, which is Cross-polarized case. When there is transferred electron in $MoSe_2$ conduction band, it forms together intervalley trion the charged exciton, with the neutral exciton created by probe, and the pure neutral exciton concentration is diminished for they are taken to form the trion. As a result, neutral exciton peak gets smaller, and trion peak appears in red shifted position (30meV) from the neutral exciton peak, as shown in Fig 3.10 (b).

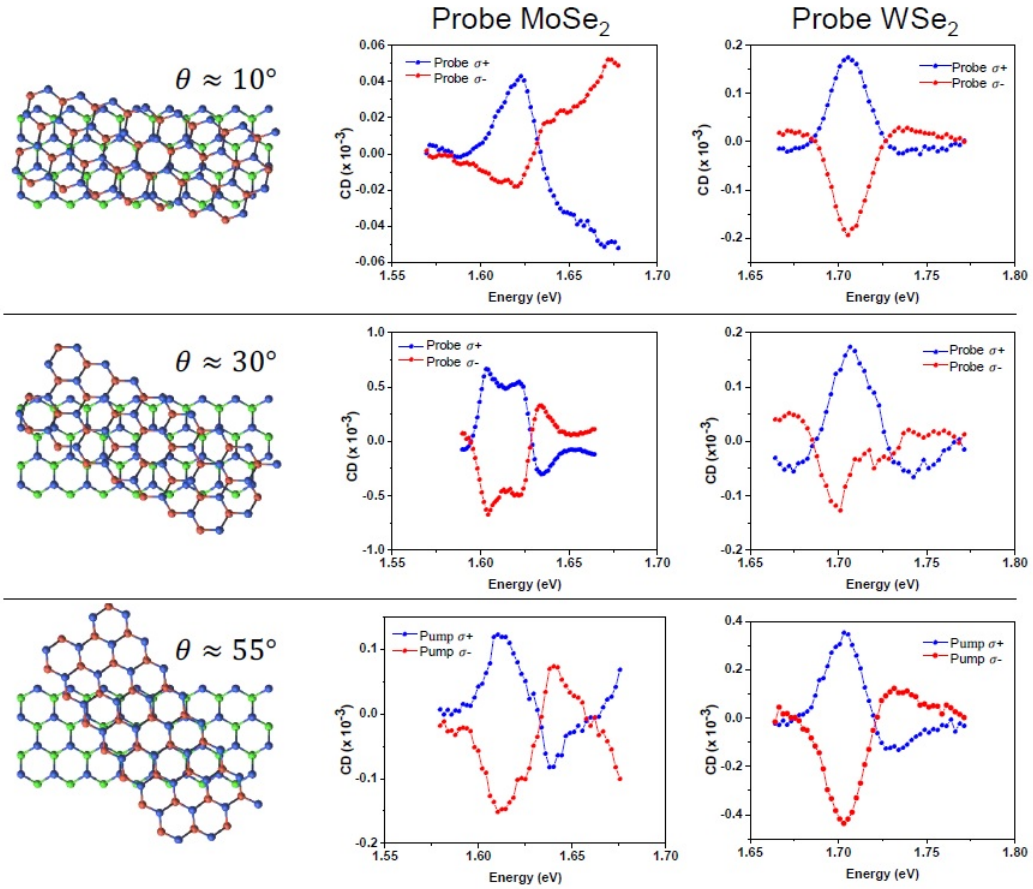

Figure 3.11: *Circular Dicroism for 3 different crystal angle (from [15])*

The authors just assumed that in the TMDC heterosturcture, the valley specifically excited electrons are interlayer transferred to same valley of new material as the original valley of new material. One can think that it is originated from the valley momentum conservation and available only in the case of well aligned crystal. In other words, the crystallographic orientation angle which can range from -60 +60, is near 0.

Then what if one does the same experiment with different crystal angles? Fig

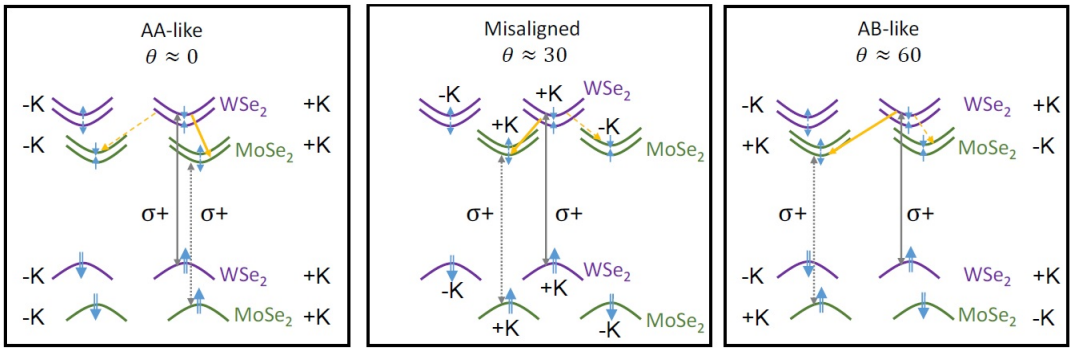

Figure 3.12: *Band Diagram and Electron Transfer for Circular polarized pump probe for 3 different crystal angle ([15])*

3.11 shows the circular dichroism result for 3 different angles, 0, 30, 55 deg. Surprisingly, the graph results keeps its overall shapes. We can see that after the interlayer transferred process, the valley specifically excited electrons are moved to always same, designated valley of new material, no matter what the alignment angle is. How can it be possible?

Fig 3.12 shows the band diagram of $MoSe_2$- WSe_2 heterostructure, depicting the electron transfer for the different crystal angles - 0, 30, 60 deg. The authors claim that because of the wide (30meV) spin splitting of $MoSe_2$ conduction band and cold temperature, (30K 3meV), among two conduction bands upper and lower conduction band, the electrons should precipitate into the lower conduction band. The inter-valley scattering might be assisted from crystal phonon or other thing, and if we assume the spin is well conserved, than the electrons can go only to the lower conduction band with designated valley because of the spin conservation.

3.5 Electrical control of the valley Hall effect in bilayer MoS_2 transistors [18]

Now apart from optics-only experiment, we will have a look at the new stage, the electronic property of TMDC the valley Hall effect. Monolayer transition metal dichalcogenides (TMDC) gave us opportunity to control valley and spin polarization, which might be able to lead us to the spintronics and valleytronics. However, for the practical application to the real world device, we should be ready to prepare, manipulate, read the spin valley information not only optically but also electronically. There has been long effort to control the spin valley states of carrier in semiconductor. One of the most famous study on this topic is the method of carriers separation with spin index, using spin-Hall effect. [16]

Spin Hall effect is a successor of ordinary Hall effect, which is originated from the spin-orbit coupling. In case of current flow in the 2D material with spin-orbit coupling, the carriers feels transverse directional force with the direction depends on the spin. In case of strip-like material geometry, the carriers with opposite spins are accumulated in opposite side of the strip.

See Fig 3.13 (a) for the detail of experiment setting. In this study, they prepared a long and thin semiconductor bar made of GaAs/InGaAs heterostructure(a good testbed of 2D electron gas used to be used before graphene and other 2D material), and applied voltage across the bar to flow some current. The spin density of the electrons were examine with Kerr rotation with 825nm pulsed laser. In the previous experiment the time reversal symmetry breaking (or more specifically in TMDC, the valley symmetry breaking or inequivalent valley excitation) is induce by circular

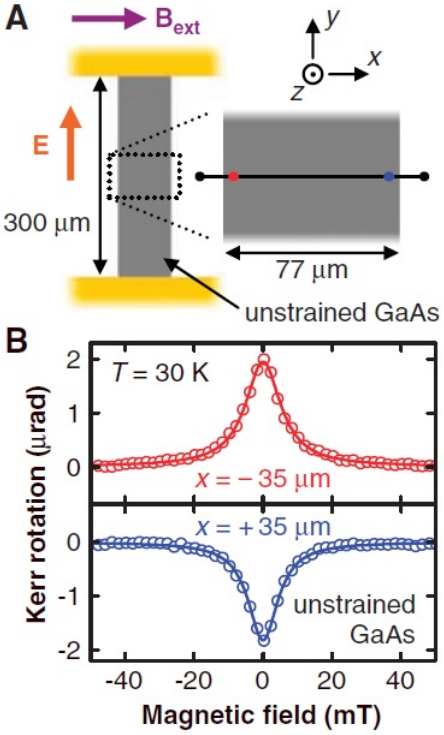

Figure 3.13: *Spin Hall Effect experiment (a) setup (b) result in two opposite side of edges (from [16])*

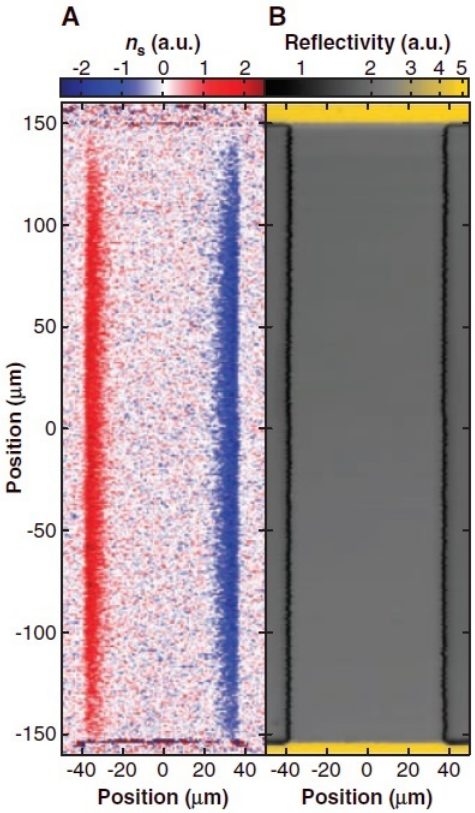

Figure 3.14: *Spin Hall Effect experiment result (a) 2D Kerr imaging, (b) 2D Reflectance imaging, of the whole GaAs/AlGaAs bar plane (from [16])*

polarized light and optically probed, but in this experiment it is electrically generated, and probed in same way. With the electric separation of carrier, the electron spin expected to be accumulated in each side of the bar. Fig 3.13 (b) shows the result in each edges of the bar, left and right. The edges are filled with spin polarized electrons up and down for each sides.

Fig 3.14 (a) shows the 2D Kerr imaging of the whole bar plane, showing the prominent spin polarization colored by red and blue. Fig 3.14 (b) shows the reflectance imaging of the sample. The symmetric nature of the map proves that the different

Kerr rotation signal in left and right edges are not from the difference in reflection. They even applied external magnetic field perpendicular to the current and parallel to the bar plane and have shown that the signal vanishes for strong external magnetic field, in order to prove the Kerr rotation signal comes from the spin Hall effect.

One might want to try an analogous experiment in Monolayer TMDC as well, and since the valley index is determined at the edge of the band with the spin-valley locking, we can call this as valley Hall effect. Lets have a look at the following study, [17], [18].

The Kerr Rotation imaging of Monolayer MoS_2 shows that the Valley Hall effect is shown clearly on the Monolayer TMDC, where the centrosymmetry is naturally broken in Monolayer TMDC. However one can start from the material with unbroken symmetry and break the symmetry to see the induced Valley Hall effect.

See Fig 3.16 (a) for the illustration of crystal structural symmetry. The valley physics of monolayer TMDC is originated from the fact that the centrosymmetry is broken in Monolayer TMDC, and the symmetry is recovered in bilayer TMDC since the bilayer is formed by stacking of two monolayer with center-rotated position to each other. However, the symmetry can be broken with vertically electric field, so that one can tune the symmetry breaking by adjusting the electric field. The electrical driven Kerr rotation experiment was done with method to similar as in [16], see Fig 3.16 (b). In addition, there is vertical electric gating to the sample to tune the symmetry breaking of the bilayer crystal.

Fig 3.17 (a) is the reflection and Fig 3.16 (b) is the Kerr rotation imaging under the high vertical electric gating, just like Fig 3.14 (a) and (b). Once again, from the separation of carrier spin, we can see the spin and valley Hall effect of the 2D

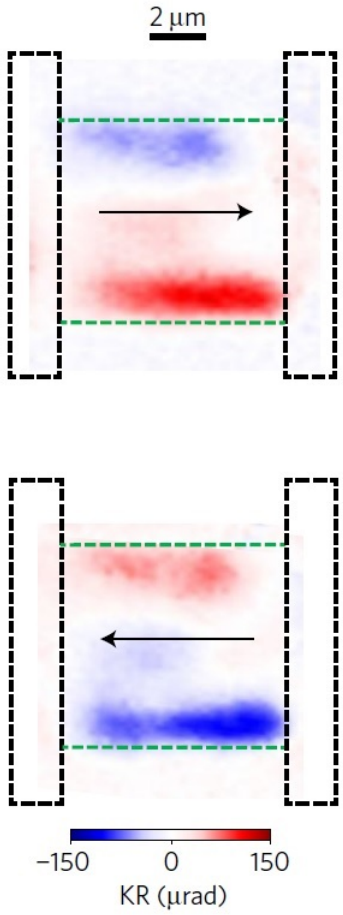

Figure 3.15: *Kerr Rotation imaging of Monolayer MoS_2 (from [17])*

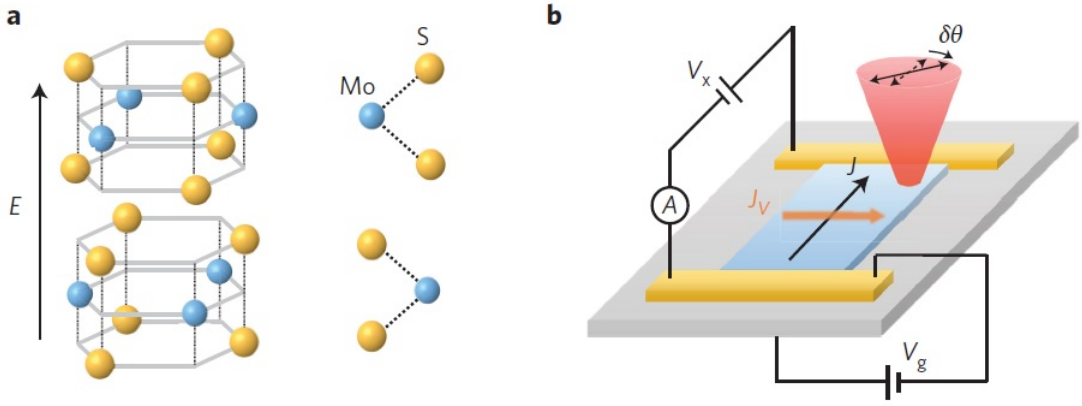

Figure 3.16: *(a) illustration of Bilayer MoS_2 crystal structural symmetry. (b) Spin Valley Hall Effect experiment setup (from [18])*

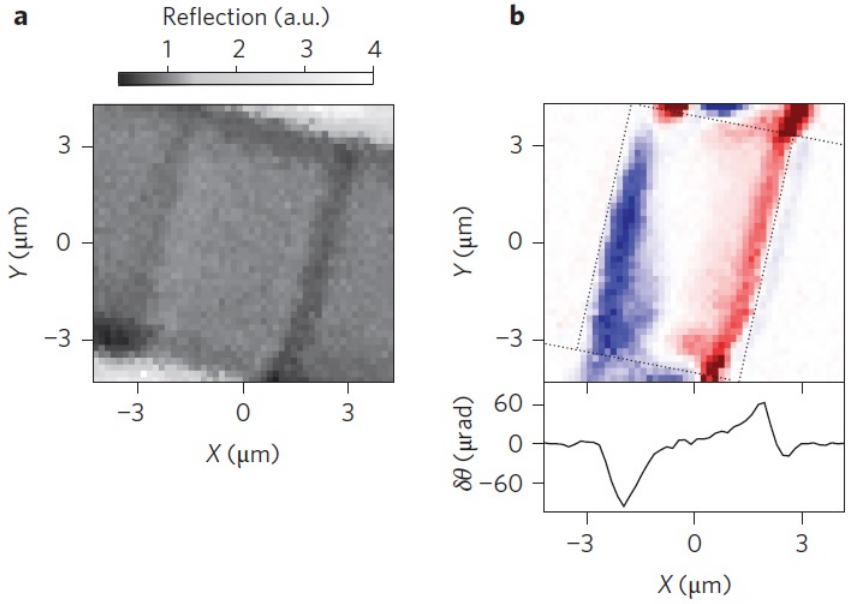

Figure 3.17: *Spin Hall Effect experiment result (a) 2D Reflectance imaging, (b) 2D Kerr imaging, of the whole bilayer MoS_2 bar plane (from [18])*

semiconductor sample.

Chapter 4

Charge and Spin-Valley Transfer in Transition Metal Dichalcogenides Heterostructure

Monolayer transition metal dichalcogenides (TMDC) offer new avenues to control valley and spin polarization based on their valley circular dichroism and spin-valley locking. In this context, interesting issues arise when two TMDC layers are stacked in a vertical heterostructure and interlayer charge transfer processes become possible. Now I explain the first half of main stem of this work, spin-valley transfer in TMDC heterostructure.

The original idea suggestion and optical study of this research was mainly done by myself-Kim Suk Hyun, and other Ph.D student assisted me - Elyse Barre and Burak Aslan, in Tony Heinz group, Department of Applied Physics, Stanford University and SLAC National Accelerator Laboratory. The sample stacking preparation was done

by Young Duck Kim, Dongjea Seo, in James Hone group, Department of Mechanical Engineering, Columbia University in the City of New York. The orignal sample growth was done by Kyungnam Kang, in Eui-Hyeok Yang group, Department of Mechanical Engineering, Stevens Institute of Technology.

4.1 Introduction

In our study, we investigate the spin-valley characteristics of charge transfer in MoS_2/WSe_2 heterostructure with similar technique as previous study, utilizing ultrafast pump probe spectroscopy in room temperature. In particular, when we excite the A exciton in WSe_2 with circularly polarized ultrafast pump radiation, we observed circular dichroism of probe pulse for both the A and B excitonic transitions in MoS_2 by making use of relatively close A and B exciton feature (small valence band splitting) of MoS_2, giving access both to the lower and upper split conduction band of electron receptor material MoS_2. (These signatures are not observed in either of the separated monolayers, verifying the role of transfer from one layer to another.) We confirmed that spin valley transfer happens even in room temperature as well, decays in few picosecond time scale. By comparing the opposite sign of A and B excitonic signal, we could conclude that spin information is only conserved while valley is lost without testing multiple samples. We confirmed the result by examining the influence of the relative crystallographic orientation in a number of different samples. We also discussed possible reason of fast decay of net spin population in MoS_2 conduction band.

Atomically thin monolayer transition metal dichalcogenides (TMDC) offer new

avenues to carry, store, and manipulate information in the form of valley and spin polarization, opening the gate of spintronics and valleytronics. [19] This represents a paradigm shift moving away from information processing through current charge based electronics. Based on the absence of inversion symmetry in crystal structure, local minima states of electrons in monolayer TMDC can take either K or K‘ valley, and these states can be optically excited selectively by circular polarized light since each valley exciton couples with different handedness of light [7]. By virtue of several hundreds of meV of large spin orbit coupling in valence band, each of valleys are assigned to spin up or spin down in degenerate band, forming so-called spin-valley locking. As a result, we can utilize the spin, valley, and layer indexes (in bilayer material) as an information carrier based on spin-valley circular dichroism and spin-valley locking, spin-layer locking. Such valley polarization-engraved information can be monitored by Photoluminescence [7] or Pump Probe Spectroscopy Kerr Rotation. [11] [12] Once the spin / valley initialized, such information can be controlled by external ultrafast light pulse, which can be used as a quantum gate.[20] New interesting issues arise when two TMDC layers are stacked to form a vertical heterostructure. Interlayer charge transfer processes become possible when the two stacked material has type-II band alignment. This phenomena has been observed in pump-probe spectroscopy in MoS_2-WS_2 stacking, by pumping only one layer and showing new peak arise in probe reflection spectral domain which have not been emerged in MoS_2 or WSe_2 separated monolayer material alone, which comes from charge transfer from originally pumped layer to another layer. [13] As a result of charge transfer, it became also possible to observe a significant photoluminescence signal peak around photon energy region well below both of energy band gaps of two monolayer materials. This new peak is

assumed to be originated from interlayer exciton, which consist of an electron and hole from opposite layers. The time-resolved PL signal have shown interlayer excitons have exceptionally long lifetimes over 1 nanosecond in 30 K, showing how hard the recombination of electron and hole in different layer is. It was also observed that two photoluminescence peaks of each materials are quenched by an order of magnitude due to fast charge transfer, reducing intra-layer excitons which produces original PL signal in recombination process. [21] Another way to see if two stacked monolayer TMDC interact is observing the electron wavefunction mixing and charge transfer in the reflection contrast. It has been observed that in MoS_2/WS_2 and $MoSe_2/WSe_2$ heterostructure, there are significant broadenings of linewidth in reflection contrast spectrum peak after the monolayer TMDC has been stacked to another material. Such broadening can be understood as originated from the decay of originally created intra-layer exciton through charge transfer process, since the amount of linewidth broadening is same as the estimated time scale of interlayer charge transfer, which are around 20∼35fs. [23] Combining these spin-valley degree of freedom and interlayer charge transfer, interesting issues arise the spin valley transfer in TMDC heterostructure. As stated in the Section 3.4. , recently there was one report that a charge transfer in $MoSe_2/WSe_2$ heterostructure is carrying not only charge itself but also spin valley information over the layers, observed by polarization sensitive CW laser pump probe spectroscopy at the temperature 30 K. They excited a given spin-valley state in one layer by circularly polarized radiation resonant with the relevant exciton, and measured co- and cross- circularly polarized light transmission to probe excitonic transitions in the other layer, examining the spin-valley characteristics of the interlayer transferred charge. However, the study could not offer an insight on

time resolved behavior of spin valley characteristic of electron since they have only done steady state observation with CW laser and giving access only to the lower spit conduction band of electron receptor material $MoSe_2$, required testing a number of heterobilayer samples with different relative crystallographic orientations to compare the degree of information conservation in spin and valley.

In the present work, we used femtosecond pulsed laser for the pump probe spectroscopy to have an insight to the time resolved dynamics of the spin valley charge transfer with the resolution up to about 1 picosecond, instead of CW laser which gives us only steady states result. As all the measurement here are taken under room temperature condition, this work paves the way for possible real device application, unlike the previous study under the cryogenic temperature only. By using wide probe spectral range which covers both A and B excitonic range of MoS_2, we could access to the spin valley conserving by one sample. In the previous study this could not be very clearly analyzed before measuring many sample.

We examine CVD grown MoS_2- WSe_2 heterostructures and check if they have enough wavefunction mixing between two layered materials for interlayer charge transfer by reflection contrast peak broadening and photoluminescence peak quenching. Then we test charge transfer from WSe_2 to MoS_2 more directly by pump-probe spectroscopy, observing newly emerged peak in probe reflection spectrum by pumping one layer, not present in either of separated monolayers. After confirming the interlayer charge transfer, we finally test the spin-valley transfer by measuring circular dichroism of heterostructure material which are pumped by circularly polarized pulse. Circular Dichroism is defined by reflection rate difference of left and right circularly polarized light, and it is a direct measure of valley imbalance of the TMDC

material, offering direct probe to the spin/valley transfer in heterostructure material. As all the measurement here are taken under room temperature condition, this work paves the way for possible real device application. We test the circular dichroism in time and probe wavelength (or probe photon energy) domain to better understand the dynamics of the highly valley polarized charges. We also examine large number of samples to see if there is any crystallographic dependence in spin/valley transfer in heterostructure material. As a back-up analysis, we try some fitting of the circular dichroism data and see how dielectric functions change before and after the charge transfer, by using real and imaginary dielectric function model of atomically thin layered material.

4.2 Sample Preparation

Here I briefly introduce the growth process of monolayer MoS_2 and WSe_2 and sample preparation of MoS_2-WSe_2 heterostructure. CVD growth of Monolayer WSe_2, tungsten source carrier chip (5nm WO3 thin film on 90nm SiO_2) was deposited on SiO_2 via electron beam evaporation. The tungsten source chip was covered, in face-to-face contact, by the silicon substrate. The sample was loaded into the center of the quartz tube and ceramic boat with 1 g of selenium powder was located upstream in quart tube. After loading, the furnace was heated up to 850°C in 1.6 Torr. 20 sccm of Argon gas and 15 sccm of Hydrogen gas were supplied to improve WO3 reduction. CVD growth of monolayer MoS_2, the SiO_2/Si substrate were O2 plasma-treated. Before the synthesis, MoO3 powder (Alfa Aesar, 99.995%, 10mg) was placed in an alumina boat close to the center of the heating zone of the furnace, and an alumina

boat containing sulfur powder (Alfa Aesar, 99.999%, 200mg) was placed upstream relative to the gas flow direction. Oxygen plasma treated 285 nm thick SiO_2/Si substrate were placed 10 cm from the edge of the alumina boat containing MoO3 powder. After purging the furnace with Argon gas for 10 minutes, the furnace was heated to 850 C with 100 sccm Ar. The Mono MoS_2 were then synthesized at 850°C for 30 minutes. After the synthesis process, the furnace was cooled to room temperature. In transfer process, we first spin coat a layer of poly methyl methacrylate (PMMA 950 A6) onto as grown MoS_2 films on SiO_2/Si substrate followed by a baking process at 180°C form 2 min. A water droplet is then dropped on the PMMA layer. The water may have a natural energy to penetrate between the MoS_2 film and the substrate due to different surface energies. And we can then readily scoop onto CVD grown WSe_2 sample. After that we bake the transferred assembly at 90°C for 10 minutes to remove water residues. The last step of the transfer process is dissolving the polymer with chloroform.

4.3 Basic Optical Characterization of the Heterostructure sample

4.3.1 Reflection Contrast

We first investigate the interlayer charge transfer itself in time and photon energy domain, regardless of spin/valley polarization. We prepared MoS_2- WSe_2 heterostructure sample by CVD growing separately on SiO_2 substrate and wet transfer MoS_2 on top of WSe_2. Monolayer flakes of MoS_2 and WSe_2 are the forms of regular triangle

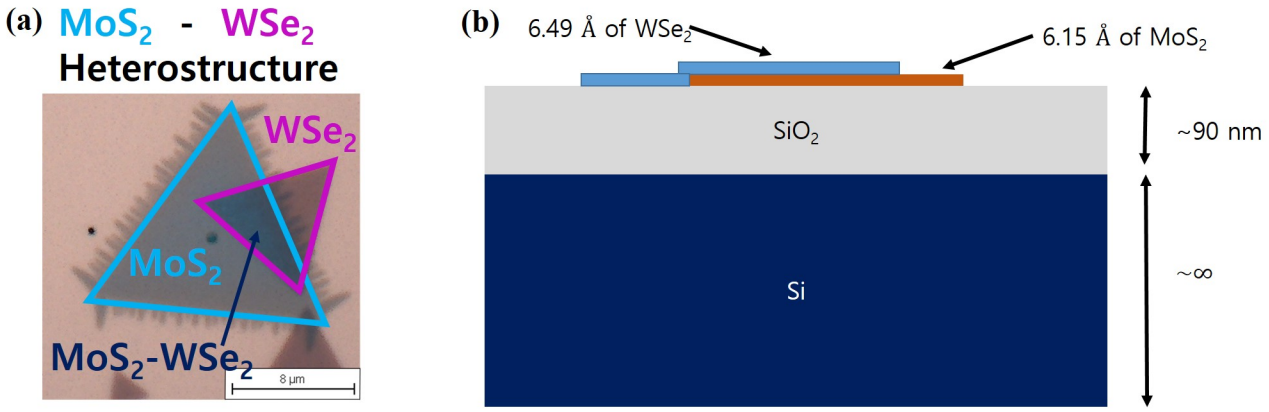

Figure 4.1: *MoS_2-WSe_2 Heterostructure Sample (a) Optical microscope image (b) Schematic side view*

with size 10∼20μm, and ∼5μm large overlapped heterostructure regions for optical measurement can be easily found so that there are ∼100 stacked region in 1 square centimeter large Si Substrate. (Fig 4.1.)

We took the reflection contrast spectrum of monolayer MoS_2, WSe_2, and their heterostructure with white light from a tungsten halogen lamp focused to 2∼3um. (Fig 4.2.)

We see A and B exciton peaks around 1.88eV and 2.02 eV in MoS_2 and 1.63eV and 2.05eV in WSe_2. Although they are all seen in heterostructure region, there are significant peak broadenings when compared to monolayer cases as we can see from the graph. Such broadenings were observed and reported earlier in [23], See Fig 4.3 for the results in the literature. The broadening can be observed in both MoS_2/WS_2 and $MoSe_2/WSe_2$, both on A and B exciton peaks. See Fig 4.4 for the detail.

We attribute such broadenings to the interlayer charge transfer serves as non-radiative decay channel of excited carriers. The broadenings of our samples in Fig

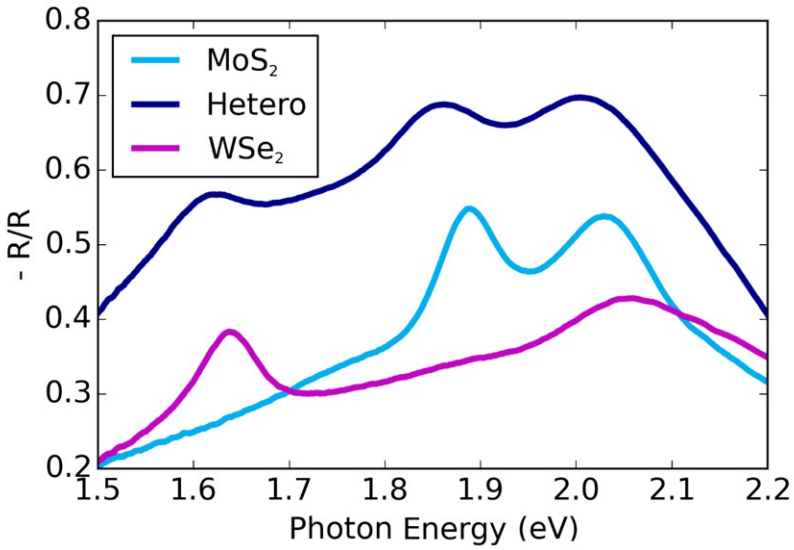

Figure 4.2: *Reflection Contrast signal of MoS_2-WSe_2 Heterostructure Sample, inverted by minus (-) sign.*

4.2. mean the layers are attached well so that they cannot be treated as separate layers without any interaction.

4.3.2 Interference effect analysis

Let us have a look in more detail including the sample-substrate interference effect. When the monolayer tmdc sample is placed on a thick transparent substrate like sapphire, the sample are seems more reflective and brighter, which means reflection contrast is positive sign. on the Si/SiO_2 substrate the sample area looks less reflective, darker, and shows different color. So we tried the Reflection contrast modeling of MoS_2 - WSe_2 Heterostructure sample with interference and dielectric function modeling. After we take Reflection Contrast (RC) measurement on the Si/SiO_2 substrate, we tried to fit the curve with the oscillator model, assuming the complex dielectric

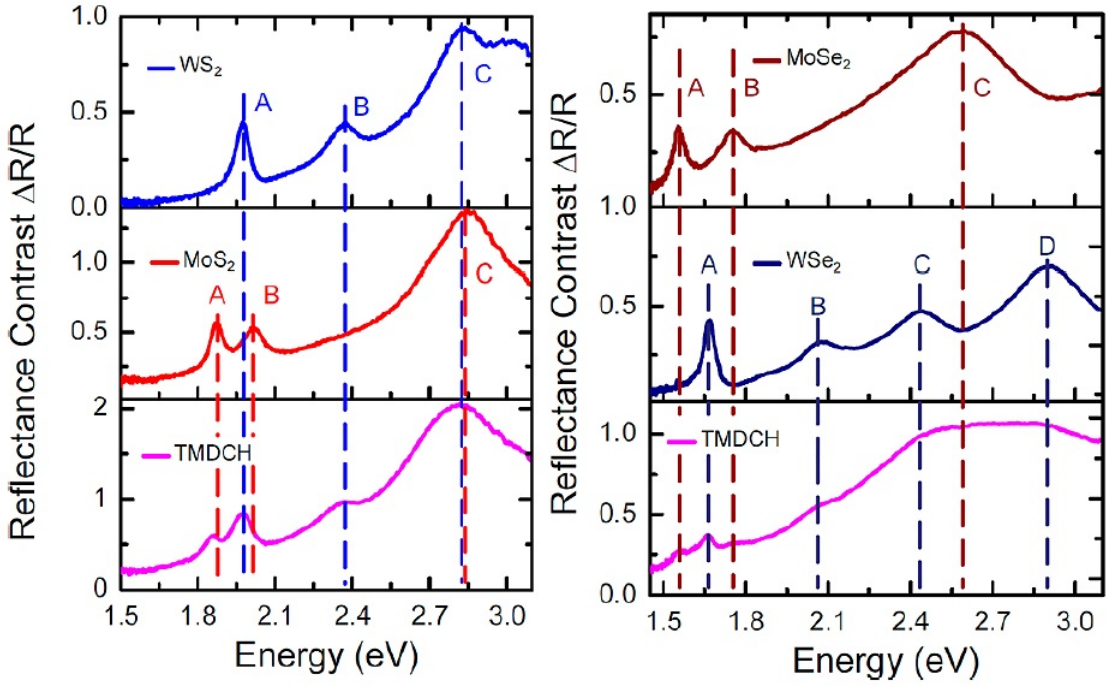

Figure 4.3: *Reflection Contrast signal of MoS_2-WS_2 Sample and $MoSe_2$-WSe_2 Sample, brought from [23]*

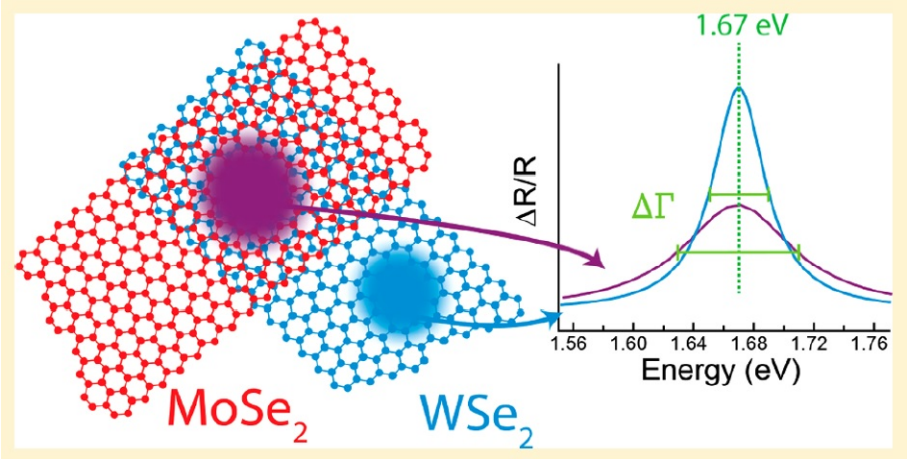

Figure 4.4: *Exciton linewidth broadening of $MoSe_2$-WSe_2 Sample, brought from [23]*

function of the TMDC materials to be sum of few Lorentzian oscillator functions which are KramersKronig constrained. [25] We assigned the Lorentzian oscillator for each different materials and excitonic ranges, like MoS_2 A, MoS_2 B, MoS_2 C, WSe_2 A, WSe_2 B,WSe_2 C, as shown in the Equation. 4.1, 4.2.

$$\epsilon_{MoS_2}(E) = \epsilon_{MoS_2,0} + \frac{f_{A,MoS_2}}{{E_{A,MoS_2}}^2 - E^2 - iE\gamma_{A,MoS_2}} + \frac{f_{B,MoS_2}}{{E_{B,MoS_2}}^2 - E^2 - iE\gamma_{B,MoS_2}} + \frac{f_{C,MoS_2}}{{E_{C,MoS_2}}^2 - E^2 - iE\gamma_{C,MoS_2}} \quad (4.1)$$

$$\epsilon_{WSe_2}(E) = \epsilon_{WSe_2,0} + \frac{f_{A,WSe_2}}{{E_{A,WSe_2}}^2 - E^2 - iE\gamma_{A,WSe_2}} + \frac{f_{B,WSe_2}}{{E_{B,WSe_2}}^2 - E^2 - iE\gamma_{B,WSe_2}} + \frac{f_{C,WSe_2}}{{E_{C,WSe_2}}^2 - E^2 - iE\gamma_{C,WSe_2}} \quad (4.2)$$

We also took account of the interference effect of SiO_2 layer by Transfer Matrix Method. [26] [27] The thickness of the materials shown in Fig. 4.1 are from the reference [25]. Equation. 4.3, 4.4 are the result of fitting of Monolayer MoS_2 and WSe_2 result, using three (A, B, C excitonic) oscillators for each of the graphs as written below.

With this model, we have got the fitting parameters:

$$\epsilon_{MoS_2,0} = 3.9$$
$$E_{A,MoS_2} = 1.89eV, \gamma_{A,MoS_2} = 0.071eV, f_{A,MoS_2} = 1.25eV^2$$
$$E_{B,MoS_2} = 2.0265eV, \gamma_{B,MoS_2} = 0.14eV, f_{B,MoS_2} = 2.81eV^2$$
$$E_{C,MoS_2} = 2.83eV, \gamma_{C,MoS_2} = 0.78eV, f_{C,MoS_2} = 79.7eV^2 \tag{4.3}$$

$$\epsilon_{WSe_2,0} = 14.1$$
$$E_{A,WSe_2} = 1.646eV, \gamma_{A,WSe_2} = 0.068eV, f_{A,WSe_2} = 0.80eV^2$$
$$E_{B,WSe_2} = 2.055eV, \gamma_{B,WSe_2} = 0.18eV, f_{B,WSe_2} = 1.67eV^2$$
$$E_{C,WSe_2} = 2.38eV, \gamma_{C,WSe_2} = 0.7eV, f_{C,WSe_2} = 22.7eV^2 \tag{4.4}$$

Fig. 4.5 (a), (b) show the fact that we can explain the reflection contrast so well even with this simple dielectric function model.

However Fig. 4.6 tells that this model with same parameters shows some deviation with the experimental result in heterostructure region. This is because interlayer charge transfer serves as non-radiative decay channel of excited carriers, inducing

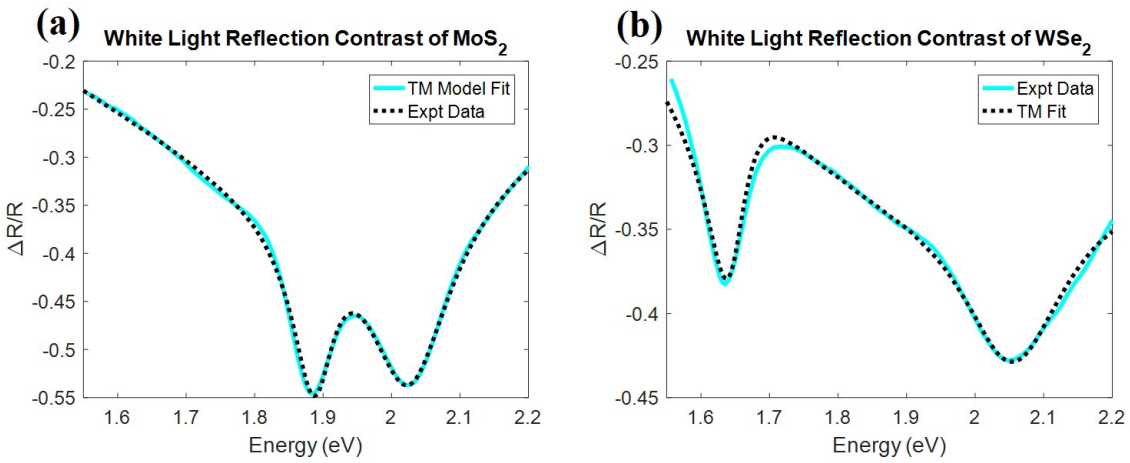

Figure 4.5: *reflection contrast data of (a) MoS_2 and (b) WSe_2 with graph fitting with the fitting parameters of Equation. 4.3, 4.4.*

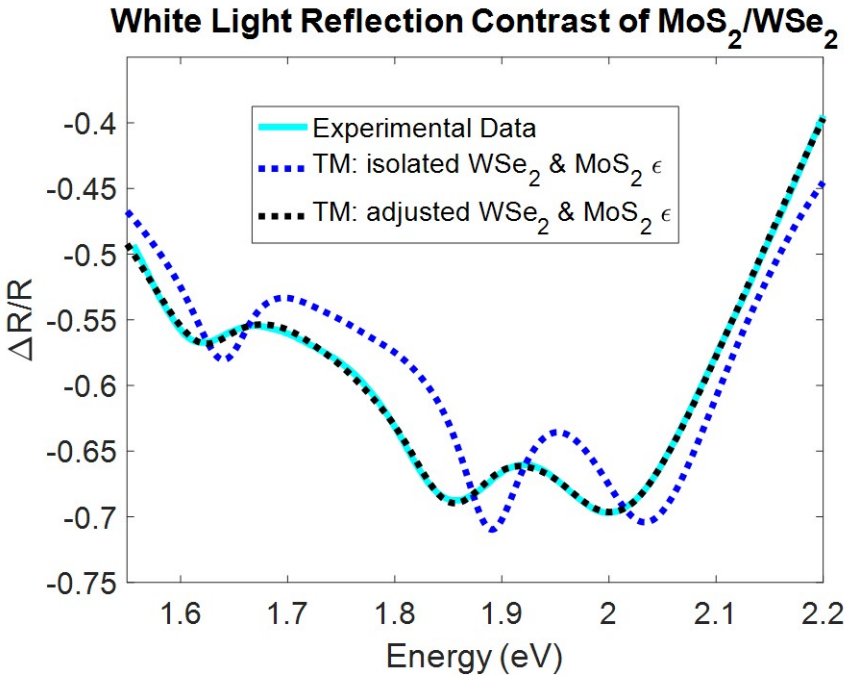

Figure 4.6: *reflection contrast data of MoS_2 - WSe_2 Heterostructure with graph fitting with the original and adjusted fitting parameters*

exciton linewidth broadening [4], requires some adjusting of the dielectric function parameters. Fig. 4.6 shows well fitted model curve again, with adjusted parameters to:

$$\begin{gathered}\epsilon_{MoS_2,0} = 4.7 \\ E_{A,MoS_2} = 1.85eV, \gamma_{A,MoS_2} = 0.1eV, f_{A,MoS_2} = 1.22eV^2 \\ E_{B,MoS_2} = 2.00eV, \gamma_{B,MoS_2} = 0.168eV, f_{B,MoS_2} = 2.81eV^2 \\ E_{C,MoS_2} = 2.81eV, \gamma_{C,MoS_2} = 0.422eV, f_{C,MoS_2} = 100eV^2\end{gathered} \tag{4.5}$$

$$\begin{gathered}\epsilon_{WSe_2,0} = 7 \\ E_{A,WSe_2} = 1.63eV, \gamma_{A,WSe_2} = 0.11eV, f_{A,WSe_2} = 1.22eV^2 \\ E_{B,WSe_2} = 2.055eV, \gamma_{B,WSe_2} = 0.255eV, f_{B,WSe_2} = 2.44eV^2 \\ E_{C,WSe_2} = 2.36eV, \gamma_{C,WSe_2} = 1.03eV, f_{C,WSe_2} = 27.4eV^2\end{gathered} \tag{4.6}$$

We did not have to change the B excitonic parameters of WSe_2. We estimate the non-radiative decay time constants by $\tau = \hbar/\Delta\gamma$ where $\Delta\gamma$ is the increased amount of linewidth γ, giving:

$$\tau_{A,MoS_2} = 22.7fs, \tau_{B,MoS_2} = 23.5fs, \tau_{A,WSe_2} = 15.7fs, \tau_{B,WSe_2} = 8.78fs \tag{4.7}$$

which are similar values as in the previous researches [23] etc., showing that we have nice quality of heterostructure sample with interlayer interaction. With the range of Si/SiO_2substrate thickness and reflective index in this work, the Reflection contrast curve is almost equal to just upside down graph of the thick transparent substrate, in the case that the reflection ratio is proportional to the absorption curve. We will consider the optical reflection spectroscopy curve by the sample on the Si/SiO_2 substrate as the original samples absorption curve unless otherwise specified.

4.3.3 Photoluminescence

We additionally examined these three regions with photoluminescence spectroscopy (PL) as well, since we expect some quenching of PL signal with the charge transfer induced non-radiative decay channel.

In Fig 4.7 we can see that heterostructure sample PL graph has characteristic peaks which are from monolayer samples, but in the stacked region the PL signals are quenched by 1$\sim$2 order of magnitudes from monolayers, especially by 1/30 in

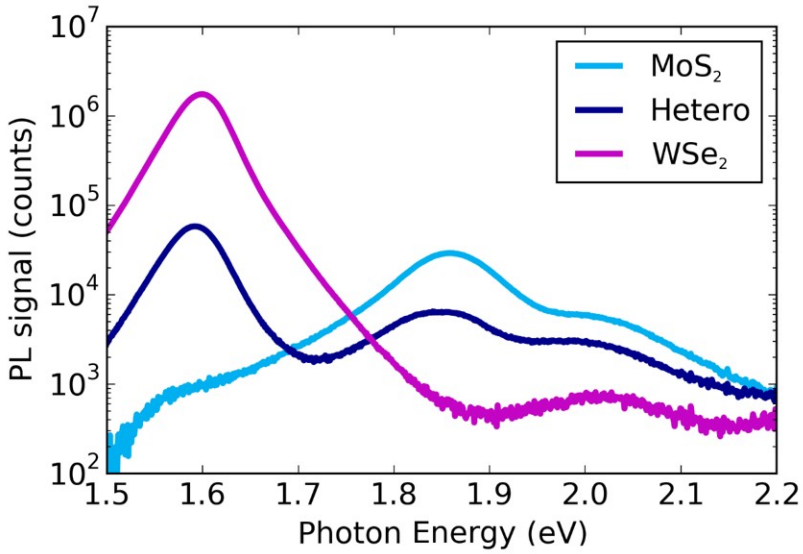

Figure 4.7: *PL data of MoS_2 - WSe_2, and their Heterostructure. The PL signal is quenched by orders of magnitude in the Heterostructure region.*

WSe_2 A exciton peak and by 1/6 in MoS_2 A exciton peak, confirming again the heterostructure samples are stuck well for charge transfer.

4.4 Charge Transfer observed by Pump Probe spectroscopy

After we characterize the sample with RC, PL spectroscopy, we made use of ultrafast femtosecond laser optics to further investigate the interlayer charge transfer. Then we move onto the spin/valley character of the carrier transfer. The sample were excited by 1.61eV pump pulse which is set to match with A exciton energy to test the charge transfer from WSe_2 to MoS_2, and broadband probed within 1.77eV $\sim$ 2.13eV.

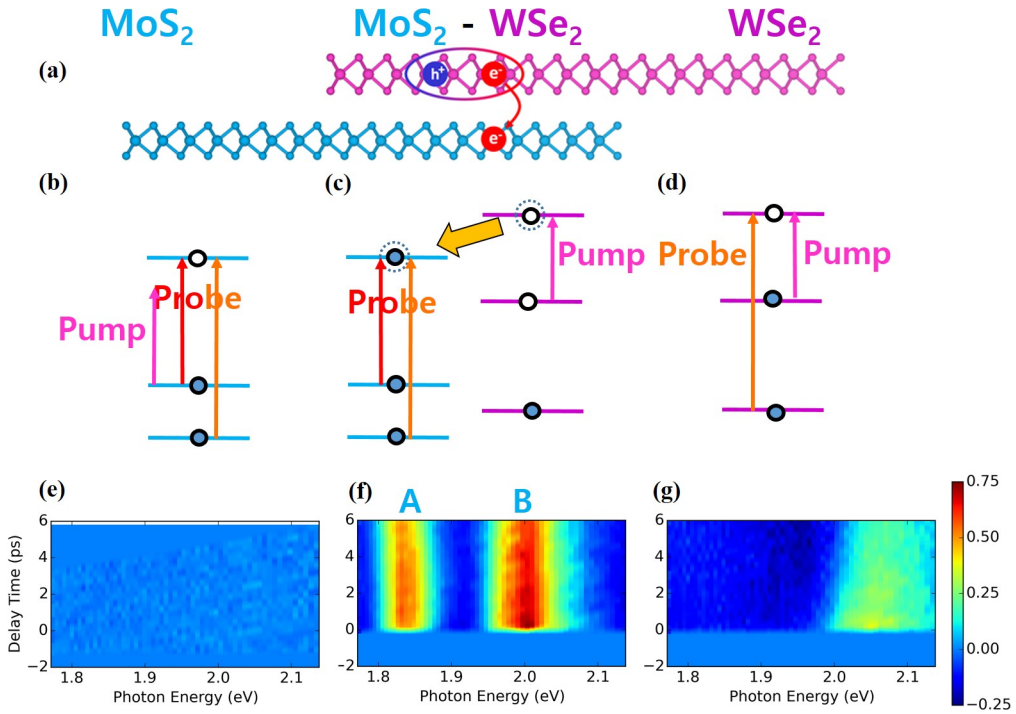

Figure 4.8: *Charge Transfer in MoS_2- WSe_2 Heterostructure. (a) Schematic of charge transfer in TMDC heterostructure. Photo-excited electron in WSe_2 layer transfers to MoS_2 layer, leaving its pair hole in WSe_2. (b)-(d) Band Diagram representation of Pump-Probe Spectroscopy in MoS_2 monolayer, MoS_2- WSe_2 Heterostructure, and WSe_2 monolayer, with the pump pulse resonant with WSe_2 A exciton energy (1.61eV of photon energy). (b) In case of MoS_2 monolayer, since it requires far greater energy to excite either A exciton (1.83eV) or B exciton (2.00eV) range, the conduction band electron population remains unchanged and we do not see any significant probe signal change. (c) In case of WSe_2 monolayer, as the conduction band was populated by the electron from A excitonic range of WSe_2 (1.61eV), the probe absorption in B exciton range of WSe_2 (2.05eV) is decreased and reflection is increased with hindered excitation of electron caused by Pauli blocking. (Right side) (d) Finally, In case of MoS_2- WSe_2 Heterostructure, pump-excited electron in WSe_2 conduction band transfers immediately to the MoS_2 conduction band, causing reflection increasing in both A and B exciton range of MoS_2 by the Pauli blocking same as in (c). (e)-(g) Pump-induced Probe signal change ratio in percentage (%), 2D color mapped on delay time and photon energy domain, backing up the ideas of (b)-(d), which are taken on (e) MoS_2 monlayer, (f) MoS_2- WSe_2 Heterostructure, and (g) WSe_2.*

Fig 4.8 (a) illustrates how pump pulse induced photo-excited electron moves from one layer to another, leaving photo-excited hole in original layer. Both pump and probe beams were linearly polarized in same direction to eliminate any circular polarization effect. We then measure reflection change ratio, ΔR/R, where R is the original reflectance and ΔR is the pump induced change of reflectance. The methodology of the Ultrafast Optical Measurement in this work is following. Femtosecond ultrafast pulses at the wavelength 1,030 nm were generated by a fiber based amplifier system (IMPULSE Femtosecond Laser by Clark MXR). The laser pulses with 100 femtosecond pulse duration at the repetition rate 1 MHz, are focused into an undoped YAG crystal to generate a supercontinuum white light, and are split into two beams by a beamspiltter. One is amplified by NOPA (Non-linear Optical Parametric Amplifier) system and bandpass filtered to become strong 770nm (10nm FWHM) near-infrared laser for pump beam, and the other was guided into a long focused monochromator (Shamrock 500i by ANDOR, Oxford Instrument) and was gathered at the other side of the monochromator with a convex lens to select a specific wavelength with $\sim$1nm resolution from 580nm to 700nm for probe pulses. The pump and probe beams were focused at the sample with a micrometer objective lens into the circular beam spot with diameter $\sim 2\mu m$. The intensities of the beams were about $\sim 20\mu W$ for pump and $\sim 1\mu W$ for probe just before the sample. The probe light was detected by a Si-based photodiode, with a 700nm short-pass filter to filter out the pump pulse. The pump-probe time delay was controlled by a motorized linear delay stage and the pump probe signal was recorded using lock-in amplifier with a mechanical chopper in a frequency of 700 Hz. The time delay and probe wavelength control and data mining were automatically processed with computer using LabVIEW. In

charge-transfer experiment, we linearly polarize both pump and probe beam in same direction to get rid of any circular polarization dependent effect. The MoS_2 alone sample does not show any reasonable signal the region of interest (Fig 4. 8 (e)), because both A and B exciton energy gaps are much higher than pump photon energy and cannot be excited by pump alone. (Fig 4.8 (b)) In contrast, the WSe_2 sample shows some peak around 2.07 eV, corresponds to increasing of reflection around B exciton energy of WSe_2. (Fig 4.8 (g)) This peak corresponds to the effect that A exciton formation filled the conduction band with electron, repulses the electron which wants to be excited to conduction band by Pauli blocking, hindering the B exciton formation, decreasing the absorption and increasing the reflection around B exciton energy. (Fig 4.8 (d)) Finally, the MoS_2 - WSe_2 heterostructure region shows two high peaks in 1.84eV and 2.00eV, corresponds to increasing of reflection around B and A exciton energy of MoS_2, respectively. (Fig 4.8 (f)) This peaks were neither observed in separated MoS_2 nor WSe_2 alone region, showing the exotic nature of heterostructure material. We attribute the peaks to be the transfer of conduction band electrons from WSe_2 A to MoS_2 conduction band. (Fig 4.8 (c)) The electron-filled conduction band hinders the excitation of electron to conduction band both from A and B valence band, suppressing the A and B exciton formation, decreasing the absorption and increasing the reflection around A and B exciton energy of MoS_2. (Fig 4.8 (c)) Not only the 1.84eV MoS_2 B exciton peak, but 2.00eV MoS_2 A exciton peak is also clearly distinguishable with 2.07eV WSe_2 B exciton peak. (Fig 4.8 (g).)

See also Fig 4.9 for the time sliced graph, the Transient Reflection in maximally excited time for MoS_2, WSe_2, and Heterosturcture. Fig. 4.9 shows the transient reflection signal verses probe photon energy in 3 regions at the maximally excited

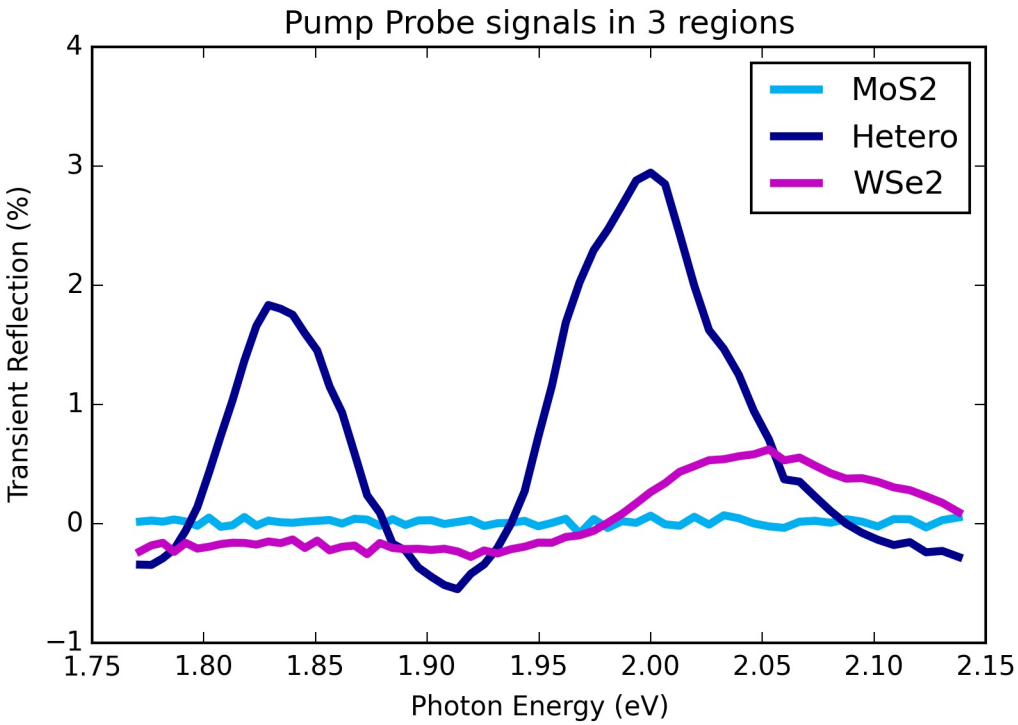

Figure 4.9: *Transient Reflection in maximally excited time for MoS_2, WSe_2, and their Heterosturcture*

time (near time zero∼2ps). MoS_2 does not show significant signal. WSe_2 curve show some peak centered at 2.05eV which corresponds to WSe_2 B excitonic range, heterostucture curve show two strong peak centered at 1.83eV and 2.00eV which corresponds to MoS_2 A and MoS_2 B excitonic range showing clear distinction from WSe_2s, giving the evidence of interlayer charge transfer. This unique emergence of peak ensures the fact that the peaks are from combinational effect of MoS_2 and WSe_2.

4.5 Spin/Valley Transfer observed by Circular Dichroism spectroscopy

4.5.1 Method- revisited

Here we address the question of whether the spin and valley characteristics of photoexcited carriers are persevered under interlayer charge transfer, since it is not very obvious if the information is still unaltered after the interlayer charge transfer. In order to observe the interlayer spin/valley binary information transfer, we again utilized ultrafast pump-probe measurements, exciting a given spin-valley state in one layer by circularly polarized radiation resonant with A exciton. The spin-valley characteristics of the transferred charge are examined through the induced Circular Dichroism for resonant probing of excitonic transitions in the other layer. Circular Dichroism (CD) is defined by

$$\eta = (\Delta R/R)_{\sigma+probe} - (\Delta R/R)_{\sigma-probe} \tag{4.8}$$

which is the difference of reflection change ratio between left ($\sigma+$) circularly polarized probe and right ($\sigma-$) circularly polarized probe. The measurement is possible by an optical bridge at once since linearly polarized probe beam is in fact a superposition of $\sigma+, \sigma-$ probes. We simply keep the pump and probe wavelength unchanged, but use pump light into circularly polarized by Soli-Barbinet compensater before it enters the sample instead of original linearly polarized light. In order to make the pump beams circularly polarized just in front of the sample, the pump beam were first linearly polarized by a polarizer and passed the Soli-Barbinet compensator, a continuous variable waveplate.

The detection of the Circular Dichroism was done using optical bridge, which make the probe light linearly polarized with a polarizer, gathers the probe beam after it was reflected to the sample, and let it pass through Wollaston prism with the axis making 45° to the polarization axis to split the beam into two beams with equal intensities and polarization which are perpendicular to each other. The two beams are monitored by two separate photodiodes, and the signal difference is extracted and amplified by low-noise amplifier, sending the signal into lock-in amplifier. This is the scheme to measure the Kerr Rotation of the sample, but this setup can be converted to measure the Circular Dichroism by inserting Fresnel Rhomb just before the Wollaston prism, a broad wavelength quarter-wave plate.

4.5.2 Result

Now we move onto the actual result and some explanation about spin-valley transfer. Fig 4.10. shows the result of delay time dependent circular dichroism, with probe filtered at 1.82eV ± 0.013eV (680nm ± 5nm).

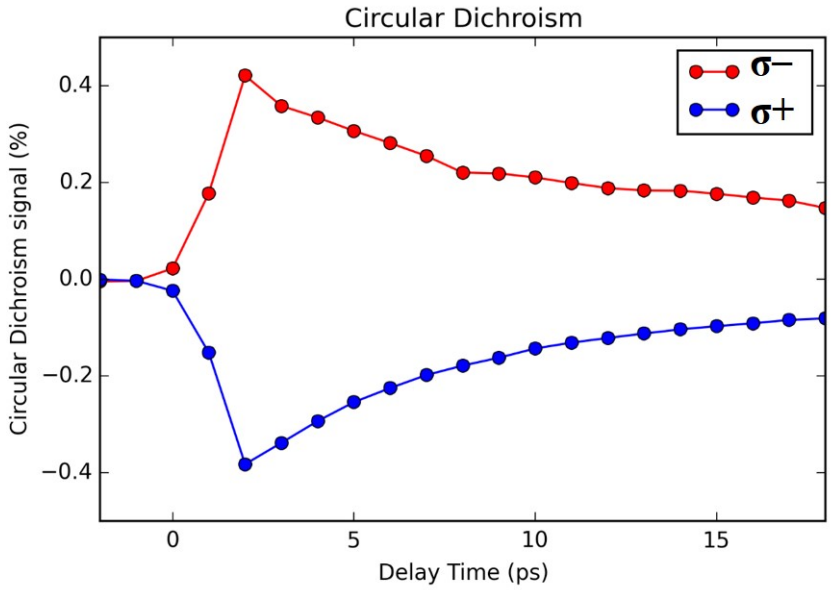

Figure 4.10: *Pump-induced Circular Dichroism of Probe signal in percentage (%) for pump energy 1.82eV ± 0.013eV (680nm ± 5nm), as a function of delay time. CD signal shows exponential decay with time constant ∼10ps, with two opposite signs of pump helicity*

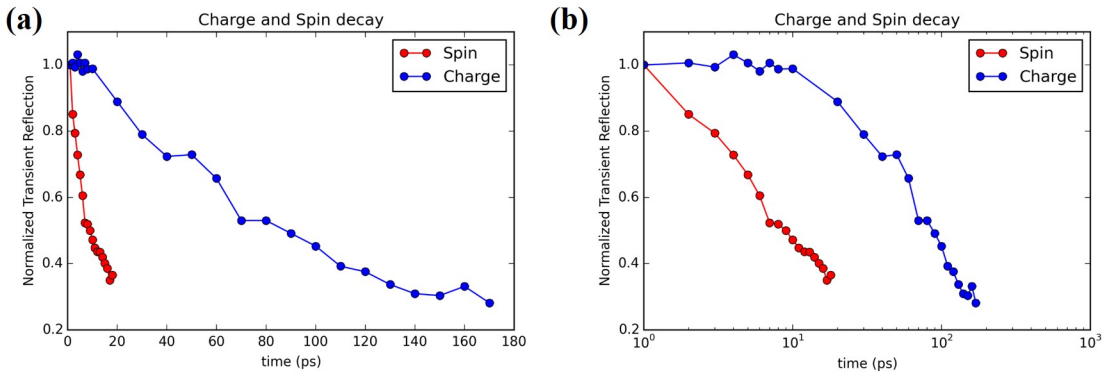

Figure 4.11: *Charge (No Circular Polarized Pump and Porbe) and Spin Valley (CD) time dependence (a) normal (b) time log scale*

We confirmed that the overall graph shape of CD signal flips to change the sign when the pump is change from left circular polarized one to right circular polarized one, insures that the observed CD signal is essentially spin-valley mediated effect. See Fig 4.11 for the time behavior of the signal. The spin valley transfer induced circular dichroism signal exhibited lifetime about 10ps, in contrast of Charge transfer induced transient reflection signal with the lifetime at least hundreds of picosecond.

Fig 4.12 shows the possible model to describe the mechanism of pump-induced circular dichroism of probe signal in MoS_2- WSe_2 heterostructure with band diagram picture. We call this as valley-dominant model, assumes the crystal momentum to be nearly strictly conserved while spin decays fast so that we can ignore it. Left ($\sigma+$) circular polarized pump pulse resonant with WSe_2 A exciton energy, excites electrons in WSe_2 K valley and interlayer transfer process sends them to MoS_2 conduction band. In case of parallel aligned crystal ($\theta = 0$ deg), electrons in WSe_2 +K valley will be transferred only to same +K valley of MoS_2 due to momentum conservation. As a result, the absorption of probe pulse in A exciton range will be effected only in

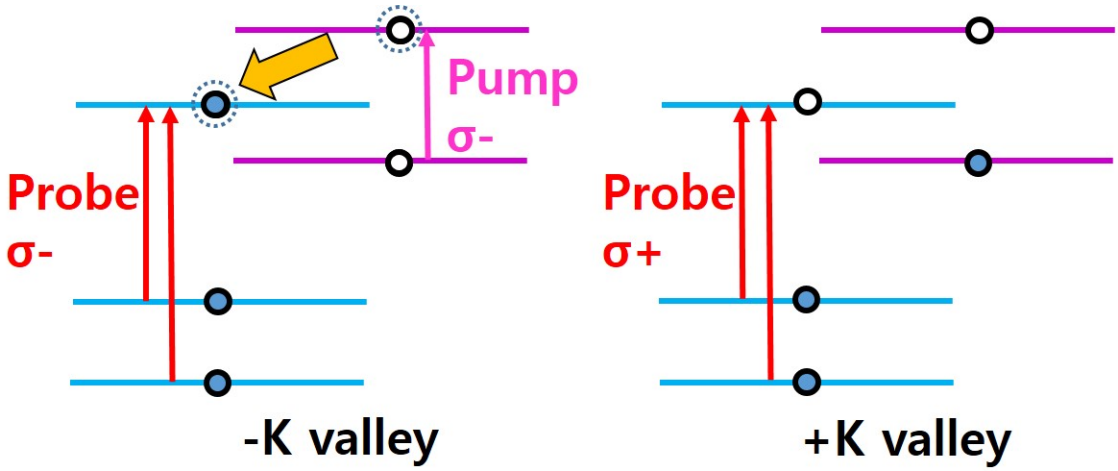

Figure 4.12: *(Original) Valley dominant model. Band Diagram representation of Pump-induced Circular Dichroism of Probe signal in MoS_2- WSe_2 Heterostructure, with the pump pulse resonant with WSe_2 A exciton energy (1.61eV of photon energy). Left ($\sigma+$) circular polarized pump (pink arrow) excited electrons in WSe_2 +K valley would be interlayer transferred (yellow arrow) to same +K valley of MoS_2 conduction band, assuming well aligned crystals. (Spin indexes are assumed to be quickly randomized and were not considered here) Then probe pulse induced excitation of MoS_2 A exciton energy (shorter red arrows) is hindered by Pauli blocking only at +K valley by the repulsion of electrons, increasing the reflection of left ($\sigma+$) circular polarized probe, creating Circular Dichroism(CD). In this model, the CD of MoS_2 B exciton (longer red arrows) energy will be same sign from the commensurate selection rule for A and B valence band.*

left ($\sigma+$) circular polarized probe. This model can describe the existence of CD signal in A excitonic range as in Fig 3 (a), and flipping of CD with flipping pump helicity. In this valley-dominant model, the sign of the CD signal in B excitonic range would be the same as that of A excitonic range, because of same selection rule for A and B valence band. However, the experimental result shows CD signal around A and B exciton appears with opposite sign, contradicts with the model.

Fig 4.13 shows the result of delay time and photon energy dependent circular dichroism of probe beam, induced by left circularly polarized pump beam pulse. Red (Blue) colored positive (negative) signal means left (right) circular polarized pump beam has greater reflectance. We observe circular dichroism of probe pulse for both the A ($\sim$ 1.85 nm) and B excitonic ($\sim$2.00eV) transitions in MoS_2. CD signal changes the sign as we follow the photon energy axis, from positive around A exciton range to negative around B exciton range, showing clear contrast to the charge transfer case with two positive peaks at both A and B exciton energy that we have seen before.

4.6 Analysis

Fig 4.14 shows the Lorentzian fitting of the time sliced data in Fig 4.13 at the maximum signal. The Red and Green curve shows the peaks at A and B exciton energy, showing that the signal can be nicely fitted with two peaks with opposite signs. The Lorentzian fitting gives us the peaks area in the photon energy domain, spectrally integrated signal. Since we get two peaks with opposite signs for each time slice, we can trace the A magnitude and B magnitude for each time. Fig 4.15 shows the time dependent magnitude of CD signal in A and B obtained by that method. Because

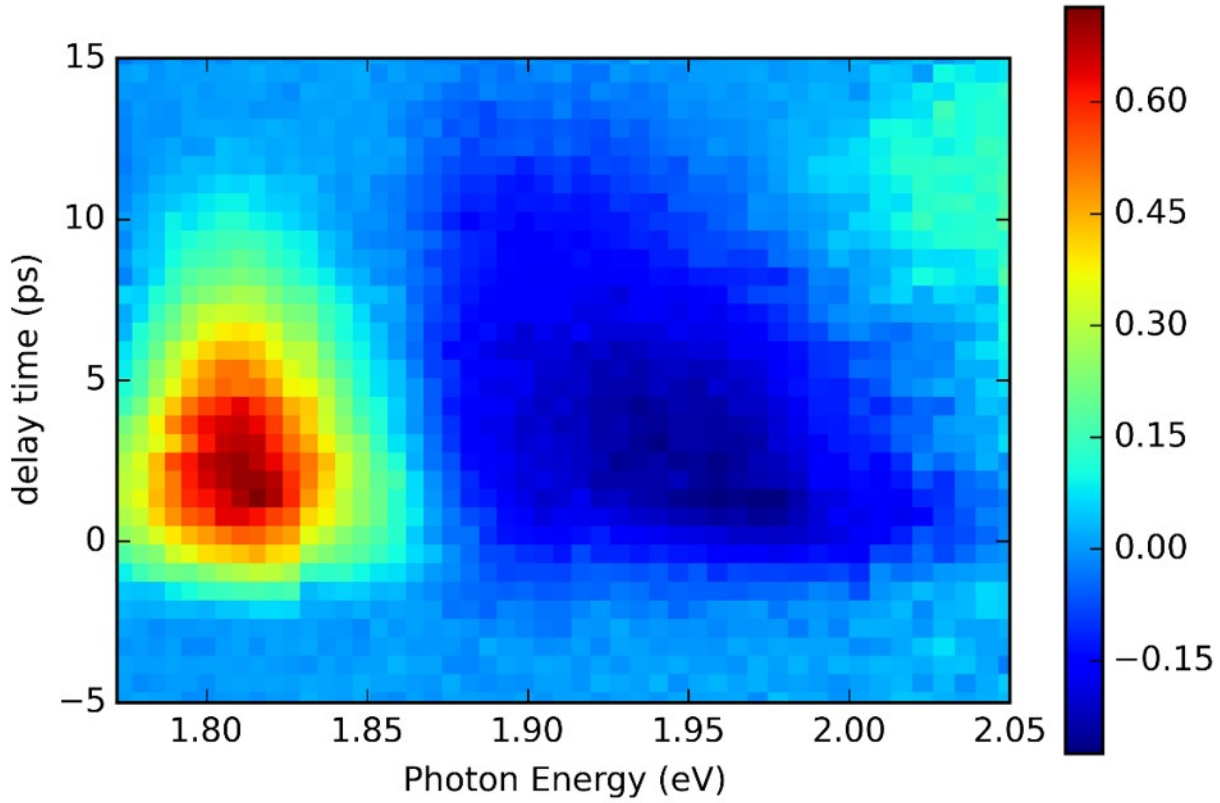

Figure 4.13: *Pump-induced Circular Dichroism of Probe signal in percentage (%), 2D color mapped on delay time and photon energy domain. CD signal shows opposite signs for A and B exciton range in time zero, contradicts with model in Fig 4.12.*

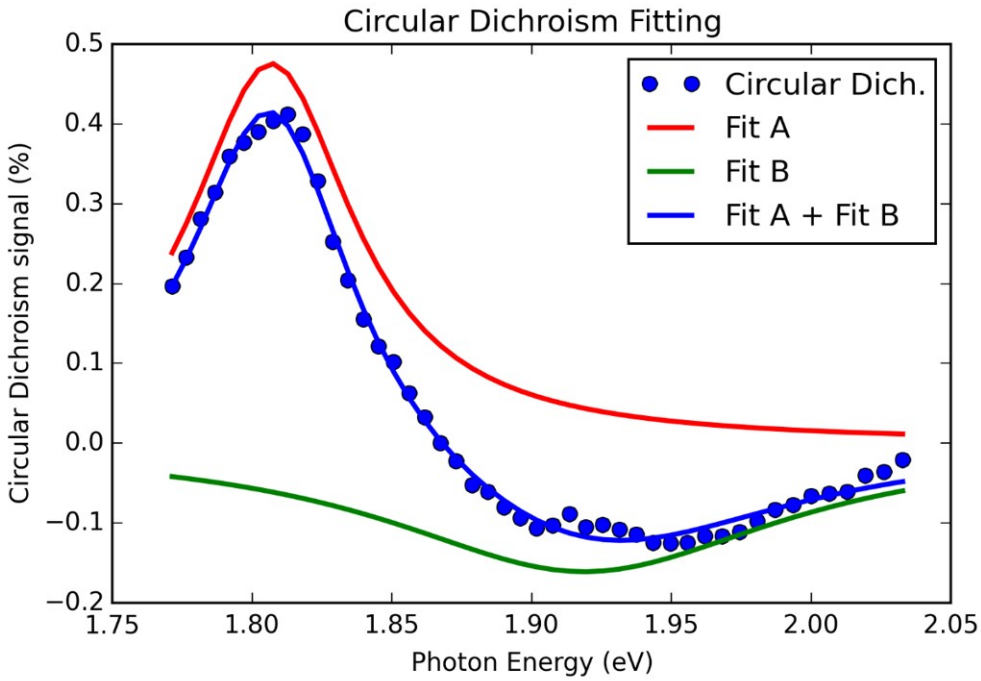

Figure 4.14: *Lorentzian fitting of the time sliced data in Fig 4.13 at the maximum signal*

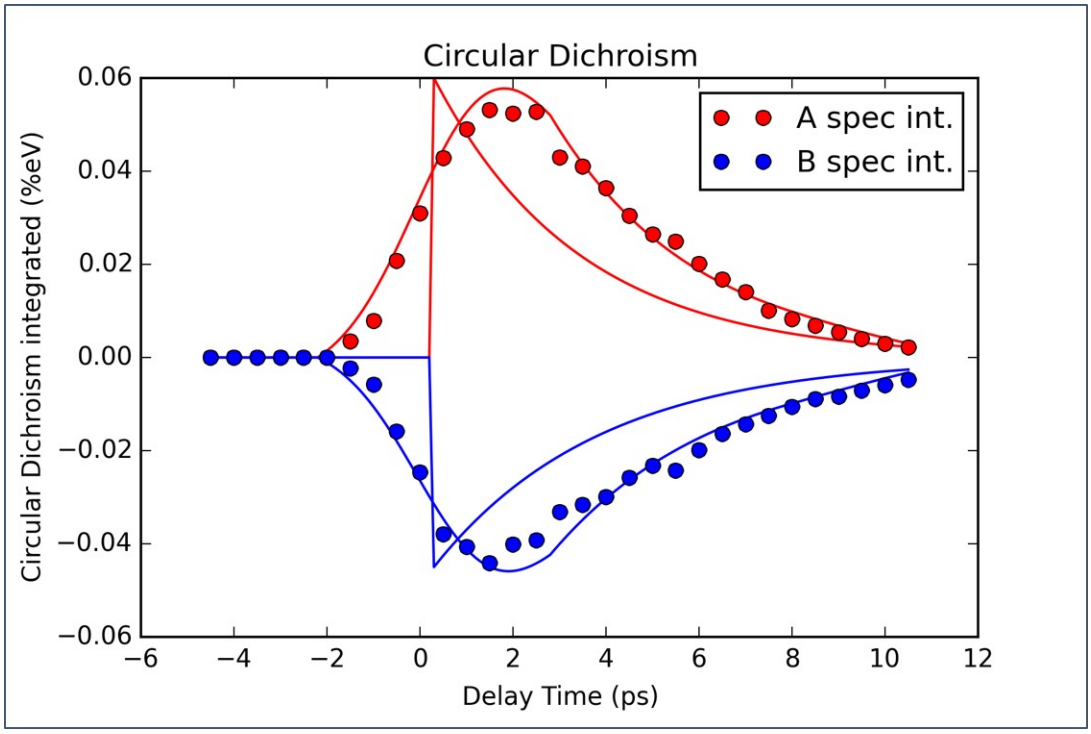

Figure 4.15: *time dependent magnitude - spectrally integrated CD signal, from the same fitting in Fig 4.14*

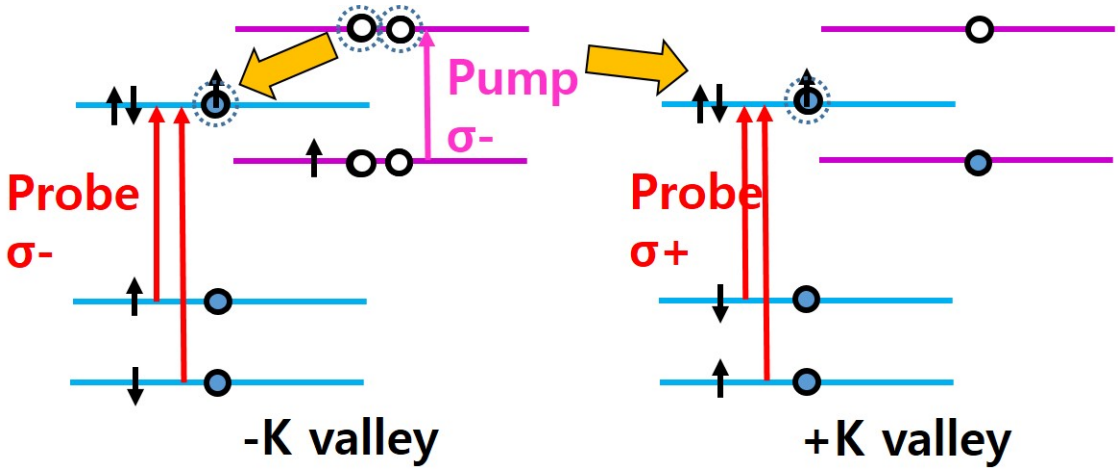

Figure 4.16: *(Alternative) Spin dominant model. Photo-excited electrons in WSe_2 +K valley have spin up orientation, and they are interlayer transferred to MoS_2 conduction band, being distributed to +K and K valley equally (two yellow arrows) through both co-valley and cross-valley channel by virtue of phonon scattering in room temperature, with preserved spin up orientation. Then probe pulse induced excitation of MoS_2 A exciton energy (red arrows) is Pauli blocked only at +K valley by the repulsion of electrons occupying same spin up states as in the valence band, increasing the reflection of left(σ+) circular polarized probe. In this model, the CD of MoS_2 B exciton (longer red arrows) energy will be opposite sign by the opposite spin-valley locking for A and B valence band, matches with the result as in Fig 4.13.*

of the broadening of the laser pulse width by the monochromator, we modeled the immediate pump probe response and blurred by pulse width model. (we assumed the finite response time does not play important role in this experiment.) The data fits well with the assumption of same decay time ∼3ps, same amplitude, and opposite signs for A and B signal, blurred by pulse width ∼2ps. Since the monochromator had the seeting of 1nm resolution and it corresponds to the time ∼2ps, we consider this as a reasonable fitting.

This phenomena can be understood by introducing alternative model called

spin-dominant model (Fig 4.16), assumes the valley to be depolarized fast by excessive room temperature phonon momentum, while spin indexes are well conserved over at least several picosecond. In this model we assume that populated electrons in WSe_2 +K valley are transferred to ±K valley equally, with preserved spin up orientation. We attribute such a valley distribution to room temperature phonon, since they were predicted to have momenta large enough to scatter electrons between K and +K valley in a simulation literature. [24]

The bosonic, spinless nature of phonon makes us think the electron spins to be well conserved. Probe pulse induced electron excitation at MoS_2 A exciton energy is Pauli blocked dominantly at K valley by electrons occupying same spin up states, increasing the reflection of left ($\sigma+$) circular polarized probe. Since the valence band spin has opposite orientation at A and B valence band, the CD of MoS_2 B exciton energy shows flipped sign, increasing the reflection of right ($\sigma-$) circular polarized probe. We have got the result that among the spin and valley it is spin with is preserved well during the first ∼1ps of the charge transfer, with measuring only one sample. The previous study in Section 3.4. also arrived to the same idea with different material combination, but the study was tied to steady state observation using CW laser, and required multiple measurements on many samples with different crystal angles. Investigation to the time behavior with finer resolution could not be done by the instrumental limitation, which suggested a goal for the future research project.

As a double check, we have also examined the influence of the relative crystallographic orientation of the two layers on the transfer process using a large number of different heterostructure samples, backing up the alternative model. Fig 4.17 shows the relation between the crystal twisted angle and CD signal amplitude and decay

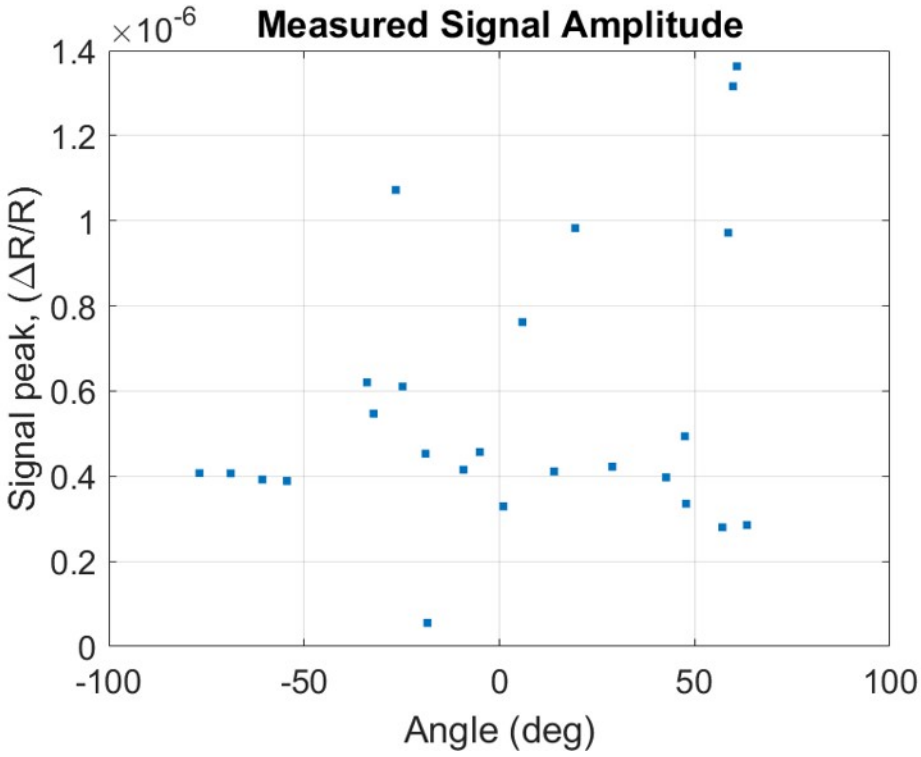

Figure 4.17: *Crystal orientation angle dependence of circular dichroism signal amplitude, without any clear trend of crystal angle.*

time constant, using with probe filtered around A exciton peak, at 1.82eV ± 0.013eV (680nm ± 5nm). We can see that the CD signals are largely independent of the crystal twisted angle, agrees with the spin conservation dominant model assuming the fast valley depolarization, suppression of valley dependent CD by momentum conservation.

Here is a closer look on the band diagram and more detailed explanation. Fig 4.18 shows the detailed look in MoS_2 conduction band. We have considered the MoS_2 conduction band to be spin degenerate for simplicity. Since the splitting is few meV which is about the size of room temperature kT, it is might be a good approximation, but let us consider the separation from now. Since the spin splitting in $MoSe_2$ conduction band in previous study in Section 3.4 is few tens of meV, and since the temperature was 30K, whose kT = 2.5meV, the transferred electron likes to go the lower split band (dark blue colored) as shown in Fig 4.18 (a). With this favor to the lower band, the spin conservation led the election to go to one valley only. (Strictly speaking, by some depolarization, the ratio was measure to be 100: 37.) The upper band (sky blue colored) dynamics and valley distribution of the transferred electron is unclear in this testbed. What will be the destination of the electron if the upper band is also a possible option? Fig 4.18 (b), (c), (d) are the result if the electron strictly follows the spin only, valley only, and spin & valley conservation. Since we can measure the time dynamics with the pulse laser pump probe, not only the destination but also the intermediate pathway might be seen. The result we have seen is the electron goes to both of the valley almost equally (the equal magnitude of the A and B signal) with the spin conservation, supporting the model in Fig 4.18 (b).

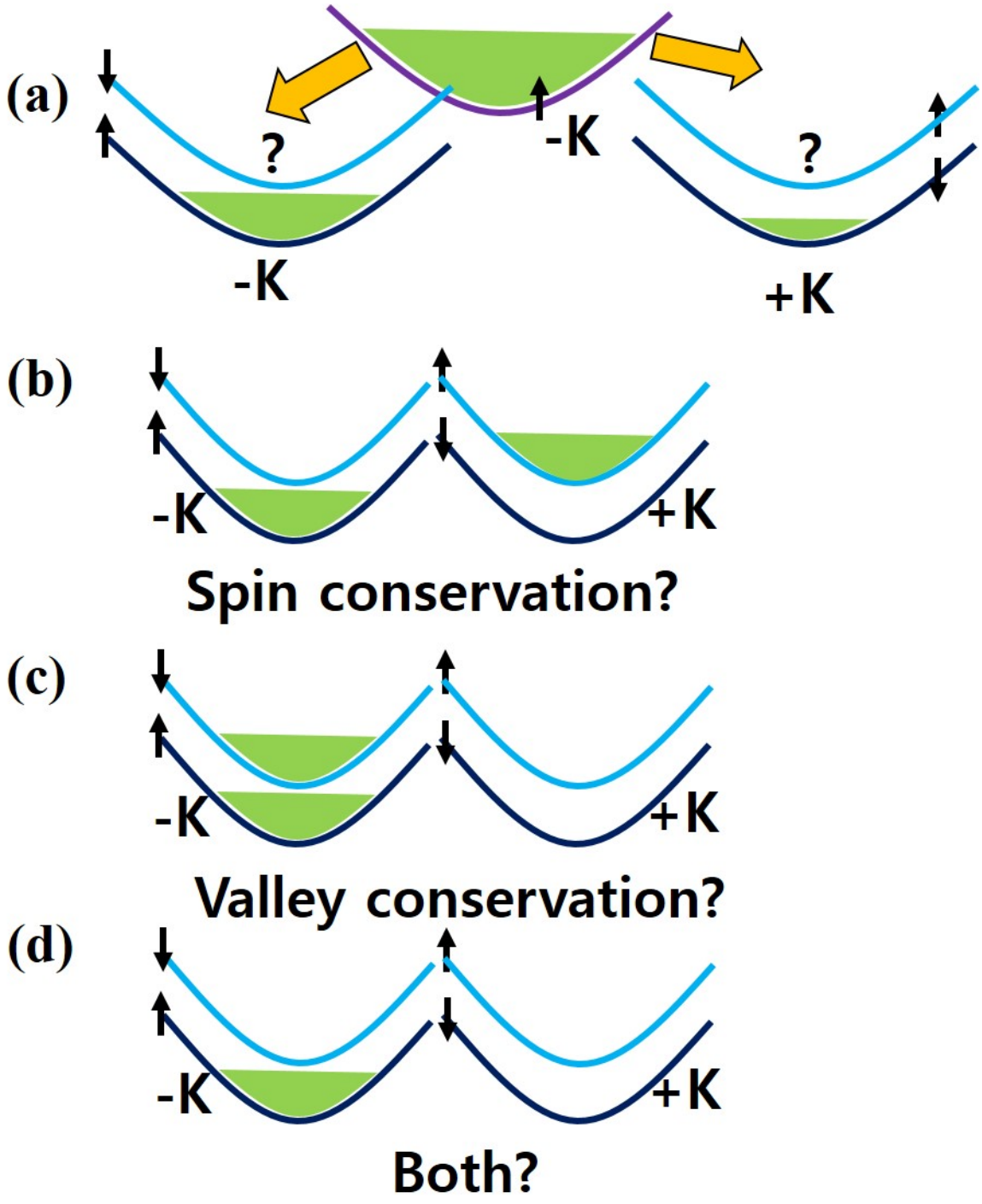

Figure 4.18: *(a) Electron transfer situation in Section 3.4 with $MoSe_2$- WSe_2 in cryo. temp. 30K. The upper band (sky blue colored) could not be used due the energetic preference and The upper band (sky blue colored) is avaliable. Only one valley was used. (b), (c), (d) are the situation of our study with MoS_2- WS_2 in room temp, both bands are avaliable, if the electron strictly follows the spin only, valley only, and spin & valley conservation*

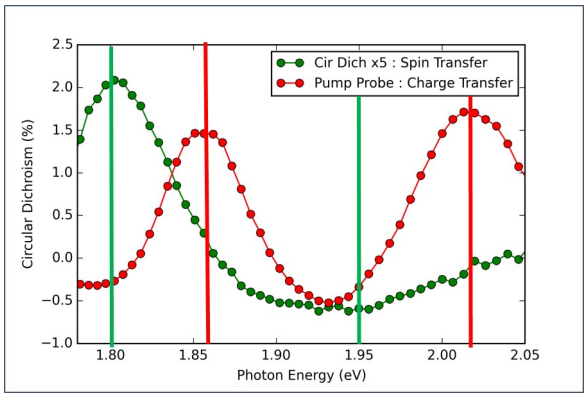

Figure 4.19: *CD signal (green) and Charge transfer pump probe signal (red). Redshift is seen.*

However there is subtle thing to consider the redshift of the CD signal. Fig 4.19 shows the red (left) shifted CD signal (green) compared to the charge transfer pump probe signal (red), about 50meV both for A and B excitonic range. The shifted position and broadened linewidth of the peaks may be considered to be partially originated from SiO_2 layer interference effect and could still be interpreted as A and B exciton range transition when they were analyzed by transfer matrix method. (See Fig 4.20 for the detail)

Nevertheless the full size of redshift and time behavior of the CD signal needs more consideration. Together with the result that the spin valley pump probe signal decays faster than the charge pump probe signal, we attribute this result to the formation of trion (charged exciton) as we previously discussed in the Section 3.2 and 3.4. With the addition of electron from WSe_2 to MoS_2, we hypothesize that both Charged exciton and Neutral exciton is formed. Neutral exciton losses its valley polarization within 1ps timescale via exchange interaction, but stays longer enough ($\sim$100ps) to retain the charge pump probe signal. Charged exciton holds its valley

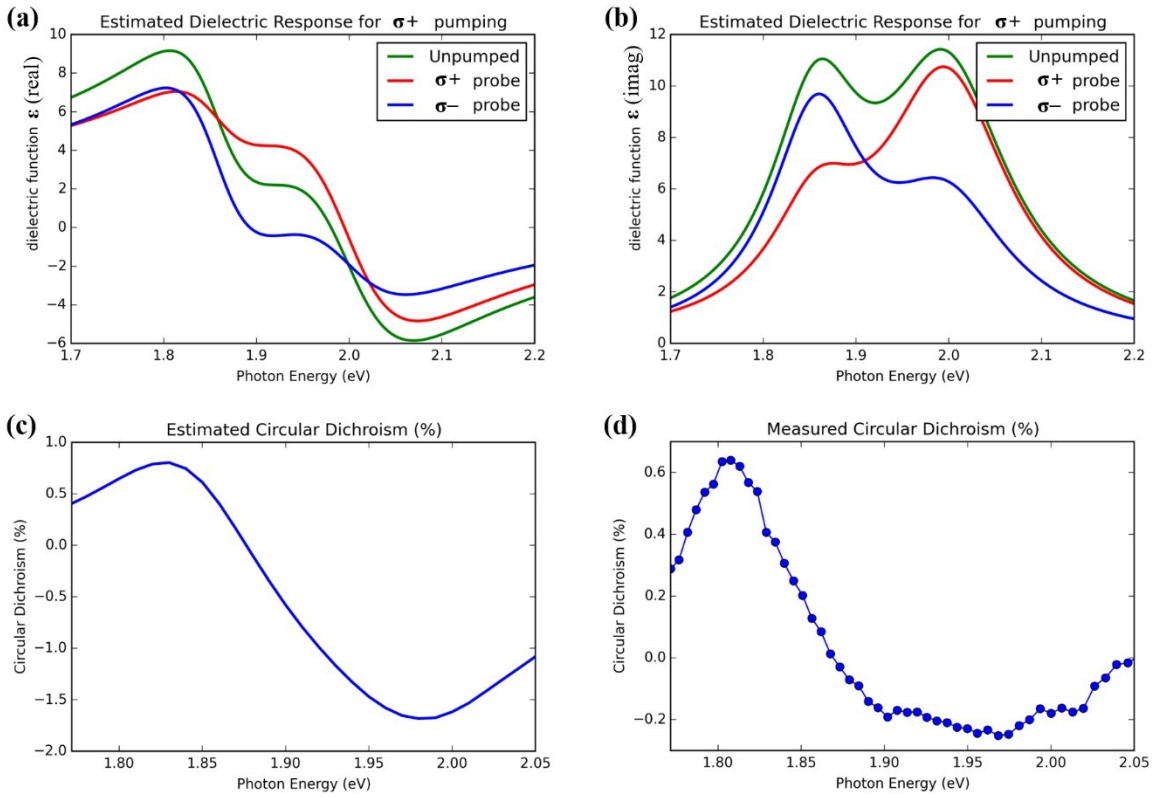

Figure 4.20: *Circular Dichroism modeling of MoS_2 - WSe_2 Heterostructure sample. (a)(b) Complex dielectric function modeling of MoS_2 in heterosturure with (a) real part (b) imaginary part, for the unpumped sample and after left circularly polarized pumped sample. The pumped samples dielectric function takes two different values (transient birefringence), so that there are separated graphs for right circularly polarized probe, and left circularly polarized probe. The pumped functions were made by decreasing oscillator strength $f_{A,MoS_2,\sigma+}$ and $f_{B,MoS_2,\sigma-}$ into a half, while keeping$f_{B,MoS_2,\sigma+}$and$f_{A,MoS_2,\sigma-}$unchanged. (c) Simulation of the estimated circular dichroism using the birefringence dielectric functions in (a)-(b). (d) Experimentally measured value of transient circular dichroism in maximally excited time for the heterosturcture, showing same overall shape as in (c).*

polarization for few ps to 10ps timescale, but decays fas enough ($\sim$10ps) to show the fast decaying spin valley pump probe signal. This intermediate, hypothetical model might be able to become more profound after some supporting experiment, which suggested a goal for the future research project.

Chapter 5

Electrical control of spin and valley Hall effect in monolayer WSe_2 transistors near room temperature

After the optical investigation of spin valley dynamics in TMDC Heterostructure, we now turn to the electrical way to control the spin valley properties of the TMDC monolayer. Which is essential in the real world application of spintronics. Due to the monolayer geometry and strong spin-orbit coupling, they are predicted to have a coupled spin and valley Hall effect (SVHE) related to the valence band spin splitting[28][29]. This spin splitting is particularly large in tungsten diselenide (WSe_2). Here, we investigate the SVHE in p-type monolayer WSe_2 transistors. Using magneto-optical Kerr effect (MOKE), we observe distinct spin-valley polarization along the sides of the transistor channel at a near-room temperature of 240 K. We show we can control the polarization magnitude using electric field, in agreement with a drift diffusion

transport model. Our study complements earlier reports of electrical control of the valley Hall effect (VHE) in gated n-type MoS_2 at 30 K[18] by showing that the SVHE can be observed and controlled at near-room temperature. Our results demonstrate the robustness of the SVHE and its potential for spin-based device applications.

The original suggestion of this study, sample and device preparation, and optical measurement, electrical transport experiment was done by Barr, E.(in Heinz, T.'s group in Stanford) and Currivan-Incorvia (in Pop, E.'s group in Stanford) equally. I myself (Kim, Suk Hyun) provided my optical measurement idea and skill, and have done the optical experiment together with them, and have done the computer programming, mechanical setting (fine XY stage control) for the main measurement of this study. McClellan, C., and Wong, H-S. P. helped with the electrical measurements and some of the analysis of the IV measurements.

5.1 Introduction

The lack of lattice symmetry in monolayer TMDs combined with strong spin-orbit coupling leads to non-zero Berry curvature and large spin splitting, Δ_{SOC} , in the valence band. The splitting and Berry phase become non-trivial at the K and K points.

Figure 5.1 shows a schematic monolayer WSe_2 band diagram. Due to time-reversal symmetry, the Berry curvature and spin of carriers in the valence band around the K and K points are opposite and equal[30][31]. Thus, this material has a coupled SVHE which could lead to device applications. Control of the SVHE in TMDs at room temperature could provide a gateable way to switch nanomagnets for spintronics and

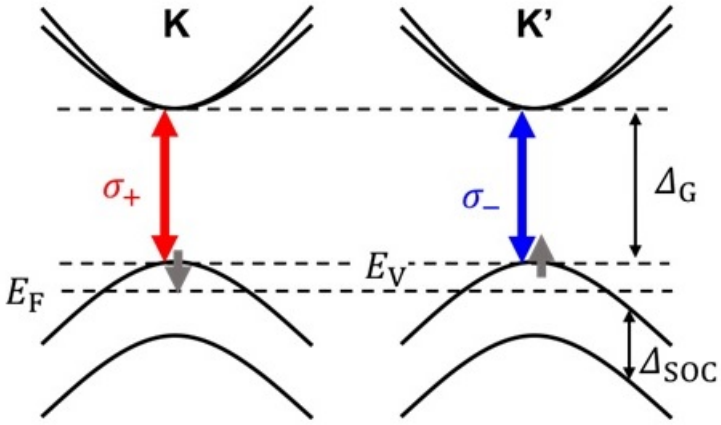

Figure 5.1: *Schematic of the conduction band bottom and valence band top in monolayer WSe_2 at the K and K points, showing spin splitting $\Delta_{SOC} \sim 0.46$ eV and coupling with light polarization $\sigma+$ and $\sigma-$. Δ_G is the bandgap, E_V is top of the valence band energy, and E_F is the Fermi energy.*

memory. Additionally, control of large areas of valley population in combination with valley-light polarization coupling could be used for non-reciprocal photonic devices.

Previous work has demonstrated the VHE in n-type MoS_2 at cooler temperatures (10 K $\sim$ 30 K)[28][18], opening up the field of valleytronics. For practical applications, advancement towards spin and valley electrical control at room temperature is necessary. Δ_{SOC} is significantly larger in Tungsten compounds than Molybdenum, making them promising candidates for spin-based applications[29][32][33][34]. We expect the scattering rate of spin and valley-polarized carriers to be slow, as a carrier cannot both conserve spin and scatter into the other valley. Thus, long-lived spin and valley lifetimes are expected. In chemical vapor deposition-grown monolayer WSe_2, lifetimes have been measured from 0.7 ns to 80 ns at 10 K[12][35]. In exfoliated samples, lifetimes have been measured over 1 μs at 10 K[37][38]. These long lifetimes protecting spin lead to long spin diffusion lengths, allowing us to measure the effect

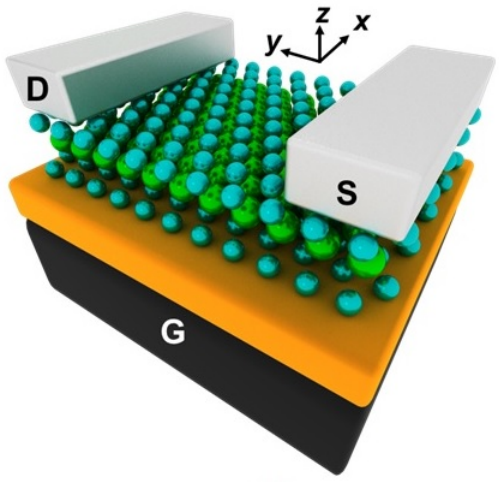

Figure 5.2: *Cartoon of the fabricated monolayer p-type WSe_2 transistors (not to scale). W is shown in green and Se in blue. Pd is used for source (S) and drain (D) contacts. Some samples have hexagonal boron nitride (hBN) underneath the WSe_2, depicted in orange. We use a Si/SiO_2 back-gate (shown in black, G), with oxide thickness of 285 nm or 100 nm*

with a 0.9 μm full-width-half-max (FWHM) laser.

To this end, we have built p-type WSe_2 field-effect transistors (FETs) to measure the spin accumulation and show control of the effect using electric field. Figure 5.2 shows a cartoon of the transistor. We manipulate the transistor with a drain voltage V_D, which creates an in-plane electric field in y across the channel, and a back-gate voltage V_G (with source voltage as reference), which modulates the Fermi level. With both V_D and V_G, a spin and valley Hall current is generated perpendicular to that field in x along the width of the sample without external magnetic fields.

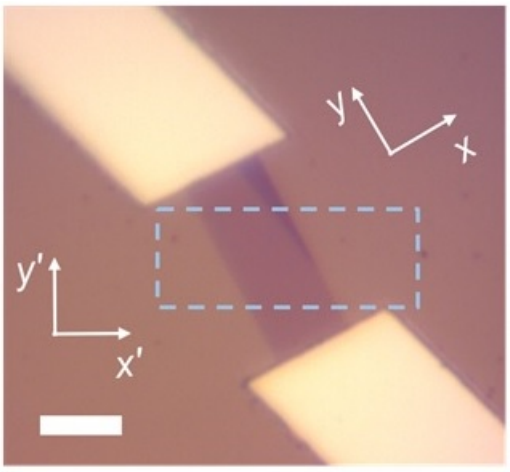

Figure 5.3: *Microscope image of Sample 1, with monolayer WSe_2 in center and 30 nm thick Pd source/drain contacts. The flake is 5 μm × 12 μm. The dotted box is the scan area for Fig. 2. Scale bar: 5 μm.*

5.2 Sample Preparation & Basic Test

5.2.1 Sample Preparation

As shown in Figure 5.2, light of circular polarization $\sigma+$ ($\sigma-$) causes excitations in valley K (K)[39][7]. If the valley populations are different, linearly polarized light will gain a Kerr rotation phase, θ_{Kerr} , which can be measured via MOKE.

Figure 5.3 shows an image of the first sample studied, Sample 1. The SVHE is mapped by rastering the sample in (x,y) underneath the laser. The WSe_2 flake is monolayer with a small piece of bilayer in the top right corner. Sample 1 is on a Si (substrate) / SiO_2 (285 nm) back-gate. We turn it on using DC V_G = -90 V and AC $V_D = 10\ V_P$ (peak voltage). At this V_G, we find symmetric current about $V_D = 0$ V. As the WSe_2 is on thick SiO_2, this sample requires $V_G \leq -20V$ on the back-gate to generate enough carriers to observe both current and the Hall effect (see Fig 5.6 for

I-V characteristics).

Transistor fabrication was carried out as following. Fabrication was done using mechanical exfoliation, electron-beam lithography, and electron-beam evaporation. Nb-doped WSe_2 crystals from 2D semiconductors were exfoliated onto polydimethylsiloxane (PDMS). The dopants assist with p-type transistor behavior. After identifying monolayers using Raman spectroscopy, the flake was transferred onto the Si/SiO_2 substrate by heating at 45 C. This process was repeated twice for samples with hBN.

The flakes were patterned using polymethyl methacrylate (PMMA) electron-beam resist and electron-beam lithography, followed by etching with XFe_2. PMMA was removed with acetone and subsequent PMMA/electron-beam lithography steps were done to place the 30 nm Pd contacts using electron-beam evaporation. Pd is used due to its large work function (∼5 eV), making it a suitable p-type contact, and due to its low evaporation temperature to limit sample damage. After device fabrication, we performed a high vacuum anneal at 2×10^{-7} Torr and 240°C for one hour to remove excess PMMA residue. Sample 1 used p++ type, $< 0.005\Omega$-cm, $< 100 >$ Si with 285 nm of SiO_2, and Sample 2 used n++ type, $< 0.005\Omega$-cm, $< 100 >$ Si with 100 nm of SiO_2.

5.2.2 Basic Optical Test : PL and Raman

The sample is cooled via liquid nitrogen in a cryostat, but thermally isolated such that the temperature, T, of the WSe_2 is around 240 K. The temperature is confirmed using photoluminescence (PL), shown in Figure 5.4. for a sample at room temperature vs. cooled. When cooled, the peak energy blue-shifts by 20 meV, and the peak FWHM shifts from 46 meV to 43 meV. Comparing to previous work[40][41], we find that this

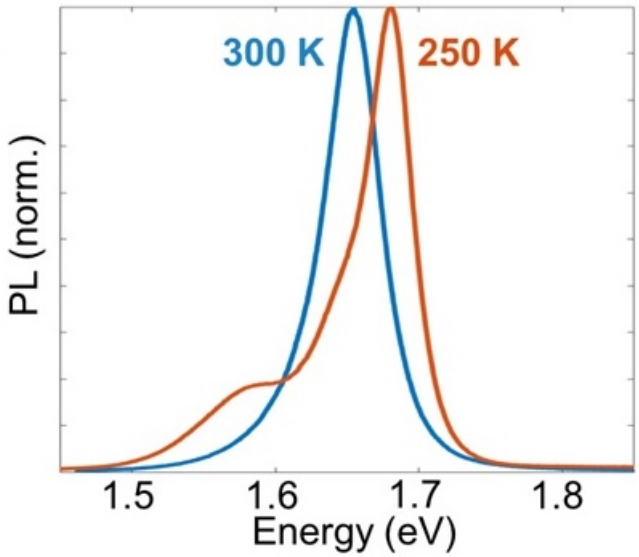

Figure 5.4: *Photoluminescence (PL) comparing ambient conditions vs. cooled in the cryostat (V_G = 0).*

shift corresponds to T $\sim$ 240$\pm$10 K.

Raman spectroscopy has been used to identify monolayers and monolayer quality. Fig. 5.5 shows the Raman spectroscopy for Sample 2 after exfoliation and after fabricating the device. In bilayer or thicker samples, the B^1_{2g} peak should be emergent around 309 cm^{-1} [42], confirming a monolayer is present. No significant changes in Raman were seen from sample processing.

5.2.3 Basic Electrical Test : IV Characteristic

Fig. 5.6 (a) and (b) show the channel current I_D vs. V_G after MOKE measurement of Sample 1 and Sample 2, respectively. While initial IV measurements showed no n-branch turn-on, after operating the device under MOKE measurements some n-type behavior was introduced, particularly in Sample 1. For Sample 1, the back-gate was

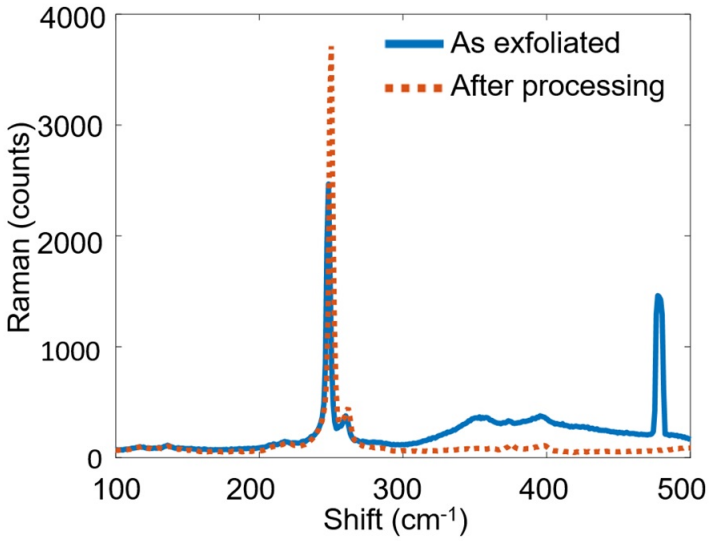

Figure 5.5: *Raman characterization. Taken for Sample 2 as exfoliated on PDMS (blue solid) and after transfer and device fabrication (orange dotted).*

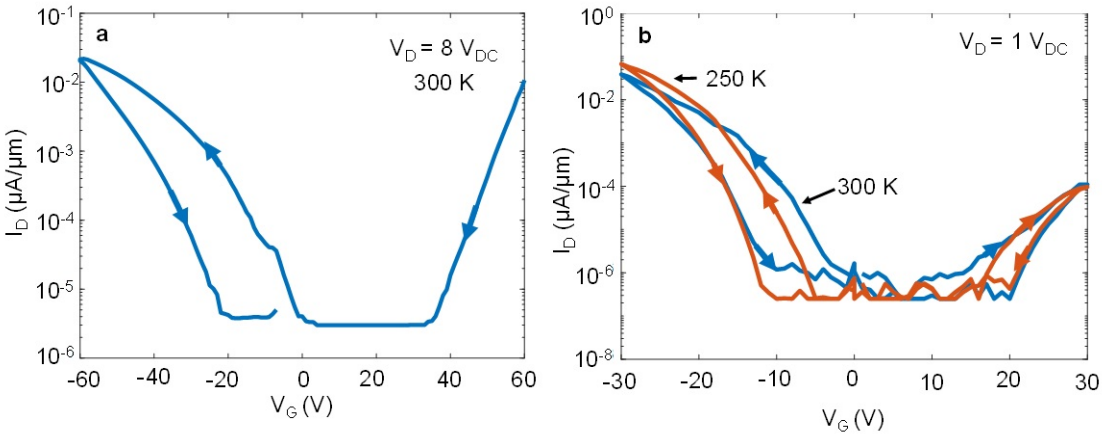

Figure 5.6: I_D *vs.* V_G *characterization taken after MOKE measurements. a, Sample 1 and b, Sample 2 near Kerr mapping conditions.*

pushed to -90 V during operation to observe steady DC current. From the I_D vs V_G curves, we note that we are likely operating the devices just around the turn on point, so our drain current is linear with drain voltage. Sample 1 required a much higher back-gate because of its thicker oxide. From the IV behavior, we estimate the hole density is approximately $(3.3 \pm 0.5) \times 10^{12} cm^{-2}$ for Sample 1 and $(5 \pm 3) \times 10^{11} cm^{-2}$ for Sample 2 at -90 V and -20 V, where the error comes from uncertainty in the threshold voltage.

Room temperature and cold temperature IV measurements were obtained for Sample 2 in Fig. 5.6 (b). At colder temperatures, there is reduced hysteresis and a larger turn-on voltage[34]. Lower temperature reduces the thermionic emission over the barrier, requiring larger V_G to turn on the channel. The higher on current at lower temperatures implies we are in the regime where phonon interactions are decreased, increasing the mobility compared to room temperature.

5.3 Optical mapping of the spin and valley Hall effect

5.3.1 MOKE characterization Method

In the experiments, two lasers have been used: a supercontiuum laser (Fianium White-Lase supercontinuum lasers, NKT Photonics) with wavelength nearly resonant to the A exciton energy of the WSe_2 sample, and a continuous wave 1.84 eV laser. For the near-resonant measurements, the wavelength is selected with a bandpass filter (10 nm FWHM) from the supercontinuum laser. The beam is linearly polarized and focused

on the sample with a 40× objective lens resulting in a beam spot size of 0.7-0.9 μm FWHM. The spot size was found by fitting the image of the beam from the microscope camera with a 2D Gaussian and confirmed by fitting the rising edge of the Kerr rotation to a Gaussian. The Kerr rotation detection was done using the optical bridge technique, which takes the probe beam after it is reflected off the sample and passes it through a Wollaston prism with an axis 45 to the polarization axis to split the beam into two with equal intensities and perpendicular polarization to each other. The two beams are monitored by two photodiodes, and the signal difference is extracted and amplified by a low-noise amplifier. The signal difference is proportional to the Kerr rotation. The signals are finally sent into a lock-in amplifier, which is synced to the source-drain AC voltage at 700 Hz. 700 Hz provides cycles long enough that the carriers behave as one might expect in DC operation, but short enough that shorter integration times are adequate for lock-in measurements.

5.3.2 Result

Figure 5.7 shows the resulting MOKE map of the SVHE in Sample 1, imaged with 1.85 eV. Figure 5.8 shows the x-axis slice graph of MOKE data. We see negligible θ_{Kerr} on the substrate and two distinct bands of positive (red) and negative (blue) θ_{Kerr} on the WSe_2 flake, corresponding to light interactions with the two valleys. Thus, we observe spin and valley accumulation to the sample edges at 240 K. Figure 5.9 (a), (b) are some additional 2D MOKE map as back-up data.

Preliminary results also show the SVHE at 294 K, room temperature. Kerr rotation indicative of SVHE across Sample 2 was also observed at 294 K, shown in Fig. 5.10. We see positive and negative θ_{Kerr} split across the sample (red squares)

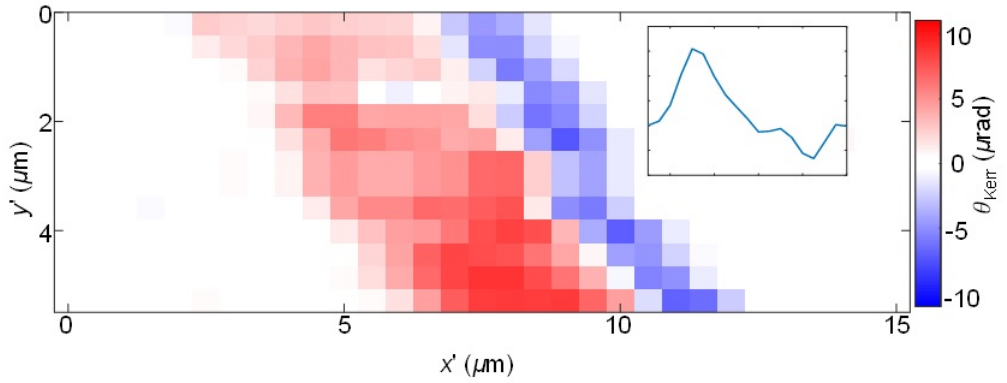

Figure 5.7: *Mapping of the SVHE. MOKE maps of Sample 1 taken at T = 240 K with 0.5 μm steps using a 1.85 eV laser. Insets show an example line scan of θ_{Kerr} vs. x on an area with no bilayer and optimized measuring parameters with a smaller in-plane bias (2 V tight focus and low noise).*

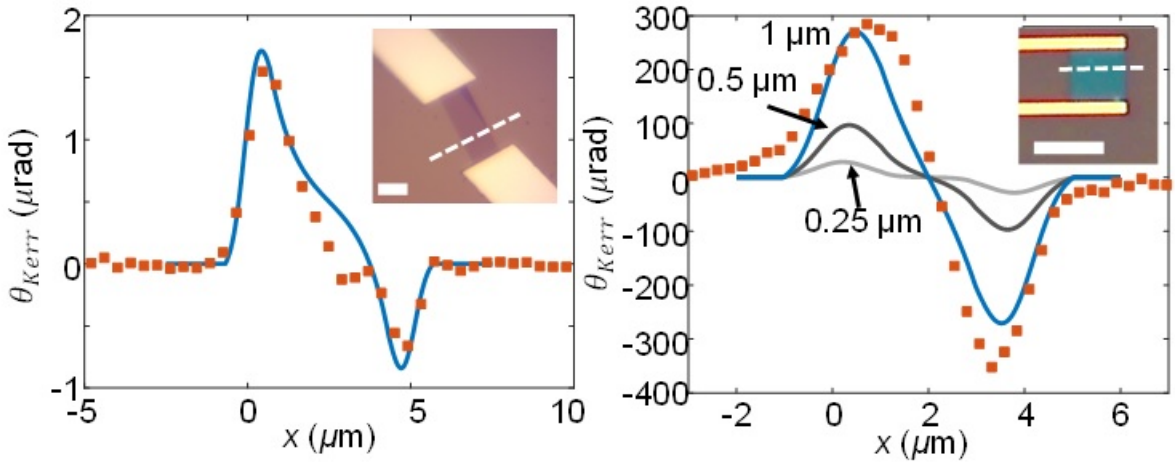

Figure 5.8: *Drift diffusion model comparison. (a) Line scan of θ_{Kerr} vs. position across Sample 1 (red squares, plot direction shown by dotted line on inset image, scale bar 5 μm) for laser energy of 1.85 ± 0.01 eV at V_G,DC = -90 V, V_D,AC = 2 V_P, and T = 240 K.*

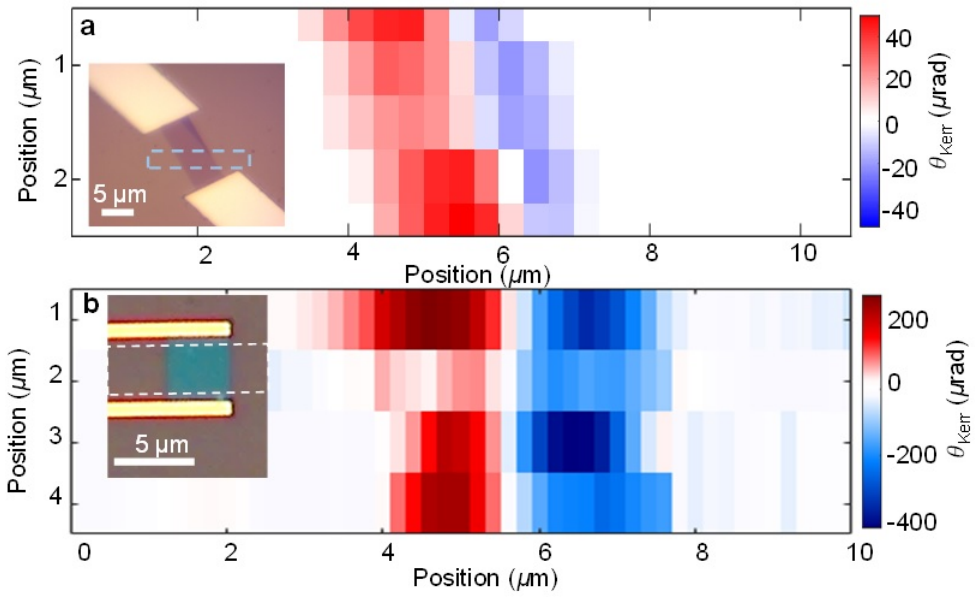

Figure 5.9: *Additional MOKE maps. a, Sample 1 taken at $T = 240$ K using a 1.65 eV laser with 0.5 µm steps. The inset shows the microscope image of Sample 1. b, Sample 2 taken at $T = 240$ K using a 1.65 eV laser with 0.2 µm steps in x and 1 µm steps in y. Inset shows the microscope image of Sample 2, that differs from Sample 1 by having a thinner 100 nm back-gate oxide and 3.3 nm of hBN underneath.*

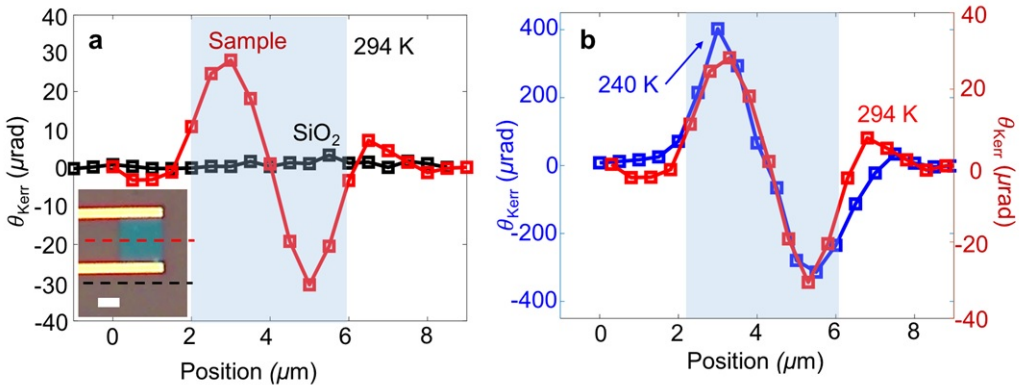

Figure 5.10: *Temperature dependence. a, Line scans of θ_{Kerr}. position at 294 K, across Sample 2 (red) vs. across the SiO_2 substrate (black). The data is taken with V_G = -10 V, V_D,AC = 1 V_P, 2.6×10-5 Torr, and laser energy 1.70 eV, and is averaged over multiple scans. The light blue box shows size of sample in x. Locations of the scans are depicted in the inset, scale bar 2 μm. b, Comparison of line scans at 294 K (red) with 240 K (blue) under similar conditions except different pressures of 2.6×10-5 Torr and 6×10-7 Torr, respectively.*

compared to across the SiO_2 surface (black diamonds), showing a SVHE at room temperature. This behavior is repeatable for the sample with hBN underneath if measurements are taken shortly after fabrication or after performing a high vacuum anneal. This is evidence that reducing interactions between the channel and its environment helps push the effect towards room temperature.

Figure 5.10 (b) compares line scans at 294 K and 240 K. Under similar operation conditions (1.70 eV), $\theta_{Kerr,max}$ is larger at lower T. Increased θ_{Kerr} can be attributed to multiple temperature-dependent factors. The exciton energy blueshifts towards 1.70 eV at 240 K, which increases overall θ_{Kerr} . this shift is observed in the PL. At colder temperatures and resulting lower pressure, there is reduced charge depletion and improved mobility seen in the IV curvesPodzorov 2004, which implies larger intervalley carrier population difference. The peaks are asymmetric with a thinner

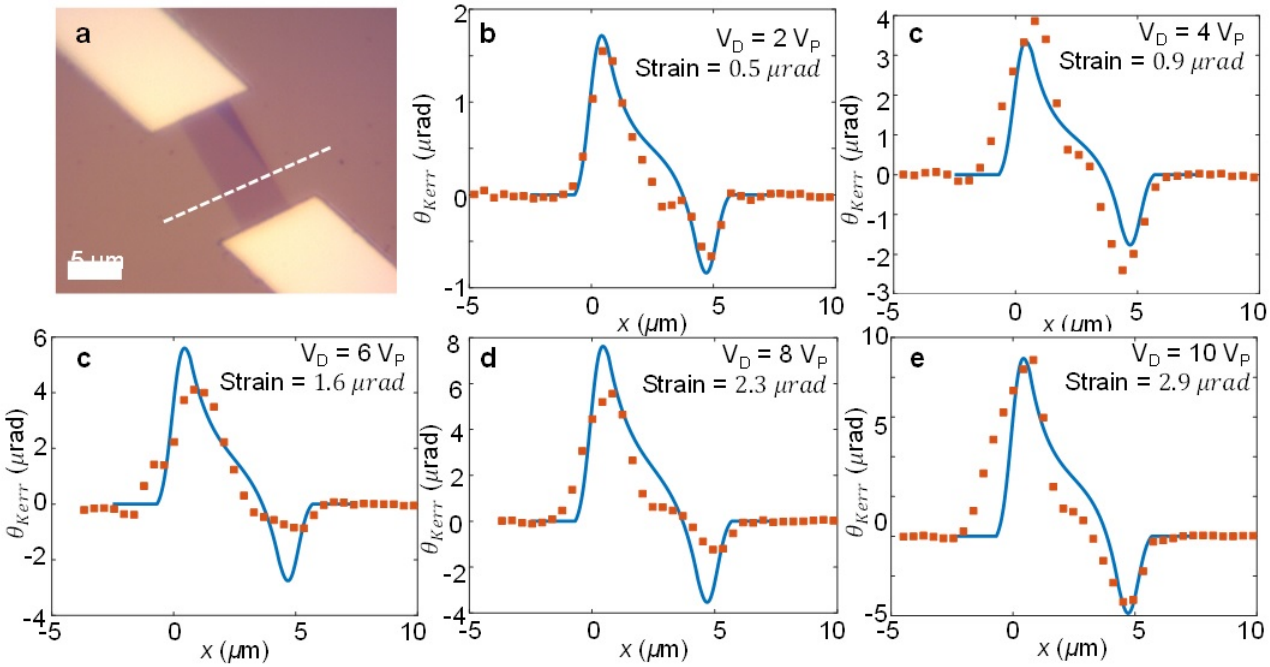

Figure 5.11: *Fitted MOKE linescans. (a) The sample and approximate position scanned and fitted Kerr Rotation measurements for 2 V_P to 10 V_P. (b)(e) using current estimated from IV characteristics (assume turn on of -45 V and linear drain voltage relation), L_D=0.8 μm and $D = 4.1 \times 10^{-5} m^2/s$ and a constant background over sample empirically estimated.*

and smaller peak on the side of the sample with a region of bilayer, as shown in the example linescan inset. The maximum Kerr rotation measured is — $\theta_{Kerr,max}$ — = 9.1 μrad; subtracting a background Kerr signal estimated from the difference in positive and negative peaks, the maximum Kerr rotation is about 8.2 μrad.

Figure 5.11 (a) shows an additional sample map for Sample 1 using a closer-to-resonance, 1.70 eV, laser energy, resulting in similar spin and valley accumulation to the map shown in the main text.. We are using V_G = -90 V and AC V_D = 10 V_P (peak voltage). Figure 5.11 (b) shows a MOKE map of Sample 2. Smaller voltages

are used due to the thinner SiO_2 and shorter transistor, with V_G,DC = -20 V and V_D,AC = 1 V_P. We corrected these scans with an angle in the piezo to scan along the width, however this introduced some noise which we corrected with y-averaging. In Sample 2, the map also shows clear positive (red) and negative (blue) $\theta_{Kerr,max}$ across the sample, showing the spin and valley Hall accumulation to the edges in x. With the 0.2 μm x step size, we can see the zero-point where the θ_{Kerr} changes from positive to negative. This sample has more spatially symmetric positive and negative bands compared to Sample 1. We observe a maximum Kerr rotation — $\theta_{Kerr,max}$ — = 9.1 μrad, 8.7× higher than in Sample 1 (49 μrad). This can mostly be attributed to the thinner SiO_2, which produces a 7.5 times stronger signal due to interference effects. The hBN also protects the WSe_2 from current-depletion due to interfacial traps, although the sample can still be affected by mobile and trapped charges.

5.3.3 Kerr rotation dependence on both sample interference effects and laser wavelength, and Kerr rotation conversion to valley concentration

In this section, we estimate the population difference between spin up ($p^{\uparrow}$) and spin down ($p^{\downarrow}$) carriers from the measured θ_{Kerr} .

We use the reflection contrast of the sample and modeling the dielectric function using a transfer matrix model as well. we explain the difference between the magnitude of the Kerr rotation measured in Sample 2 on 100 nm SiO_2 and Sample 1 on 285 nm SiO_2. We also quantify the relationship between the measured Kerr rotation and the intervalley concentration difference.

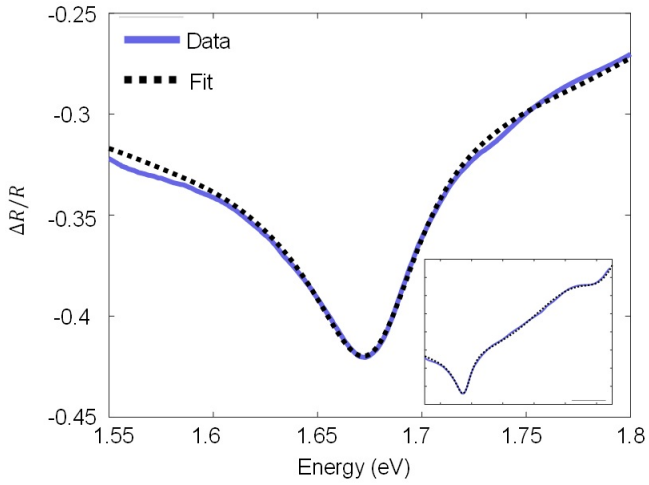

Figure 5.12: *Reflection Contrast. Taken for Sample 2 and fit via transfer matrix using a sum of Lorentzians to represent the dielectric function of the WSe_2. The inset shows the full fit plotted from 1.55 eV to 2.15 eV on the x axis and -.45 to -0.05 on the y axis.*

Shown in Fig. 5.12, the reflection contrast of Sample 2 was taken at 240 K in vacuum in order to estimate the oscillator resonance, strength, and damping of A excitons. The reflection contrast is taken as the difference between the reflection off the WSe_2 on hBN, R_{WSe_2}, and the SiO_2, R_{SiO_2}, normalized by the reflection off SiO_2:

$$\frac{\Delta R}{R} = \frac{R_{WSe_2} - R_{SiO_2}}{R_{SiO_2}} \tag{5.1}$$

Following previous work[34], we model the WSe_2 dielectric function as a series of Lorentzians with a constant real background. For our purpose, we included 3 Lorentzians corresponding to the A, B, and C exciton. To relate the reflection contrast to the dielectric function, we used the dielectric function as an input in a transfer matrix model of the Si/100 nm SiO_2/3 nm hBN/WSe_2 stack and fit the results. The

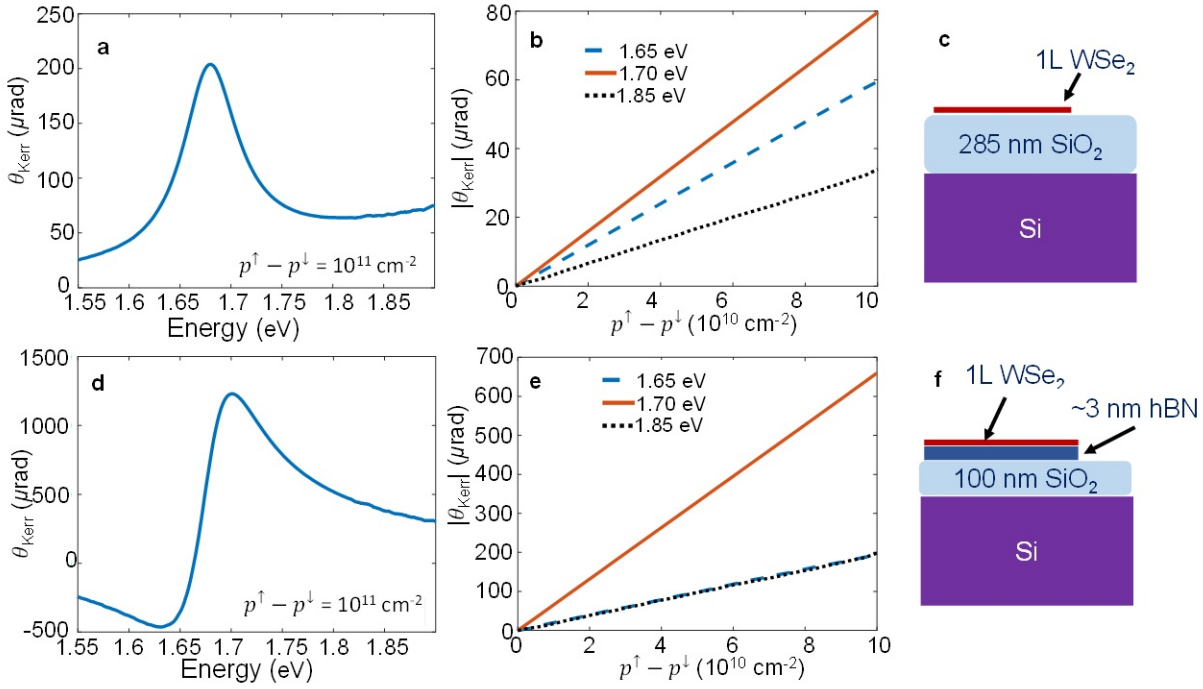

Figure 5.13: *Intervalley carrier concentration to Kerr rotation conversion. The Kerr rotation (given $p_0 = 10^{12} cm^{-2}$) as obtained from a transfer matrix model (a),(d) plotted for different probing laser energies and (b),(e) plotted over intervalley concentration difference for three particular laser energies for the represented stacks. (c),(f) Cartoon of the Si/285 nm SiO_2/WSe_2 stack representing Sample 1 and Si/100 nm SiO_2/hBN/WSe_2 stack representing Sample 2.*

A exciton peak had a resonant energy of 1.679 eV, strength of 0.67 eV2, and damping of 64 meV.

Using the dielectric function fit obtained at 240 K and 0 V back-gate, we assume the change in the carrier concentration in the K valley is linearly related to the A exciton oscillator strength of right hand (RH) circularly polarized light (and K with left hand, LH, circularly polarized light). Chernikov et al. 2015[36] found that for WS_2 the oscillator strength decreased to about 0.2% of its charge neutral point at a

carrier density of about $8\times10^{12}cm^{-2}$ Extrapolating to WSe_2, we estimate an oscillator strength decrease of about 0.1% per $1\times10^{1}cm^{-2}$ away from charge neutrality for each valley. We are ignoring the Burnstein-Moss effects which may shift the peak and the potential emergence of a intervalley trion peak, both of which have been observed in highly polarized hole-doped WSe_2[37]. These effects can be ignored as the intervalley carrier concentration is relatively small.

A transfer matrix model is used to estimate the response, assuming a carrier concentration of $p_0 = p^{\uparrow} + p^{\downarrow} = 10^{12}cm^{-2}$. The Kerr rotation for a give intervalley concentration changed less than 0.5% between $p_0 = 10^{11}cm^{-2}$ and $p_0 = 10^{12}cm^{-2}$.

The reflection of RH and LH light is assumed to be the response of each valley with concentrations deviating from p_0 by $\pm\frac{p^{\uparrow}-p^{\downarrow}}{2}$, i.e. with increased and decreased oscillator strengths in their respective dielectric responses. Using this assumption and examining the wavelengths used in the experiments: 672 nm (1.85 eV), 730 nm (1.70 eV) and 750 nm (1.65 eV), in Fig. 5.13. we plot the Kerr rotation θ_{Kerr} vs. population difference between up and down carriers and vs. probing energies.

Fig. 5.13. (a)(b)(c) is for a Si/285 nm SiO_2/WSe_2 stack to represent Sample 1 and Fig. 4d-f is for a Si/100 nm SiO_2/3.1 nm hBN/WSe_2 stack to represent Sample 2. The Kerr rotation is calculated as $\theta_{\sigma+}-\theta_{\sigma-}$, where $r_{\sigma\pm}$ is the complex reflectivity for $\sigma\pm$ polarized light and $\theta_{\sigma\pm}$ is the associated phase. From the simulations, one can see that the Kerr rotation for the thinner oxide will appear almost 7 times larger than for the thicker oxide for the same intervalley carrier concentration difference due to interference. This partially explains the large magnitude difference between θ_{Kerr} measurements of Sample 1 and Sample 2.

The adjusted peak accumulation in Fig. 5.7 corresponds to $p^{\uparrow}-p^{\downarrow} \sim 2.4 \times$

$10^{10}cm^{-2}$ or $\sim 0.72\%$ polarization, where polarization is defined as $\frac{p^{\uparrow}-p^{\downarrow}}{p^{\uparrow}+p^{\downarrow}}$. We deduce the hole concentration at the given back-gate, $p = p^{\uparrow}+p^{\downarrow}$, from the electrical characteristics (Fig 5.6). For the same sample, we obtained maps using a closer-to-resonance energy of 1.70 eV, which measured $|\theta_{Kerr,maxadj}| \sim 33$ μrad(Fig 5.11). This corresponds to $p^{\uparrow}-p^{\downarrow} \sim 4.1 \times 10^{10}cm^{-2}$. Both laser energies measure similar maximum population difference, but probing closer to the A excitonic peak (1.67 eV) increases the measured θ_{Kerr}. This is the expected behavior if the valley concentration is modifying the resonant peak of the A exciton.

5.3.4 Parameter estimation with Spin-Diffusion model

In a spin drift diffusion model, assuming uniformity, the resulting spin accumulation can be described as :

$$s(x) = p^{\uparrow}-p^{\downarrow} = \frac{L_D}{D}\frac{\sigma_S}{\sigma_C}J_C\frac{e^{\frac{x}{L_D}}-e^{\frac{L-x}{L_D}}}{1+e^{\frac{x}{L_D}}} \tag{5.2}$$

where σ_S is the spin conductivity, σ_C is the charge conductivity (estimated by $\mu p_0 e$) and L is the length of the sample.

The accumulation near the edges falls off proportional to the diffusion constant $L_D = \sqrt{D\tau_s}$ where D is the spin diffusivity estimated by the Einstein relationship and τ_s is valley and spin polarized hole lifetime. The spin Hall conductivity can be due to both extrinsic and intrinsic sources. However, for the purposes of our calculations, the spin Hall conductivity is approximated from the theoretical low temperature, intrinsic spin Hall conduction given an approximate carrier concentration [29]. This spin hall conductivity is incorporated in a drift diffusion model incorporating spin

(using $s = p^{\uparrow} - p^{\downarrow}$ for shorthand).

In this model, the 1D continuity equation in steady state (with no magnetic field) is $(\partial s/\partial t) = -(\partial/\partial x)J_{s,x} - (s/\tau_s) = 0$and the spin current is $J_{s,x} = -D(\partial/\partial x)s + \sigma_S E_y$. D is the carrier diffusivity, σ_S is the spin-hall conductivity, and E_y is the electric field. The lifetime, τ_s, is dominated by the lifetime of a valley polarized hole, and only holes are considered. This model has been used to describe spin Hall effect in GaAs[43]. An analysis of these equations at steady state in one dimension, with reflecting boundary conditions $\hat{x} \cdot J_{s,x}(x = 0, L) = 0$, leads to

$$s(x) = \frac{L_D}{D}\sigma_S E_y \frac{e^{\frac{x}{L_D}} - e^{\frac{L-x}{L_D}}}{1 + e^{\frac{x}{L_D}}} \tag{5.3}$$

Where the diffusion constant is $L_D = \sqrt{D\tau_s}$. Hence, the peak accumulation, assuming $L \gg L_D$, would be approximately $|\frac{L_D}{D}\sigma_S E_y| = |\frac{L_D}{D}\frac{\sigma_S}{\sigma_C}|$ in an idealized scenario. To compare to our experimental data, we obtain a carrier concentration based on the capacitance plus offset mode of $1.1 \times 10^{11} cm^{-2}$ for V_G = -60 V, from which we can find the intrinsic spin hall conductivity and the charge conductivity assuming the mobility to be μ =20 cm^2 /Vs. We assume the diffusivity is related by the Einstein model. Taking our experimental values $L \sim 0.5\mu m$ and $J_C \sim 1 \times 10^{-2}\mu A/\mu m$, we find $s = p^{\uparrow} - p^{\downarrow} = 7 \times 10^9 cm^{-2}$.

In measurements, we found a maximum Kerr Rotation under a back-gate of V_G = -60 V and $V_D = 10\ V_P$ ($\sim$7.1 V_{RMS}) to be approximately 0.9 rad; including a strain related offset, this reduces to 0.5 rad (computed from the difference between the two maxima). Converted to an approximate spin accumulation of $p^{\uparrow} - p^{\downarrow} \sim 1.4 \times 10^9 cm^{-2}$ approach the predicted accumulation. The shortfall can be explained by Gaussian convolution, the slight difference in applied drain voltage and reduced current from

hysteresis. To better compare, we plotted the Kerr rotation data alongside predictions from the spin drift diffusion model empirically setting a strain related background Kerr signal over the entire sample. In the maintext, we included the data/model comparison for V_G = -90 V and $V_D = 2\ V_P$. In Supplementary Figure 5, we show the fit for 5 applied draini voltages. We assume a linear voltage increase from -60 V to -90 V and linear drain voltage dependence and use μ=20 cm^2 /Vs , where D is the spin diffusivity estimated by the Einstein relationship and L_D=0.8 μm.

The drift-diffusion model has been used to estimate the behavior of spin accumulation in GaAs[43]. In Figure 3a, we compare a line scan across Sample 1 (as shown by the inset) to a drift diffusion model including laser beam Gaussian spreading and an overall strain background contributing 0.9 μrad. For these measurements, we set V_G = -90 V and $V_D = 2\ V_P$, finding —$\theta_{Kerr,max}$— = 1.5 μrad with a 1.86 eV laser, corresponding to — $p^{\uparrow}-p^{\downarrow}$— 5×$10^9 cm^{-2}$, or 0.15% polarization. As there is some uncertainty in the spin hall conductivity (one could include extrinsic contributions) and in current, mobility and lifetime, the values used in this model simply indicate that our data can be fitted with reasonable order-of-magnitude parameters. Included in Fig 5.10, we fit using the same parameters for different V_D.

In Figure 5.10 (b), we compare the shape of our experimental data to the drift diffusion model for a second sample, Sample 2 (x position corrected for scanning drift). Sample 2 is a solely monolayer, 4 μm × 4 μm flake on Si (substrate) / SiO_2 (100 nm) / hBN (3.3 nm), shown in Fig. 3b(inset). It is turned on with V_G = -20 V and $V_D = 1\ V_P$. The spin and valley diffusion is observed to be more symmetric in both magnitude and position, in agreement with the drift diffusion model using no extra strain effects.

Scans of Sample 2 indicate diffusion lengths that are long compared to half the width of the sample. However, Sample 2 presented more measurement difficulties as cooling and warming appeared to induce some uneven strain as revealed by Kerr measurements. This introduced some uncertainty in fitting for Sample 2. In both samples, the fitted model shows the monolayer $L_D \geq 0.5$ μm. In Fig. 5.8 (b), we compare our data to the model using $L_D = 0.25$, 0.5, and 1 μm. If the diffusion length was much shorter than the sample width, maximum valley accumulation should be limited to the edges (shown for L_D= 0.25 μm). However, with longer L_D and Gaussian averaging from a laser profile, the maximum is found inward from the edge, matching more closely with the data from both samples (shown for L_D= 0.5, 1 μm). This is repeatedly observed in the experiments: thus, we expect that L_D is a significant portion of the sample width.

5.3.5 Electric field control

MOKE line scans were taken at multiple back-gate and drain voltages to determine the electric field dependence of the SVHE. Figure 5.14 (a) shows $\theta_{Kerr,max}$ vs V_G for Sample 1. We observe an exponential dependence on negative V_G, which implies the spin Hall conductivity has an exponential trend. Negligible θ_{Kerr} is observed for positive V_G (not shown). This agrees with the exponential behavior of the source-drain current I_D vs. V_G shown in Fig. 5.14 (b) (noting the hysteresisin the source-drain and photodoping may alter the operating currents: Supplementary S1).

Figure 5.14 (c) shows line scans of Sample 1 vs. V_D. The general shape of the line scan is maintained, but $\theta_{Kerr,max}$ linearly increases with V_D, shown in Fig. 5.14 (c). The linear dependence on channel longitudinal field agrees with the drift

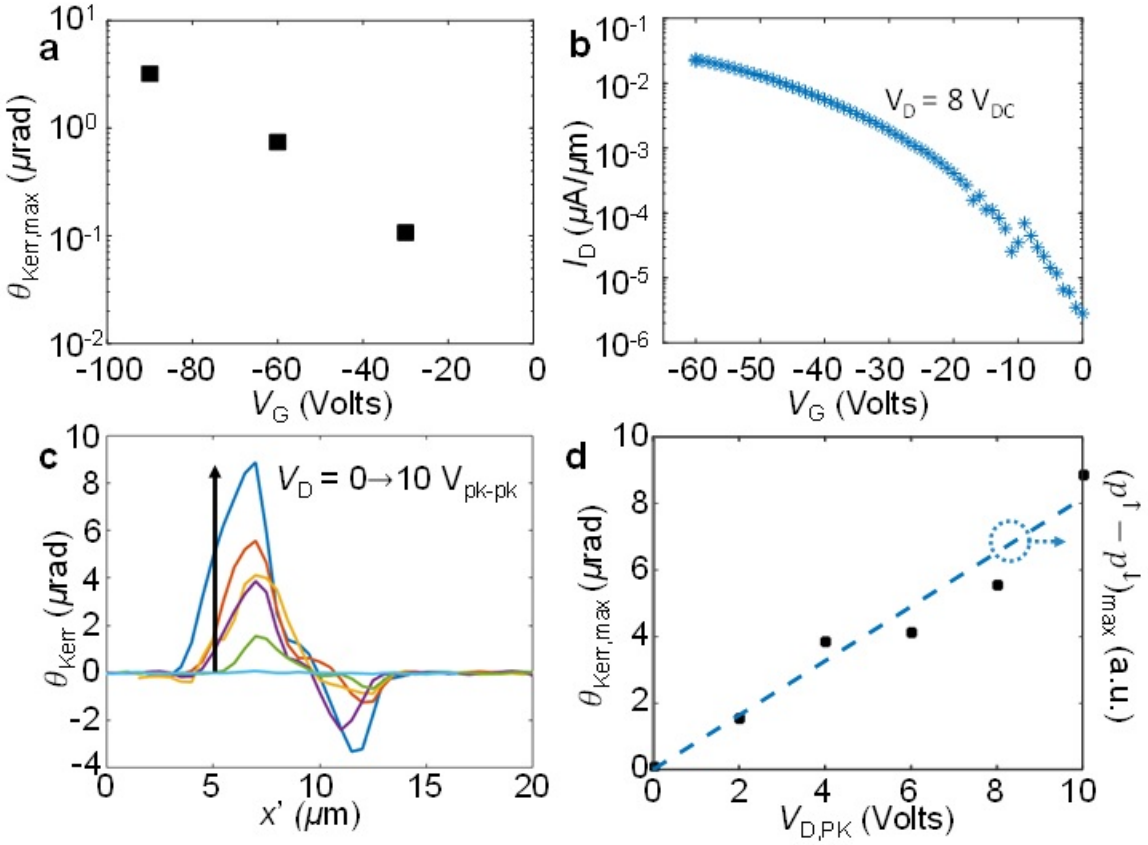

Figure 5.14: *Electric field control. (a) Plot of maximum θ_{Kerr} vs. V_G with $V_{D,AC}$ = 10 V_P or 7.1 V_{RMS}. Measurements were taken off resonance (1.84 eV) using 0.5 µm steps at $3.3 \times 10^{-6} Torr$. (b) Plot of drain current ID vs. V_G with $V_{D,DC}$ = 8 V. (c) Line scans of θ_{Kerr} vs. position across Sample 1 with V_G = -90 V and increasing V_D from 0 to 10 V_P in steps of 2 V_P . (d) Plot of maximum θ_{Kerr} vs. V_D (black squares). The dotted blue line shows the valley population difference vs. position derived from the drift diffusion model.*

diffusion model, plotted as the blue line. Both V_G and V_D-dependent results indicate that the $\theta_{Kerr,max} \propto p^{\uparrow} - p^{\downarrow} \propto I_D$.

Chapter 6

Conclusion

6.1 Charge and Spin-Valley Transfer in Transition Metal Dichalcogenides Heterostructure

In conclusion, we demonstrated that interlayer charge transfer in MoS_2- WSe_2 heterostructure TMDC sample can be observed at room temperature. Transient reflection spectroscopy offers direct probe of the charge transfer from WSe_2 layer to MoS_2 layer, showing increased reflection in both A and B excitonic region of MoS_2 which are not seen at either of separated monolayer MoS_2 and WSe_2 alone. We further made use of circular dichroic spectroscopy to see if spin/valley indexes of the electrons are still conserved during the transfer. We concluded that valley conservation cannot be observed due high momentum interference from room temperature phonon, but we succeeded observe based on valley selective optical effect that the spin orientation is well conserved within the lifetime ∼10ps so that we see prominent circular dichroism signal in both A and B excitonic regions, with opposite signs due to spin

discriminative Pauli blocking effect. In this study we have seen spin conserving interlayer charge transfer in TMDC heterostructure which creates valley selective effect even in room temperature. This shows that TMDC heterostructure spin/valleytronic schemes could be integrated into conventional electronics.

As a future plan, we should look for the condition to adjust the 'ratio' between the spin and valley polarization transfer. For example, under ultralow temperature, one can expect the valley index of electron is not scattered to two valleys but they are conserved and transfer to only one valley because of the suppressed phonon midiated scattering. To erase the spin effect, in-plane magnetic field might be used to scatter the spin while conserving the valley, expected to produce the same circular dichroism signs for the A and B excitonic range, contrast to our original no magnetic room templerature experiment giving opposite signs. We can also electrically gate the heterostructure sample to see the neutral exciton, trion effect of the circular dichroism.

6.2 Electrical control of spin and valley Hall effect in monolayer WSe_2 transistors near room temperature

In conclusion, we have mapped the SVHE in WSe_2 monolayer transistors using MOKE. The maps show accumulation of opposite valleys to the edges of the monolayer at an elevated temperature of 240 K. The shape of the accumulation agrees with a drift diffusion transport model with spin diffusion lengths greater than 0.5 μm. Although there appears to be some potential contributions from strain effects,

the negative and positive accumulation due to the SVHE appears in multiple samples and it is unlikely strain is the dominant effect, considering the accumulation shape is consistent with the spin drift diffusion model. We show electric field control of the maximum spin and valley diffusion in agreement with the diffusion model. Showing control of the SVHE, long spin diffusion lengths, and pushing the effect towards warmer temperatures are very important results for spin-based, practical applications of TMDs.

As a future plan, we should study wider WSe_2 sample for the true spin decay time. Our narrow sample width might be a limitation to measure the spin-valley diffusion length (Kerr Rotation signal decay length) to get the true spin-valley diffusion time. We can also design the Heterostructure experiment of the Spin Valley Hall effect, combining our two main projects.

Bibliography

[1] D. P. DiVincenzo and E. J. Mele, Self-consistent effective-mass theory for intralayer screening in graphite intercalation compounds, Phys. Rev. B 29, 1685 Published 15 February 1984

[2] Photo: Alexander Alus, licensed by Creative Commons Attribution-Share Alike 3.0.

[3] K. S. Novoselov, A. K. Geim, S. V. Morozov, D. Jiang, Y. Zhang, S. V. Dubonos, I. V. Grigorieva, A. A. Firsov, "Electric Field Effect in Atomically Thin Carbon Films", Science 22 Oct 2004: Vol. 306, Issue 5696, pp. 666-669

[4] A. H. Castro Neto, F. Guinea, N. M. R. Peres, K. S. Novoselov, and A. K. Geim, The electronic properties of graphene, Rev. Mod. Phys. 81, 109 Published 14 January 2009

[5] K. S. Novoselov, Z. Jiang, Y. Zhang, S. V. Morozov, H. L. Stormer, U. Zeitler, J. C. Maan, G. S. Boebinger, P. Kim, A. K. Geim, "Room-Temperature Quantum Hall Effect in Graphene", Science 09 Mar 2007: Vol. 315, Issue 5817, pp. 1379

[6] Photo: Alexander Alus, licensed by Creative Commons Attribution-Share Alike 3.0.

[7] Mak, K. F., He, K., Shan, J. and Heinz, T. F. ,"Control of valley polarization in monolayer MoS_2 by optical helicity", Nature Nanotech 7, 494-498 (2012).doi:10.1038/nnano.2012.96

[8] Kin Fai Mak et al, "Atomically Thin MoS_2: A New Direct-Gap Semiconductor", Physics Review Letters 105, 136805 (2010)

[9] Lee, C.; Yan, H.; Brus, L. E.; Heinz, T. F.; Hone, J.; Ryu, S. "Anomalous Lattice Vibrations of Single- and Few-Layer MoS_2". ACS Nano, 2010, 4, 2695-2700.

[10] Aharon Kapitulnik, Jing Xia, Elizabeth Schemm, and Alexander Palevski, "Polar Kerr effect as probe for time-reversal symmetry breaking in unconventional superconductors", New Journal of Physics 11 (2009) 055060 (18pp)

[11] C.R. Zhu, K. Zhang, M. Glazov, B. Urbaszek, T. Amand, Z. W. Ji, B.L. Liu, X. Marie, Exciton valley dynamics probed by Kerr rotation in WSe_2 monolayers, PHYSICAL REVIEW B 90, 161302(R) (2014)

[12] Hsu, W. T., Chen, Y. L., Chen, C. H., Chen, C. H., Liu, P. S., Hou, T. H., Li, L. J. and Chang, W. H. "Optically initialized robust valley-polarized holes in monolayer WSe_2", Nat Commun 6, 8963 (2015).doi:10.1038/ncomms9963

[13] X. Hong et al, "Ultrafast charge transfer in atomically thin MoS_2/WS_2 heterostructures", Nature Nanotechnology 9, 682686 (2014)

[14] A. Pant et al, Fundamentals of lateral and vertical heterojunctions of atomically thin materials, Nanoscale, 2016, 8, 3870-3887

[15] J. R. Schaibley et al, "Directional interlayer spin-valley transfer in two-dimensional heterostructures", Nature Communications 7, 13747 (2016)

[16] Y. K. Kato et al, "Observation of the Spin Hall Effect in Semiconductors", Science 10 Dec 2004: Vol. 306, Issue 5703, pp. 1910-1913

[17] Jieun Lee et al, Valley magnetoelectricity in single-layer MoS_2. Nature Materials 16, 887891 (2017)

[18] Jieun Lee et al, Electrical control of the valley Hall effect in bilayer MoS_2 transistors. Nature Nanotechnology 11, 421425 (2016)

[19] Xiaodong X. et al. Spin and pseudospins in layered transition metal dichalcogenides, Nature Physics 10, 343350 (2014)

[20] Z. Ye, D. Sun & T. F. Heinz, "Optical manipulation of valley pseudospin", Nature Physics 13, 2629 (2017)

[21] P. Rivera et al, "Observation of long-lived interlayer excitons in monolayer $MoSe_2/WSe_2$ heterostructures", Nature Communications 6, 6242 (2015)

[22] G. Plechinger et al, "Trion fine structure and coupled spinvalley dynamics in monolayer tungsten disulfide", Nature Communications 7, 12715 (2016)

[23] A. Rigosi et al, "Probing Interlayer Interactions in Transition Metal Dichalcogenide Heterostructures by Optical Spectroscopy: MoS_2/WS_2 and $MoSe_2/WSe_2$", Nano Lett., 2015, 15 (8), pp 50335038

[24] A. Molina-Sanchez, Phonons in single-layer and few-layer MoS_2 and WS_2", Physical Review B 84, 155413 (2011)

[25] Y. Li et al, "Measurement of the Optical Dielectric Function of Monolayer Transition-Metal Dichalcogenides: MoS_2, $MoSe_2$, WS_2, and WSe_2", Phys. Rev. B 90, 205422 (2014)

[26] P. Blake et al, "Making graphene visible", Applied Physics Letters 91, 063124 (2007)

[27] C. C. Katsidis et al, "General transfer-matrix method for optical multilayer systems with coherent, partially coherent, and incoherent interference", Applied Optics Vol. 41, Issue 19, pp. 3978-3987 (2002)

[28] Mak, K. F., McGill, K. L., Park, J. and McEuen, P. L. "The valley Hall effect in MoS_2 transistors". Science 344, 1489-1492 (2014).

[29] Xiao, D., Liu, G. B., Feng, W., Xu, X. and Yao, W. "Coupled spin and valley physics in monolayers of MoS_2 and other group-VI dichalcogenides". Phys Rev Lett 108, 196802 (2012).doi:10.1103/PhysRevLett.108.196802

[30] Xiao, D., Chang, M. -C. and Niu, Q. "Berry phase effects on electronic properties". Reviews of modern physics 82, 1959 (2010).

[31] Feng, W., Yao, Y., Zhu, W., Zhou, J., Yao, W. and Xiao, D. "Intrinsic spin Hall effect in monolayers of group-VI dichalcogenides: A first-principles study". Physical Review B 86, (2012).doi:10.1103/physrevb.86.165108

[32] Zhu, Z. Y., Cheng, Y. C. and Schwingenschlgl, U. "Giant spin-orbit-induced spin splitting in two-dimensional transition-metal dichalcogenide semiconductors". Phys. Rev. B 84, (2011).doi:10.1103/physrevb.84.153402

[33] Le, D., Barinov, A., Preciado, E., Isarraraz, M., Tanabe, I., Komesu, T., Troha, C., Bartels, L., Rahman, T. S. and Dowben, P. A. "Spin-orbit coupling in the band structure of monolayer WSe_2". J Phys Condens Matter 27, 182201 (2015).doi:10.1088/0953-8984/27/18/182201

[34] Li, Y., Chernikov, A., Zhang, X., Rigosi, A., Hill, H. M., van der Zande, A. M., Chenet, D. A., Shih, E., Hone, J. and Heinz, T. F. "Measurement of the optical dielectric function of monolayer transition-metal dichalcogenides:MoS_2,$MoSe_2$,WS_2, and WSe_2". Physical Review B 90, (2014).doi:10.1103/physrevb.90.205422

[35] Song, X., Xie, S., Kang, K., Park, J. and Sih, V. "Long-Lived Hole Spin/Valley Polarization Probed by Kerr Rotation in Monolayer WSe_2". Nano Lett 16, 5010-4 (2016).doi:10.1021/acs.nanolett.6b01727

[36] Alexey Chernikov, Arend M. van der Zande, Heather M. Hill, Albert F. Rigosi, Ajanth Velauthapillai, James Hone, and Tony F. Heinz, "Electrical Tuning of Exciton Binding Energies in Monolayer WS_2", Phys. Rev. Lett. 115, 126802

[37] Kim, J., Jin, C., Chen, B., Cai, H., Zhao, T., Lee, P., Kahn, S., Watanabe, K., Taniguchi, T. and Tongay, S. "Observation of Ultralong Valley Lifetime in WSe_2/MoS_2 Heterostructures". arXiv preprint. arXiv:1612.05359 (2016).

[38] Dey, P., Yang, L., Robert, C., Wang, G., Urbaszek, B., Marie, X. and Crooker, S. A. "Gate controlled spin-valley locking of resident carriers in WSe_2 monolayers". arXiv preprint. arXiv:1704.05448 (2017)

[39] 17.Yao, W., Xiao, D. and Niu, Q. "Valley-dependent optoelectronics from inversion symmetry breaking". Physical Review B 77, (2008).doi:10.1103/physrevb.77.235406

[40] Zhu, C. R., Zhang, K., Glazov, M., Urbaszek, B., Amand, T., Ji, Z. W., Liu, B. L. and Marie, X. "Exciton valley dynamics probed by Kerr rotation in WSe_2 monolayers". Physical Review B 90, 161302 (2014).

[41] Arora, A., Koperski, M., Nogajewski, K., Marcus, J., Faugeras, C. and Potemski, M. "Excitonic resonances in thin films of WSe_2: from monolayer to bulk material". Nanoscale 7, 10421-9 (2015).doi:10.1039/c5nr01536g

[42] Philipp Tonndorf et al, "Photoluminescence emission and Raman response of monolayer MoS_2, $MoSe_2$, and WSe_2", Optics Express Vol. 21, Issue 4, pp. 4908-4916 (2013)

[43] Stern, N. P., Steuerman, D. W., Mack, S., Gossard, A. C. and Awschalom, D. D. "Drift and diffusion of spins generated by the spin Hall effect". Appl. Phys. Lett 91, 062109 (2007).doi:10.1063/1.2768633